Image charge effects near solid surfaces

Thesis by
Benjamin Bobin Ye

In Partial Fulfillment of the Requirements for the
Degree of
Doctor of Philosophy in Chemical Engineering

Caltech

CALIFORNIA INSTITUTE OF TECHNOLOGY
Pasadena, California

2025
Defended August 9, 2024

© 2025

Benjamin Bobin Ye
ORCID: 0000-0003-0253-6311

ACKNOWLEDGEMENTS

I am extremely fortunate to have been surrounded by incredible friends, family, colleagues, and mentors throughout my Ph.D. journey. I am sincerely grateful to all of these individuals for fostering engaging conversations, providing welcome distractions, and creating lifelong memories. I am also thankful to the Hong Kong Quantum AI Lab, AIR@InnoHK of the Hong Kong Government for their partial support of the work in this thesis.

My deepest gratitude goes to my advisor, Prof. Zhen-Gang Wang, whose enthusiasm for research, guidance, and patience have been instrumental in shaping my personal development and research interests. In many ways, Prof. Wang has been like a father figure to me during my time at Caltech; his profound knowledge, inspiring mentorship, and unwavering support have given me invaluable opportunities to grow both as an academic and a person, enabling me to achieve things I never thought possible. I also extend my heartfelt thanks to my thesis committee members, Profs. John Brady, Konstantinos Giapis, and Kimberly See, for their continuous encouragement and guidance. Prof. Brady sparked my love for computer simulations early in my journey at Caltech, and Profs. Giapis and See laid the essential groundwork for understanding the physics in my studies through their captivating classes. Their expertise, insights, and feedback throughout my projects have significantly contributed to the success of my research. Finally, I am especially indebted to Dr. Mike Vicic for his invaluable life advice and helping me navigate the uncertainties after a long and fruitful Ph.D. career.

I am privileged to have had an exceptional cohort of classmates and labmates with whom I have had the unparalleled opportunity to work closely. I am especially thankful to Dr. Christopher Balzer, Dr. Yasemin Basdogan, Dr. Shensheng Chen, Dr. Alejandro Gallegos, Dr. Sriteja Mantha, and Dr. Edmond Zhou for their mentorship and willingness to lend an ear for research problems and life's mysteries. They have imparted on me more knowledge and wisdom than I will ever be able to repay. I am also thankful to Dorian Bruch, Alec Glisman, Alexandros Tsamopoulos, Samuel Varner, and Pierre Walker for not only being great office mates but also for their camaraderie and support. Outside of the Wang group, I appreciate the back-and-forths with and friendship of Dr. Austin Dulaney, Dr. Camilla Kjeldbjerg, Dr. Stewart Mallory, Dr. Zhiwei Peng, Dr. Hyeongjoo Row, and Dr. Andy Ylitalo.

Above all, I am eternally grateful to my parents and sister for their unwavering support and belief in me. Their love and encouragement have been my anchor throughout my doctoral studies, and I could not have achieved this milestone without them.

I truly believe that it was fate and my destiny to have come across all of these positive influences in my life. To everyone who has been a part of this journey, thank you from the bottom of my heart.

ABSTRACT

Ion–surface interactions underpin fundamental biological and technological processes and hold the key to advancing the performance of modern electrochemical devices, such as electric double-layer capacitors (EDLCs). As such, a comprehensive understanding of the mechanistic details governing these interactions and their effects on the electrical double layer structure and charge transport is crucial. However, accurately modeling ion–surface interactions in theory and simulations remains challenging due to the complexities and computational cost associated with properly treating dielectric discontinuities at ion–surface interfaces. This thesis leverages the efficient method of image charges in coarse-grained molecular dynamics simulations to capture the correct behavior at the ion–surface interface and unravel anomalous phenomena in various charged soft matter systems with conductive metal surfaces. Specifically, we construct a molecular model to demonstrate a spontaneous symmetry breaking transition in room-temperature ionic liquid EDLCs that provides a molecular mechanism for a hysteresis in the capacitance behavior observed experimentally. We also introduce a physically motivated soft-core model, the Gaussian core model with smeared electrostatics (GCMe), which addresses the limitations of traditional hard-core force fields in representing bulky organic ions and their spread charges, while also being orders of magnitude faster. Using GCMe, we then characterize the effects of the polyelectrolyte chain length, electrolyte polarizability, and electrode material on the energy storage of polymerized ionic liquid EDLCs, and the ion adsorption behavior and charging/discharging dynamics in polyelectrolyte EDLCs. Finally, we present MDCraft, an open-source Python assistant designed to streamline computational research workflows by providing tools for simulation setup, data analysis, and visualization. This comprehensive study not only enhances the understanding of ion-surface interactions but also offers practical insights and tools for advancing the design and optimization of systems involving charged species near surfaces, such as next-generation electrochemical energy storage devices.

PUBLISHED CONTENT AND CONTRIBUTIONS

(1)   Ye, B. B.; Chen, S.; Wang, Z.-G. *J. Chem. Theory Comput.* **2024**, acs.jctc.4c00603, DOI: `10.1021/acs.jctc.4c00603`.

(2)   Ye, B. B.; Wang, Z.-G. *Phys. Chem. Chem. Phys.* **2022**, *24*, 11573–11584, DOI: `10.1039/D2CP00166G`.

In each of the publications above, I contributed to the conception of the project, conducted calculations, analyzed data, and participated in the writing of the manuscript.

TABLE OF CONTENTS

LIST OF ILLUSTRATIONS

LIST OF TABLES

C h a p t e r   1

INTRODUCTION

This introductory chapter gives an overview of ion–surface interactions, their significance in electrochemical devices like electric double-layer capacitors (EDLCs), and the historical development of electrolyte and electrode materials in EDLCs. It also discusses the challenges associated with accurately modeling these interactions and understanding the structure and dynamics of ions near solid surfaces using computer simulations. The subsequent chapters detail the force fields and techniques used to model charged complex soft matter systems and the dielectric mismatch at the ion–surface interface, respectively, and present systematic studies that reveal unique adsorption behaviors near and various phenomena that occur with perfectly conducting boundaries in different electrolytes, including room-temperature ionic liquids, polymerized ionic liquids, and polyelectrolytes.

1.1   Ion–surface interactions

Ion–surface interactions refer to the various forces and phenomena that occur when ions come into contact with solid surfaces. The fundamental forces between ions and neutral or charged surfaces include short-range van der Waals forces, which describe distance-dependent nonbonded attractive and repulsive interactions and capture excluded volume or steric effects, and long-range electrostatic forces, which attract or repel ions based on their charges. Additional forces, such as chemical bonding, hydrogen bonding, and hydration effects, may also play a role depending on the chemical makeup of the charged soft matter system of interest.

These interactions are ubiquitous in nature and play a crucial role in many everyday products and biological systems. The physics behind these interactions is fundamental to numerous natural processes and technological applications involving ion–surface interfaces. For example, ion channels in cell membranes can open or close in response to the binding of specific ligands and neurotransmitters [1], and selectively allow certain ions to pass based on their interactions with the amino acids residues on the channel surfaces [2]. In medical applications, ion–surface interactions are the basis of biosensors, which rely on the selective binding of a target analyte or ion to a bioreceptor surface [3].

In recent years, one of the most significant applications of ion–surface interactions is in electrochemical devices, like batteries and electric double-layer capacitors (EDLCs), due to the proliferation of consumer electronics, electric vehicles, and renewable energy initiatives. The performance, durability, and efficiency of these energy storage devices are directly influenced by the nature of ion–surface interactions, making this area of study crucial for advancing energy storage technology. As such, we will focus on the exploration and understanding of non-Faradaic ion–surface interactions and phenomena across various combinations of ions and surface materials through the lens of EDLCs. However, many of our findings can be generalized to other systems involving ion–surface interactions.

1.2 Historical development of electrode and electrolyte materials in electric double-layer capacitors

EDLCs consist of electronic conductors (electrodes) and an ionic conductor (electrolyte), as illustrated in Fig. 1.1. EDLCs store charge electrostatically in the electrical double layer (EDL) at the ion–surface interface. In dilute selectrolytes, the EDL consists of a single layer of counterions that exactly screens the surface charge in dilute electrolytes [4, 5]. In contrast, in highly concentrated electrolytes, the EDL can span multiple layers of densely packed ions [6–9]. Generally, EDLCs are known for their high power densities, but have low energy densities compared to batteries [10]. As such, optimizing the electrode and electrolyte materials used in EDLCs is important to enhancing their performance, particularly by improving their energy densities.
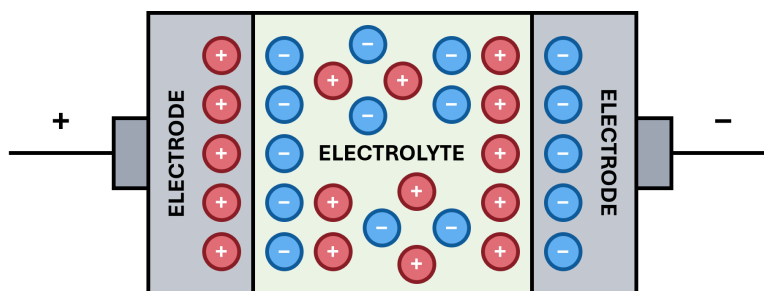
Figure 1.1: Schematic of an electric double-layer capacitor.

To this end, we begin with a historical perspective to explore the evolution of electrode and electrolyte materials in EDLCs and identify potential opportunities in unexplored ion–surface interactions and phenomena. EDLCs trace their origins back to a series of patents between 1957 through 1970 [11–13]. In their original iteration, EDLCs used aqueous electrolytes such as sulfuric acid (H_2SO_4) or potassium

hydroxide (KOH), which have small ionic radii for better access to pores and high ionic concentrations for better conductivity [14]. In the 1990s, these were replaced by organic electrolytes like acetonitrile and propylene carbonate solutions of salts, which offered larger voltage windows and improved solubility [14]. Subsequently, in the early 2000s, ionic liquids emerged as a promising electrolyte candidate due to their low vapor pressures [15], high chemical and thermal stability [15–17], low flammability [14], and, critically, wide electrochemical windows [16, 18–21] that are expected to significantly enhance the low energy density of EDLCs. Recently, polymer electrolytes and polyelectrolytes have garnered significant attention due to their similar chemical and thermal stability as ionic liquids, improved mechanical properties, and leakage-proof nature [22–24]. The physicochemical and energy storage properties of these electrolytes have been extensively studied experimentally, and numerous theoretical models have been proposed to describe their bulk and interfacial behavior.

On the electrode front, EDLCs initially employed activated carbon electrodes, which have high surface area and porosity [14, 25, 26]. In the 1990s, these were succeeded by nanostructured carbon electrodes for their high specific area and controlled pore sizes. In modern times, the focus has shifted to conductive electrodes, such as metal foils with polymer coatings and metal oxides, due to their metallic conductivity and pseudocapacitance effects that are expected to significantly enhance the capacitance of EDLCs [14, 25, 26]. While experimental studies have quantified the energy storage potential of this new class of electrodes, current theories and simulation force fields struggle to accurately represent the dielectric discontinuities at the ion–surface interface.

1.3 Challenges and opportunities of modeling ion–surface interfaces

Austrian theoretical physicist and Nobel laureate Wolfgang Pauli once said, "God made the bulk; surfaces were invented by the devil." This sentiment aptly captures the challenges of modeling ion-surface interactions in theory and simulations. In mean-field theories (MFTs), the treatment of ion–surface interactions is often unsatisfactory because mean-field approaches fail to distinguish between dielectric and conductive boundaries. Efforts have been made to include the image charge effects for conductive surfaces, such as perturbative corrections to the Poisson–Boltzmann theory [27] and non-perturbative renormalized Gaussian fluctuation theory [28, 29]. However, the former has been shown to be invalid under all limiting conditions [29], and the latter is exceedingly challenging to evaluate numerically and is inherently

still an approximation.

In molecular dynamics (MD) simulations, several methods have been developed to accurately model ion–surface interactions and capture the correct electrostatic behavior at the interface. For instance, the constant potential method is a variational approach that allows the positions and charges of surface atoms to fluctuate based on their local environments [30, 31]. Another approach, the induced charge computation method, introduces induced charges on the surface particles to maintain equipotentiality [32, 33]. However, both of these methods are computationally expensive. Thus, we turn to the method of image charges, which efficiently captures the polarization difference between the electrolyte and parallel planar conductive surfaces using explicit image charge interactions.

By pairing the method of image charges with coarse-grained MD models, we can now provide molecular insight into previously unexplored or not-well-understood behavior near ion–surface interfaces in complex charged soft matter systems over large ranges of length scales and timescales. In the subsequent chapters, we will explore various aspects of image charge effects on different ions near conductive surfaces. A central theme of this thesis is how the attractive image charge interactions can drastically alter the interfacial phenomena, structure, and behavior of ions compared to systems with dielectric or nonmetal surfaces, which minimize or lack these interactions, respectively.

First, Chapter 2 introduces the theory behind and our implementations of the main electrostatic problem-solving tool, the method of image charges, used throughout the remaining chapters. Chapter 3 builds a molecular model using the method of image charges and commonly used coarse-grained MD interaction potentials to provide a physical mechanism for the hysteresis in capacitance observed experimentally when the charging direction was reversed and the spontaneous symmetry breaking transition predicted by theory in room-temperature ionic liquid EDLCs.

In Chapter 4, we detail our development and implementation of an efficient and physically motivated soft-core model, the Gaussian core model with smeared electrostatics (GCMe). This model represents charged soft matter systems using radially Gaussian-distributed mass and charge densities, which more rigorously describe bulky organic ions that can interpenetrate and spread their charges along their backbones, and can be multiple orders of magnitude faster than than traditional hard-core models. As an illustrative example of GCMe and a segue from the monomeric ions in Chapter 3 to the polyelectrolyte systems we are interested in, Chapter 5 uses

GCMe to systematically explore how the chain length, relative permittivity of the electrolyte, and the image charge effects impact the energy storage in polymerized ionic liquid EDLCs. Then, Chapter 6 characterizes the EDL structure and charge transport in polyelectrolyte EDLCs with nonmetal and perfectly conducting boundaries using GCMe, and reports complete reversals in the adsorption behavior and charging/discharging dynamics. Finally, Chapter 7 presents MDCraft, an in-house open-source Python assistant that we developed and used extensively to streamline the research workflows in the preceding chapters, from setting up and running MD simulations to analyzing, modeling, and plotting data from the trajectories. MDCraft not only provides access to our implementations of the method of image charges and GCMe but also includes optimized serial and multithreaded analysis classes that evaluate complex structural, thermodynamic, and transport properties, making computational chemistry more accessible to a broader audience.

References

(1)   Alberts, B., *Molecular biology of the cell*, Sixth edition; Garland Science, Taylor and Francis Group: New York, NY, 2015.

(2)   Roux, B. *Essays Biochem.* **2017**, *61*, ed. by Lippard, S. J.; Berg, J. M., 201–209, DOI: `10.1042/EBC20160074`.

(3)   Shanbhag, M. M.; Manasa, G.; Mascarenhas, R. J.; Mondal, K.; Shetti, N. P. *Chem. Eng. J. Adv.* **2023**, *16*, 100516, DOI: `10.1016/j.ceja.2023.100516`.

(4)   Gouy, M. *J. Phys. Theor. Appl.* **1910**, *9*, 457–468, DOI: `10.1051/jphystap:019100090045700`.

(5)   Chapman, D. L. *Lond. Edinb. Dubl. Phil. Mag.* **1913**, *25*, 475–481, DOI: `10.1080/14786440408634187`.

(6)   Kornyshev, A. A. *J. Phys. Chem. B* **2007**, *111*, 5545–5557, DOI: `10.1021/jp067857o`.

(7)   Fedorov, M. V.; Kornyshev, A. A. *J. Phys. Chem. B* **2008**, *112*, 11868–11872, DOI: `10.1021/jp803440q`.

(8)   Fedorov, M. V.; Kornyshev, A. A. *Electrochim. Acta* **2008**, *53*, 6835–6840, DOI: `10.1016/j.electacta.2008.02.065`.

(9)   Begić, S.; Chen, F.; Jónsson, E.; Forsyth, M. *Phys. Rev. Mater.* **2019**, *3*, 095801, DOI: `10.1103/PhysRevMaterials.3.095801`.

(10) Christen, T.; Carlen, M. W. *J. Power Sources* **2000**, *91*, 210–216, DOI: `10.1016/S0378-7753(00)00474-2`.

(11) Becker, H. Low voltage electrolytic capacitor, US2800616A, 1957.

(12) Rightmere, R. Electrical energy storage apparatus, US3288641A, 1966.

(13) Boos, D. Electrolytic capacitor having carbon paste electrodes, US3536963A, 1970.

(14) Wang, G.; Zhang, L.; Zhang, J. *Chem. Soc. Rev.* **2012**, *41*, 797–828, DOI: `10.1039/C1CS15060J`.

(15) Arbizzani, C.; Biso, M.; Cericola, D., et al. *J. Power Sources* **2008**, *185*, 1575–1579, DOI: `10.1016/j.jpowsour.2008.09.016`.

(16) Barisci, J. *Electrochem. Commun.* **2004**, *6*, 22–27, DOI: `10.1016/j.elecom.2003.09.015`.

(17) Ruiz, V.; Huynh, T.; Sivakkumar, S. R.; Pandolfo, A. G. *RSC Adv.* **2012**, *2*, 5591, DOI: `10.1039/c2ra20177a`.

(18) Suarez, P. A.; Selbach, V. M.; Dullius, J. E., et al. *Electrochim. Acta* **1997**, *42*, 2533–2535, DOI: `10.1016/S0013-4686(96)00444-6`.

(19) Sato, T.; Masuda, G.; Takagi, K. *Electrochim. Acta* **2004**, *49*, 3603–3611, DOI: `10.1016/j.electacta.2004.03.030`.

(20) Van Aken, K. L.; Beidaghi, M.; Gogotsi, Y. *Angew. Chem. Int. Ed.* **2015**, *54*, 4806–4809, DOI: `10.1002/anie.201412257`.

(21) Mousavi, M. P. S.; Wilson, B. E.; Kashefolgheta, S., et al. *ACS Appl. Mater. Interfaces* **2016**, *8*, 3396–3406, DOI: `10.1021/acsami.5b11353`.

(22) Yan, C.; Jin, M.; Pan, X.; Ma, L.; Ma, X. *RSC Adv.* **2020**, *10*, 9299–9308, DOI: `10.1039/C9RA10701K`.

(23) Moore, D.; Arcila, J. A.; Saraf, R. F. *Langmuir* **2020**, *36*, 1864–1870, DOI: `10.1021/acs.langmuir.9b03734`.

(24) Aziz, S. B.; Brza, M. A.; Abdulwahid, R. T., et al. *Sci. Rep.* **2023**, *13*, 21139, DOI: `10.1038/s41598-023-48417-6`.

(25) Iro, Z. S.; Subramani, C.; Dash, S. *Int. J. Electrochem. Sci.* **2016**, *11*, 10628–10643, DOI: `10.20964/2016.12.50`.

(26) Miller, E. E.; Hua, Y.; Tezel, F. H. *Journal of Energy Storage* **2018**, *20*, 30–40, DOI: `10.1016/j.est.2018.08.009`.

(27) Kanduč, M.; Podgornik, R. *Eur. Phys. J. E* **2007**, *23*, 265–274, DOI: `10.1140/epje/i2007-10187-2`.

(28) Wang, Z.-G. *Phys. Rev. E* **2010**, *81*, 021501, DOI: `10.1103/PhysRevE.81.021501`.

(29) Wang, R.; Wang, Z.-G. *J. Chem. Phys.* **2013**, *139*, 124702, DOI: `10.1063/1.4821636`.

(30) Siepmann, J. I.; Sprik, M. *J. Chem. Phys.* **1995**, *102*, 511–524, DOI: `10.1063/1.469429`.

(31) Reed, S. K.; Lanning, O. J.; Madden, P. A. *J. Chem. Phys.* **2007**, *126*, 084704, DOI: `10.1063/1.2464084`.

(32) Tyagi, S.; Süzen, M.; Sega, M., et al. *J. Chem. Phys.* **2010**, *132*, 154112, DOI: `10.1063/1.3376011`.

(33) Nguyen, T. D.; Li, H.; Bagchi, D.; Solis, F. J.; Olvera De La Cruz, M. *Comput. Phys. Commun.* **2019**, *241*, 80–91, DOI: `10.1016/j.cpc.2019.03.006`.

Chapter 2

METHOD OF IMAGE CHARGES

Energy storage devices, such as batteries and electric double-layer capacitors (EDLCs), can be constructed from a diverse array of high-performance electrode and electrolyte materials. When modeling these systems using molecular dynamics (MD) simulations to quantify physical properties and explore phase phenomena, it is essential to capture the boundary polarization effects caused by dielectric mismatches at the ion–surface interfaces. From a continuum electrostatics perspective, ions are repelled from or attracted to surfaces with much lower or higher relative permittivities, respectively, because the surfaces can polarize in response to the nearby ions. For instance, with perfectly conducting metal boundaries, which have relative permittivities many orders of magnitude higher than most traditional electrolytes, the adsorption behavior of the charged species and the charging/discharging dynamics can be markedly different compared to systems where the surfaces and electrolytes have similar relative permittivities. The following chapter introduces the method of image charges, an electrostatic problem-solving tool that provides a straightforward and efficient way to account for surface polarization in systems with parallel planar surfaces.

This chapter includes content from our previously published articles:

Ye, B. B.; Wang, Z.-G. *Phys. Chem. Chem. Phys.* **2022**, *24*, 11573–11584, DOI: `10.1039/D2CP00166G`

Ye, B. B.; Chen, S.; Wang, Z.-G. *J. Chem. Theory Comput.* **2024**, acs.jctc.4c00603, DOI: `10.1021/acs.jctc.4c00603`

2.1 Introduction

In systems with charged species and parallel planar surfaces, such as EDLCs, an important consideration is the proper treatment of the ion–surface interactions to capture the correct electrostatic behavior at the interface. Two commonly used methods to enforce constant surface charges are maintaining constant charges on the atoms that constitute the surfaces and allowing the charges of the atoms to fluctuate based on the local environment via the versatile variational procedure formulated by Siepmann and Sprik [3]. However, the former approach gives vastly

different electrical double layer (EDL) structures and dynamics compared to those acquired from systems where the surfaces can polarize in response to nearby charge fluctuations [4], and the latter is computationally expensive.

An alternative and efficient approach for parallel planar perfectly conducting surfaces is the method of image charges, which accounts for the dielectric mismatch between the electrolyte and the bounding medium using image charge interactions. An ion feels repulsion from or attraction to the interface when the surface material has a lower or higher relative permittivity $\varepsilon_{r, \text{surface}}$ than that of the electrolyte (ε_r), respectively, because the corresponding image charge on the other side of the interface carries a charge of

$$q_{i, \text{IC}} = z_i e \frac{\varepsilon_r - \varepsilon_{r, \text{surface}}}{\varepsilon_r + \varepsilon_{r, \text{surface}}}, \tag{2.1}$$

which has the same sign as the ion when $\varepsilon_r > \varepsilon_{r, \text{surface}}$ and the opposite sign when $\varepsilon_r < \varepsilon_{r, \text{surface}}$. We focus on the limiting cases of perfectly conducting metal surfaces ($\varepsilon_{r, \text{surface}} = \infty$), where the image charges have equal but opposite charges to the ions they mirror, and nonmetal surfaces with the same permittivity as the electrolyte, where the image charges vanish.

2.2 Implementations
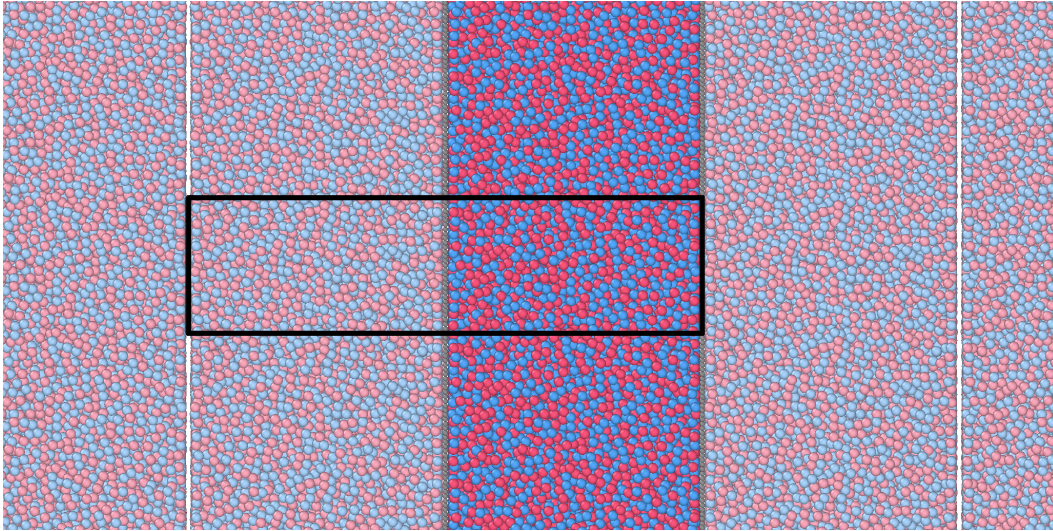
Figure 2.1: Two-dimensional representation of the three-dimensional periodic system with image charges. The unit cell containing the real and image systems is enclosed in a solid box. The blue and red colors represent the negative and positive charges, while the dark and light shades specify the real and image charges, respectively.

The method of image charges was recently implemented in both LAMMPS [5] by Dwelle and Willard [6] to take advantage of its spatial decomposition techniques and wide hardware acceleration support, and OpenMM [7] by Son and Wang [8] to fully leverage its GPU acceleration to achieve performance that is orders of magnitude higher than that of traditional multithreaded CPU implementations. The implementation is based on the method proposed by Hautman et al. [9], which includes infinitely many repeating systems of image charges for a system of ions in a three-dimensional MD simulation. In the extended simulation box of dimension $L_x \times L_y \times 2L_z$, there are two subsystems: a real system ($0 < z < L_z$) that contains the real ions, and an image system ($-L_z < z < 0$) that contains the image charges mirroring the real ions. The method of image charges involves reflecting the ions in the real system across the surface at $z = 0$ and giving them opposite charges to create the corresponding image charges in the image system. With periodic boundary conditions, the subsystems form a repeat unit that is electroneutral, has no net potential difference between $z = -L_z$ and $z = L_z$, and repeats ad infinitum in all directions, as shown in Fig. 2.1. It is periodic in the x- and y-directions to simulate a slab and in the z-direction as both surfaces are perfectly conducting. In each timestep, because the motion of the real ions and the image charges are coupled, the positions of the real ions are updated first by evaluating the forces acting on them from their interactions with each other and the image charges, and integrating the Langevin equation of motion. Then, the positions of the image charges are updated to reflect the new positions of the real ions.

References

(1) Ye, B. B.; Wang, Z.-G. *Phys. Chem. Chem. Phys.* **2022**, *24*, 11573–11584, DOI: 10.1039/D2CP00166G.

(2) Ye, B. B.; Chen, S.; Wang, Z.-G. *J. Chem. Theory Comput.* **2024**, acs.jctc.4c00603, DOI: 10.1021/acs.jctc.4c00603.

(3) Siepmann, J. I.; Sprik, M. *J. Chem. Phys.* **1995**, *102*, 511–524, DOI: 10.1063/1.469429.

(4) Merlet, C.; Péan, C.; Rotenberg, B., et al. *J. Phys. Chem. Lett.* **2013**, *4*, 264–268, DOI: 10.1021/jz3019226.

(5) Plimpton, S. *J. Comput. Phys.* **1995**, *117*, 1–19, DOI: 10.1006/jcph.1995.1039.

(6) Dwelle, K. A.; Willard, A. P. *J. Phys. Chem. C* **2019**, *123*, 24095–24103, DOI: 10.1021/acs.jpcc.9b06635.

(7)   Eastman, P.; Swails, J.; Chodera, J. D., et al. *PLoS Comput. Biol.* **2017**, *13*, ed. by Gentleman, R., e1005659, DOI: `10.1371/journal.pcbi.1005659`.

(8)   Son, C. Y.; Wang, Z.-G. *Proc. Natl. Acad. Sci. U.S.A.* **2021**, *118*, e2020615118, DOI: `10.1073/pnas.2020615118`.

(9)   Hautman, J.; Halley, J. W.; Rhee, Y.-J. *J. Chem. Phys.* **1989**, *91*, 467–472, DOI: `10.1063/1.457481`.

Chapter 3

SPONTANEOUS SURFACE CHARGE SEPARATION IN ROOM-TEMPERATURE IONIC LIQUIDS

Room-temperature ionic liquids (RTILs) have garnered considerable interest lately due to their high chemical and thermal stability, low volatility, and large electrochemical windows. These are all qualities that enable a wide range of potential applications. Notably, RTILs are highly promising as electrolytes for electromechanical devices, such as actuators and sensors, and the next generation of high-performance energy storage devices, like batteries and electric double-layer capacitors (EDLCs). Therefore, understanding their behavior at the molecular level is crucial for optimizing their performance in these applications.

Numerous experimental studies and theoretical models have investigated the distinctive characteristics of RTIL EDLCs. Notably, recent mean-field theories predict that RTIL EDLCs undergo a spontaneous surface charge separation (SSCS) with no applied potential. In this chapter, we construct a coarse-grained molecular model that corresponds to the mean-field models to directly simulate the behavior of RTILs without invoking mean-field approximations. In addition to observing the SSCS transition, we highlight the importance of the image charge interactions and explore the enhanced in-plane ordering on the electrodes, two effects not accounted for by the mean-field theories. By comparing the differential capacitance for RTILs confined between perfectly conducting and nonmetal electrodes, we show that the image charge interactions can drastically improve the energy storage properties of RTIL EDLCs.

This chapter includes content from our previously published article:

3.1   Introduction

Room-temperature ionic liquids (RTILs) are synthetic organic salts that are in the liquid state at ambient conditions and generally consist of at least one bulky organic ion [2]. RTILs have been studied extensively in the past two decades owing to their promising electrochemical performance compared to traditional electrolytes. As

the design objective of energy storage devices is to maximize both the energy and power densities, RTILs are prime electrolyte candidates for use in electric double-layer capacitors (EDLCs) due to their larger operational voltage windows [3–7], lower vapor pressure and freezing points [8], and higher chemical and thermal stability [4, 8, 9]. Compared to rechargeable batteries, EDLCs have higher power densities because their faster non-faradaic charging and discharging processes are not limited by charge transfer kinetics, but lower energy densities since they store charge electrostatically instead of electrochemically [10–12]. Since the maximum energy U an EDLC can store scales as $CV^2/2$, the wider electrochemical windows of RTILs can enable EDLCs with higher energy storage.

For such applications, the structure of the electric double-layers (EDLs) near the metal electrodes is important. EDLs in dilute electrolytes consist of a Stern layer of counterions that screen the surface charge and are well understood due to the classical Gouy–Chapman–Stern (GCS) theory [13, 14], but EDLs in highly concentrated electrolytes, such as RTILs, can span multiple layers of densely packed ions due to overscreening and crowding [2, 15–17]. These effects are driven by the "ion–ion correlations" in RTILs, which are primarily attributed to the incompatible functional groups and chemical differences between the cations and anions but can also have contributions from short-range electrostatic correlations [18, 19].

By considering the finite volume occupied by the ions, Kornyshev [2] found that the crowding of counterions near the surface can drastically affect the voltage dependency of the differential capacitance. In contrast with the GCS model, which gives U-shaped capacitance–voltage curves, the Kornyshev model predicted bell- and camel-shaped capacitance–voltage curves for dense and dilute systems, respectively, which were shown to be consistent with the ensuing capacitance results from computer simulations [15, 16] and experimental observations of the EDL structure [20, 21] despite it not accounting for the short-range ion–ion correlations that can be very strong in RTILs [22–26].

Subsequently, Bazant, Storey, and Kornyshev (BSK) [27] proposed a phenomenological mean-field theory (MFT) that incorporates the ion–ion correlations through nonlocality in the relative permittivity and demonstrates the overscreening and crowding of counterions across multiple layers at moderate and high potentials, respectively. Lee et al. [28] showed that the BSK model maps to a lattice-based MFT with a composite Coulomb–Yukawa potential, where the Yukawa potential accounts for the electrostatic ion–ion correlations but has also been used by May and cowork-

ers [29–31] to capture the hydration-mediated non-electrostatic ion–ion interactions in aqueous solutions. This Yukawa potential essentially results in the effective attraction (repulsion) between like (opposite) charges. Limmer [32] offered an alternative phenomenological free energy model that treats the ion–ion correlations with repulsive non-electrostatic interactions between counterions and approximates small potential differences with an effective surface adsorption. Interestingly, Limmer showed that the competition between the short-range ion–ion correlations and long-range electrostatic interactions can lead to the onset of a fluctuation-induced spontaneous surface charge separation (SSCS) before any bulk phase separation. Then, Chao and Wang (CW) [19] generalized the BSK model by adding a dimensionless parameter α to control the strength of the ion–ion correlations. The Helmholtz free energy F for the CW model is

$$
\begin{aligned}
\frac{F}{k_{\mathrm{B}}T} = \frac{1}{v} \int & \left[\frac{1+\phi}{2} \ln\left(\frac{1+\phi}{2} \right) + \frac{1-\phi}{2} \ln\left(\frac{1-\phi}{2} \right) \right] d\mathbf{r} \\
& + \frac{1}{8\pi\lambda_{\mathrm{D}}^2 v} \iint \frac{\phi(\mathbf{r})\,\phi(\mathbf{r}')}{|\mathbf{r}-\mathbf{r}'|} \, d\mathbf{r}\,d\mathbf{r}' \\
& - \frac{\alpha}{8\pi\lambda_{\mathrm{D}}^2 v} \iint \frac{\phi(\mathbf{r})\exp\left(-|\mathbf{r}-\mathbf{r}'|/\ell_{\mathrm{c}}\right)\phi(\mathbf{r}')}{|\mathbf{r}-\mathbf{r}'|} \, d\mathbf{r}\,d\mathbf{r}',
\end{aligned}
\tag{3.1}
$$

where k_{B} is the Boltzmann constant, T is the absolute temperature, v is the molecular volume, ϕ is the local charge density, ψ is the electrostatic potential, λ_{D} is the nominal screening length, and ℓ_{c} is the ion–ion correlation length. The CW model also predicts SSCS for ion–ion correlation strengths greater than a critical $\alpha_{s,c}$ value and shows that SSCS should be a common feature in RTIL EDLCs. Recently, Bossa and May (BM) [33] presented a lattice-based MFT accounting for the penetration of the Yukawa field into the electrode that was neglected in Ref. 18. It also anticipates SSCS but finds that the CW model had overestimated the extent of the transition.

While the MFTs have provided insight into the origin of the SSCS transition, their treatments of the ion–electrode interactions are unsatisfactory since their mean-field nature prevents the distinction between dielectric and metal boundaries. The potential in the metal electrodes is constant because the movement and rearrangement of their free electrons negate the electric field, but can fluctuate for dielectrics since they only polarize in response to the applied field. However, at the mean-field level, the dielectric property of the electrodes is not reflected because the averaged electrostatic potential, which varies only in one spatial direction, is used in the free energy calculations. Furthermore, the MFTs show that SSCS is a second-order transition due to an underlying microphase separation, but it is likely a weakly first-order

fluctuation-induced transition that belongs to the Brazovskii universality class [34] beyond the mean-field, as suggested by Limmer [32].

In this chapter, we construct a molecular model that corresponds to the phenomenological BSK, CW, and BM models to capture the non-mean-field effects in RTIL EDLCs. We conduct molecular dynamics (MD) simulations of coarse-grained RTILs that properly account for the different dielectric properties of ideal perfectly conducting (PC) metal boundaries and nonmetal (NM) boundaries with the same relative permittivity as the RTIL using the method of image charges to explore the driving forces behind, and the propensity for, surface phenomena such as SSCS and in-plane surface ordering, and investigate how the ion–electrode interactions affect the capacitance properties of RTILs when potential differences are applied.

3.2 Model and methods

Pair potentials

We aim to construct a coarse-grained molecular model that corresponds to the free energy functional in Eq. 3.1. In this model, the anions and cations are represented by featureless equisized spherical particles with opposite point charges $-q$ and q at the center, respectively, that interact via centrosymmetric pair potentials, and the ion polarization effects are implicitly accounted for with a dielectric continuum. The long-range electrostatic interaction between any two real or image charges i and j is modeled by the Coulomb potential, the short-range non-electrostatic excluded volume interaction between real ions i and j is modeled by a combination of Weeks–Chander–Andersen (WCA) and Gaussian potentials, and the short-range ion–ion correlations are accounted for by a Yukawa potential. As it is convenient to work in Lennard-Jones units, all input parameters and output quantities in the remainder of this chapter have been scaled by the fundamental quantities—mass m, ion size σ, energy ϵ, and k_{B}—unless otherwise noted. The derivations of key dimensionless quantities can be found in the Appendix.

The Coulomb potential has the form

$$U_{\mathrm{Coul}}\left(r_{ij}\right) = \frac{q_i q_j}{\varepsilon_{\mathrm{r}} r_{ij}} = \frac{z_i z_j \lambda_{\mathrm{B}} T}{r_{ij}}, \tag{3.2}$$

where q_i and q_j are the charges of ions i and j, respectively, ε_{r} is the relative permittivity, and r_{ij} is the separation distance between ions i and j. By expressing the charge $q = ze$ in terms of the charge number z and the elementary charge e, the Coulomb potential can also be written in terms of the Bjerrum length $\lambda_{\mathrm{B}} = e^2/\varepsilon_{\mathrm{r}} T$.

The coulombic interactions are evaluated using a particle-particle particle-mesh (PPPM) solver, which approximates the electrostatic potential by computing the short-range interactions within a cutoff normally in a pairwise fashion in real space and the long-range interactions past the cutoff using fast Fourier transforms in reciprocal space [35, 36].

The excluded volume interaction is given by

$$U_{\text{ex}}\left(r_{ij}\right) = U_{\text{WCA}}\left(r_{ij}\right) + U_{\text{Gauss}}\left(r_{ij}\right), \tag{3.3}$$

where U_{WCA} and U_{Gauss} are the WCA and soft Gaussian potentials, respectively. The WCA potential has the form

$$U_{\text{WCA}}\left(r_{ij}\right) = \begin{cases} 4\epsilon_{ij}\left[\left(\dfrac{\sigma_{ij}}{r_{ij}}\right)^{12} - \left(\dfrac{\sigma_{ij}}{r_{ij}}\right)^{6}\right] + \epsilon_{ij}, & r_{ij} \leq 2^{1/6} \\ 0, & r_{ij} > 2^{1/6} \end{cases}, \tag{3.4}$$

where ϵ_{ij} and σ_{ij} are the scaled dispersion energy and mean ion size, respectively, between ions i and j.

The truncated and shifted Gaussian potential has the form

$$U_{\text{Gauss}}\left(r_{ij}\right) = \begin{cases} A_{ij}\left[\exp\left(-B_{ij}r_{ij}^2\right) - \exp\left(-B_{ij}\right)\right], & r_{ij} \leq 1 \\ 0, & r_{ij} > 1 \end{cases}, \tag{3.5}$$

where A_{ij} and B_{ij} are parameters that set the interaction energy and range, respectively, between ions i and j. This purely repulsive soft potential, with arbitrarily chosen $A_{ij} = 1,000$ and $B_{ij} = 7$, is used in conjunction with a "soft" WCA potential with $\epsilon_{ij} = 0.01$ and $\sigma_{ij} = 1$ to capture the excluded volume interactions of the squishy RTIL ions that can deform and interpenetrate due to the cushioning from the alkyl chains or organic groups. Importantly, this hybrid potential also prevents a bulk liquid–solid phase transition, which is likely to be observed in systems of densely packed charged "hard" Lennard-Jones spheres due to geometric packing [37] but is not observed in RTILs at ambient conditions.

The Yukawa potential has the form

$$U_{\text{Yukawa}}\left(r_{ij}\right) = \begin{cases} -\alpha\dfrac{z_i z_j \lambda_{\text{B}}T}{r_{ij}}\left[\exp(-r_{ij}/\ell_{\text{c}}) - \exp(-L_z/2\ell_{\text{c}})\right], & r_{ij} \leq L_z/2 \\ 0, & r_{ij} > L_z/2 \end{cases}, \tag{3.6}$$

where α is a dimensionless parameter that controls the strength and ℓ_c is the inverse decay length of the Yukawa potential. While any short-range pair potential could have been used to model the ion–ion correlations, we use the Yukawa potential with the correlation length set to $\ell_\mathrm{c} = 1$ to match the ion size due to the similar formulation in the BSK, CW, and BM models. It is important to note that the Yukawa potential with varying ion–ion correlation strengths α is the distinguishing factor of each system simulated since the WCA–Gaussian potential is the same across all simulation runs in this study. A comparison of magnitudes of the hybrid WCA–Gaussian potential with WCA potentials with $\epsilon_{ij} = 0.01$ and $\epsilon_{ij} = 1$, the Coulomb potential, and the Yukawa potential with $\alpha = 0.8$ is shown in Fig. 3.1.
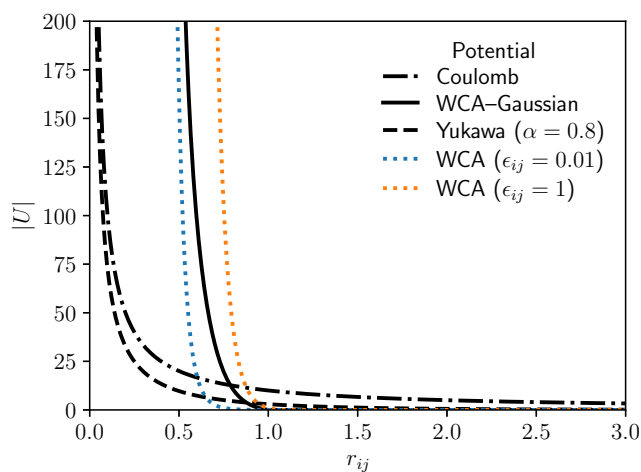
Figure 3.1: Comparison of the magnitudes and ranges of the electrostatic (Coulomb) and excluded volume (WCA, hybrid WCA–Gaussian, and Yukawa) pair potentials.

Lastly, the non-electrostatic interaction between the real ions and the electrodes is modeled by the WCA potential in Eq. 3.4 with a cutoff of $r_{ij} \leq 2^{-5/6}$ and parameters $\epsilon_{ij} = 100$ and $\sigma_{ij} = 0.5$. Here, r_{ij} is the z-distance between ion i and the wall and σ_{ij} represents the closest contact of ion i to the surface.

In addition to being analogous to the BSK, CW, and BM models, our model is phenomenologically equivalent to the lattice models used previously to study frustrated Coulomb liquids [38–40] and ionic liquids [32, 41, 42]. The long-range Coulomb and short-range Yukawa interactions used in the current model correspond to the electrostatic interactions and nearest neighbor attraction, respectively, between co-ions in the lattice models.

System

Simulations of RTIL EDLCs were carried out using LAMMPS in the canonical ensemble with $N = 1,000$ real particles, a number density of $\rho = 0.8$, and a temperature of $T = 1$. The relative permittivity and Bjerrum length were set to $\varepsilon_r = 12$ and $\lambda_B = 10$, respectively, which are typical for RTILs [2, 27, 43]. With these parameters, the elementary point charges ($-z_- = z_+ = 1$) have reduced charge magnitudes of $q = \sqrt{\varepsilon_r \lambda_B T} \approx 11$ and a nominal Debye length of $\lambda_D = (4\pi\lambda_B\rho)^{-1/2} \approx 0.1$.

The system is initialized by creating a $L \times L \times 2L$ simulation box containing the real and image subsystems, establishing two smooth planar walls at $z = 0$ and $z = L$ to represent the metal electrodes, and placing ions in the real system. The method of image charges is employed to account for the dielectric mismatch at the ion–electrode interface and mirrors the real ions into the image system. The electrode separation distance $L_z = L$ is selected such that the desired number density $\rho = N/V$ is achieved in the cubic real system, where $V = L_x L_y L_z = L^3$ is the volume of the real system.

For each simulation, energy minimization and system equilibration were performed over at least 10^5 timesteps of step size $\tau = 0.001$, and data was collected for at least another $2 \times 10^6 \tau$. Desired quantities for each set of parameters are calculated by block averaging data over at least two independent trajectories. For systems close to transition points, data was collected for and averaged over at least ten different trajectories to minimize noise. In the perspective of a common RTIL like [EMIM$^+$][BF$_4^-$] or [EMIM$^+$][NTf$_2^-$], the relevant timescale is on the order of picoseconds, as shown in the Appendix, and the production runs have lengths on the order of tens of nanoseconds.

3.3   Results and discussion

Spontaneous surface charge separation without applied potential difference

A range of Yukawa interaction strengths from $\alpha = 0$ to $\alpha = 1.35$ was explored, with the simulations started from both homogeneous and charge-separated configurations to ensure that the systems converge to the same equilibrium state for each α value regardless of the initial state.

To quantify charge separation, we calculated the relevant order parameter, the surface charge density, for each system. First, the local charge density profile $\rho_q(z)$ is given

by

$$\langle \rho_q(z) \rangle = q \left(\langle \rho_+(z) \rangle - \langle \rho_-(z) \rangle \right), \tag{3.7}$$

where the angular brackets denote the ensemble average and $\rho_-(z)$ and $\rho_+(z)$ are the anion and cation density profiles, respectively, which are spatially averaged over the x- and y-directions and computed by binning the real systems in the z-direction into 100 intervals, counting the number of relevant ions, and dividing the counts by the volume of the bins. Then, as shown by Hautman et al. [44] and derived by Qing et al. [45], the surface charge density σ_q is obtained using

$$\langle \sigma_q \rangle = \sigma_q^s + \langle \sigma_q^p \rangle = \frac{\varepsilon_r \Delta V}{4\pi L_z} - \frac{1}{L_z} \int_0^{L_z} z \langle \rho_q(z) \rangle \, dz, \tag{3.8}$$

where ΔV is the constant potential difference between the two electrodes. The static term σ_q^s accounts for the direct response to the applied potential in the dielectric medium with relative permittivity ε_r, while the polarization term σ_q^p accounts for the charge separation.

The SSCS transition can be further characterized by analyzing the system dipole and the differential capacitance. The instantaneous system dipole M_z is given by

$$M_z = \sum_i q_i z_i, \tag{3.9}$$

where q_i and z_i are the charge and z-position, respectively, of ion i. The distribution of the instantaneous system dipoles shows how large the charge fluctuations are in the system, and it can be shown that the surface charge density is related to the system polarization with $\langle \sigma_q^p \rangle$ in Eq. 3.8 being equivalent to $-\langle M_z \rangle / V$. The differential capacitance C_d is defined as

$$C_d = \frac{\partial \langle \sigma_q \rangle}{\partial \Delta V} = \frac{L_x L_y}{T} \langle (\delta \sigma_q)^2 \rangle, \tag{3.10}$$

where $\delta \sigma_q = \sigma_q - \langle \sigma_q \rangle$ is the surface charge density fluctuation [46, 47]. A discontinuity or divergence in the C_d–α relationship would signify the onset of SSCS transition [48]. While the partial derivative definition is less affected by thermal noise and typically gives more accurate results, the fluctuation definition allows for C_d to be evaluated for systems with $\Delta V = 0$ without needing any information from additional simulations with applied potentials. As such, the fluctuation definition is used for the following analysis in the absence of applied potentials.

Figs. 3.2a and 3.2b show the surface charge densities and differential capacitance, respectively, at different Yukawa interaction strengths, while Fig. 3.2c shows the
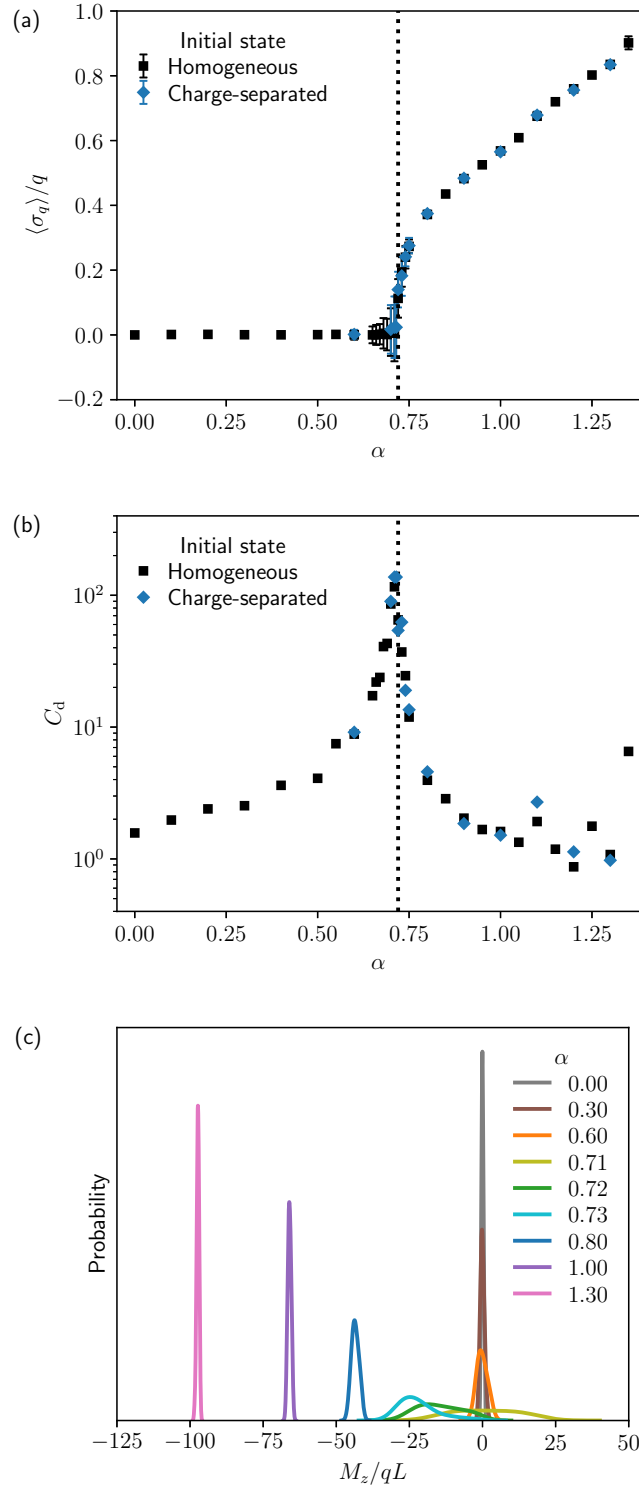
Figure 3.2: (a) Ensemble-averaged surface charge density $\langle\sigma_q\rangle$ and (b) zero voltage differential capacitance C_{d} as a function of the Yukawa interaction strength α, and (c) system dipole distributions for selected α values with $\Delta V = 0$ when starting from homogeneous and charge-separated systems. The error bars in (a) represent one standard deviation from the mean, and the dotted lines in (a) and (b) identify the transition point $\alpha_{\mathrm{t}} = 0.72$ of the spontaneous surface charge separation.

system dipole distributions for selected α values. While Figs. 3.2a and 3.2b have separate plots for the systems starting from homogeneous and charge-separated states, Fig. 3.2c combines the system dipole distributions for both initial states. As expected, the systems evolve into the same final state for each Yukawa interaction strength regardless of the initial state, as shown by the overlapping curves in Figs. 3.2a and 3.2b. The surface charge density remains 0 until the transition point $\alpha_t \approx 0.72$, at which the $\langle \sigma_q \rangle$–α relationship bifurcates into two curves with equal but opposite magnitudes and the dipole distribution becomes bimodal since both SSCS directions are equally favorable when starting from an isotropic fluid. Note that only the positive half of the $\langle \sigma_q \rangle$–α curve and the corresponding dipole distributions for α values past the transition point are shown in Fig. 3.2. Details on how the transition point was determined and how the surface charge densities and dipole distributions were computed can be found in the Appendix.

For $\alpha = 0$, the surface charge density is 0 and the unimodal dipole distribution has a narrow peak at $M_z = 0$. The differential capacitance and charge fluctuations grow with increasing α, as evidenced by Fig. 3.2b and the widening ranges of the dipole distributions in Fig. 3.2c, respectively, but the dipole distributions continue to be symmetric about $M_z = 0$. As α approaches the transition point, the differential capacitance increases sharply while the dipole distribution flattens out, indicating significantly more pronounced charge fluctuations in the system and suggesting an incipient bimodality.

The transition point at $\alpha_t = 0.72$ marks the onset of a spontaneous symmetry breaking transition with no potential difference, when the enhanced charge fluctuations from the Yukawa potential lead to stable surface charges on the two electrodes but an electroneutral bulk RTIL, as shown in the charge density profiles in Fig. 3.3. However, we cannot fully resolve the order of the transition using Fig. 3.2 since it is unclear whether there are discontinuities in the $\langle \sigma_q \rangle$–α and C_d–α relationships and if the peak in the differential capacitance is divergent at the transition point. Nevertheless, the non-Gaussian nature of the dipole distribution at the transition point suggests that SSCS is likely a weakly first-order transition driven by the correlation effects [49].

After the transition, the surface charge density becomes non-zero and monotonically increases, the differential capacitance sharply decreases, and the peak of the dipole distribution is no longer centered on $M_z = 0$ and shifts further to the left. Additionally, the dipole distribution narrows as the systems take on increasingly ordered
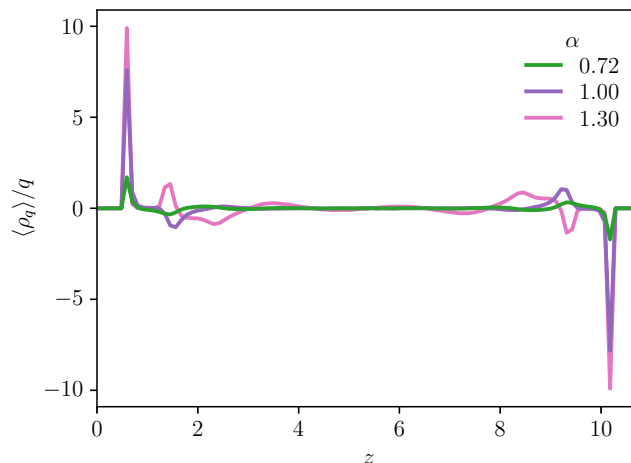
Figure 3.3: Ensemble-averaged charge density profiles $\langle \rho_q \rangle$ at the transition point $\alpha_t = 0.72$ of the spontaneous surface charge separation, and for strong Yukawa interaction strengths $\alpha = 1$ and $\alpha = 1.3$ with $\Delta V = 0$.
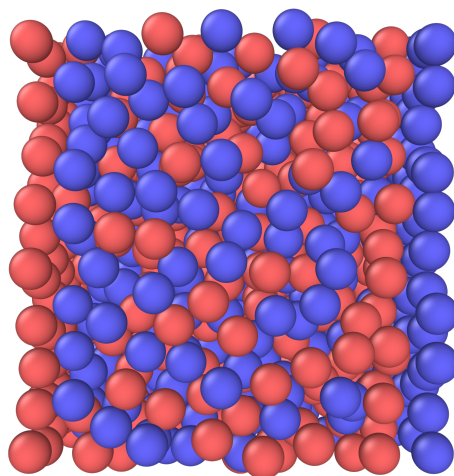
Figure 3.4: Side view of an equilibrated real system for Yukawa interaction strength $\alpha = 1$ with $\Delta V = 0$ that has undergone spontaneous surface charge separation.

SSCS states and the charge fluctuations are suppressed. The snapshot in Fig. 3.4 for an $\alpha = 1$ system shows that the ion monolayers next to the electrodes are fully filled to screen the induced surface charge on the corresponding electrode, and the second layer is dominated by counterions to screen the excess charge in the first layer. This overscreening is observed in the three layers next to the electrodes as the charge density oscillates between positive and negative values before bulk electroneutrality is achieved, as shown by the orange line in Fig. 3.3.

At even stronger Yukawa interaction strengths but before bulk charge separation, a

densely packed layer of counterions next to the electrode is unable to screen the high surface charge and crowding is observed despite there being no applied potential. At $\alpha = 1.3$, there are two layers of ions with the same charge at each electrode that screen the surface charge, with those layers then overscreened by subsequent layers until the concentration of anions and cations are comparable in the bulk, as shown numerically by the green line in Fig. 3.3 and physically in Fig. 3.5. This extends the EDL to nearly four distinguishable layers.
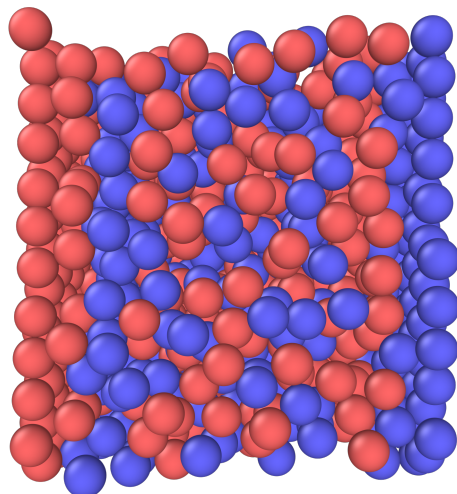
Figure 3.5: Side view of an equilibrated real system for Yukawa interaction strength $\alpha = 1.3$ with $\Delta V = 0$ that has undergone spontaneous surface charge separation.

Surface in-plane ordering without applied potential difference

Two intriguing surface phenomena were observed during SSCS: a transient in-plane microphase separation and a persistent solid-like ion structuring. These phenomena are observed mainly for $\alpha > 1$, or when the Yukawa interaction strength become stronger than the electrostatic interactions at short distances. A comparison of the transition and equilibrium states at different α values in Fig. 3.6 shows that these effects appear to grow stronger as the Yukawa interaction strength increases.

In the SSCS transition, the anions and cations do not migrate directly to their respective electrodes. Instead, they aggregate into local, finite domains on both electrodes that coarsen and grow into either alternating stripes or patches of ions, as shown in Figs. 3.6c and 3.6e, respectively. This diffusive in-plane microphase separation is a metastable state driven by the competition between the short-range effective attraction and the long-range Coulomb repulsion between co-ions, which gives rise to a preferred length scale in the charge density that dictates the size of
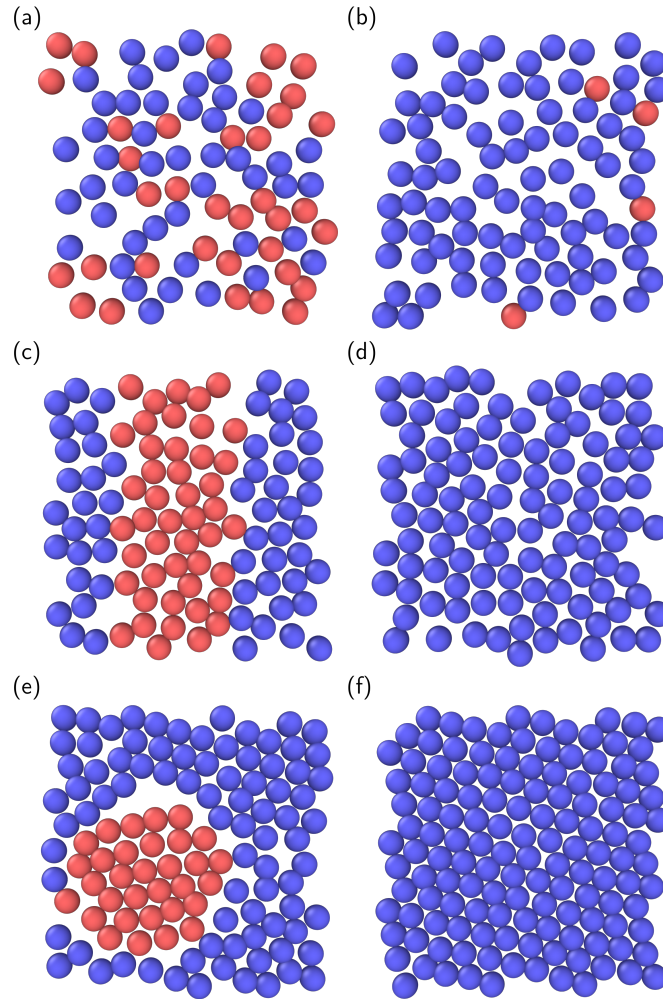
Figure 3.6: Adlayer cross-sections for systems with Yukawa interaction strengths (a, b) $\alpha = 0.8$, (c, d) $\alpha = 1.1$, and (e, f) $\alpha = 1.35$ in the transient and equilibrium states, respectively. The in-plane microphase separation and the solid-like ion structuring on the surfaces are observed when $\alpha > 1$.

the stripes or patches that form. However, each of the adlayers consists only of one type of ion at equilibrium due to the unfavorable Yukawa repulsion between counterions, so the adlayers must be restructured by swapping the less abundant ions for the dominant ions. This in-plane rearrangement is typically much slower than the interplane diffusion that screens the induced surface charge [50]. Fig. 3.7 plots a time trace of the total potential energy from all ion–ion and ion–image charge interactions for a representative $\alpha = 1.3$ system. It not only shows that the equilibrium state is much more energetically favorable than the metastable state, but also confirms that the ion restructuring, which is on the order of microseconds for a typical RTIL, is over an order of magnitude slower than the ion diffusion.
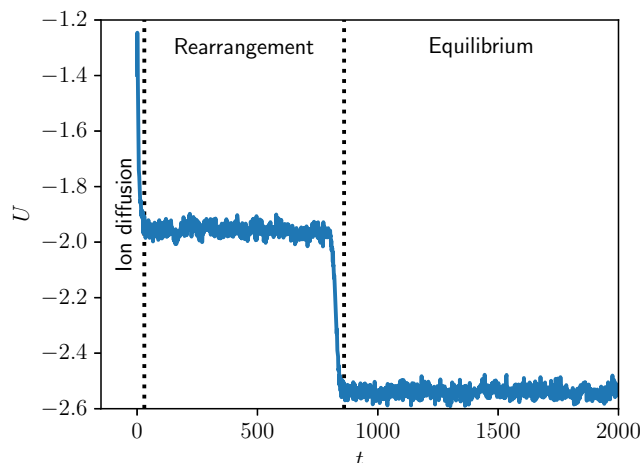
Figure 3.7: Time trace of the extensive potential energy in the real system with Yukawa interaction strength $\alpha = 1.3$ when starting from a homogeneous initial state. The transient metastable and equilibrium states are observed at approximately $t = 30$ and $t = 860$, respectively.

The increased translational ordering on the surfaces is driven by the complex interplay between the image charge effects and pair interactions, as the ionic crystal adlayers are only observed with PC boundaries and are more pronounced with stronger Yukawa interactions. Microscopically, the attractive image charge interactions draw ions to and increases the ion density near the surface, and this interfacial accumulation effect is amplified by the attractive Yukawa interaction between co-ions that favors the close packing of like-charged ions. As a result, the number of like-charged ions found in the adlayers increases with the Yukawa interaction strength, and Fig. 3.8 shows that the surface ion number density ρ_s, which measures the number of ions per electrode area in the adlayers, grows sharply after the transition point. The enhanced lateral interactions from the increasing surface ion number density result in the formation of solid-like adlayers, similar to how hard spheres exhibit a liquid–solid phase transition when the density is sufficiently high [37]. Despite the decrease in the surface ion number density from the voids formed between the like-charged domains due to the increasingly repulsive Yukawa interaction between counterions, the hexagonal packing of ions is *even possible* in the transitional in-plane microphase separation at strong Yukawa interaction strengths, such as $\alpha = 1.35$ as shown in Fig. 3.6e, since the density in each domain is sufficiently high for the ionic crystal to form. Conversely, whenever there is enhanced crystal packing on the surfaces, the in-plane microphase separation is *always* observed during the SSCS transition since the slow dynamics from the solid-like adlayer

formation impedes the EDL rearrangement.
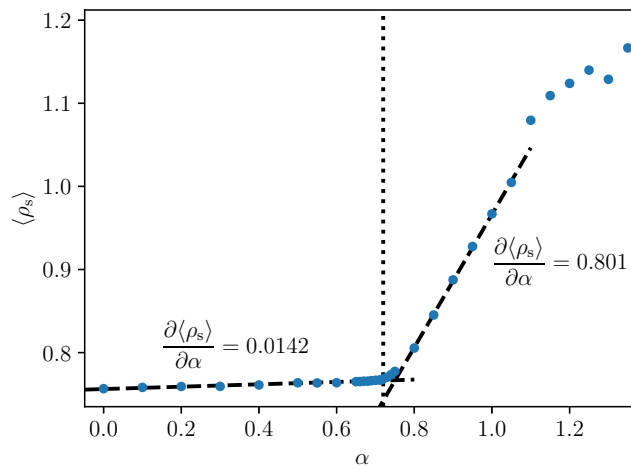
Figure 3.8: Ensemble-averaged surface ion number density $\langle \rho_s \rangle$ as a function of the Yukawa interaction strength α. The dotted line identify the transition point $\alpha_t = 0.72$ of the spontaneous surface charge separation, and the dashed lines show the approximate linear fits in the regions before and after the transition point.

This packing phenomenon could be related to the experimentally observed multi-layered ion structuring on a gold surface for RTILs [51]. Generally, this solid-like adlayer formation is undesired in capacitance applications because it slows down the dynamics at the interface and can be avoided by using disordered and uneven electrodes, which breaks the symmetry between the real and image systems.

With applied potential difference

Electrochemical energy storage devices like EDLCs are charged by applying a potential difference between the two electrodes. In the literature, the potential difference ΔV is commonly modeled by applying a uniform electric field of magnitude $E = \Delta V / L_z$ in the z-direction, which is constant everywhere in the real system and exerts an electrostatic force $\mathbf{f}_i = q_i \mathbf{E}$ on real ion i [44, 52, 53]. Alternatively, the potential difference can be accounted for by placing explicit surface ions with equal but opposite charges at the z-boundaries of the RTIL EDLCs [15, 53–55]. The surface charge densities obtained from the constant potential and constant charge methods are fully consistent with each other, as shown in the Appendix.

In our study, electric fields with strengths $-1 \leq E \leq 1$ were added to the system to model applied potential differences of approximately $-118 \leq \Delta V / V_T \leq 118$, where $V_T \approx 11$ is the thermal voltage in Lennard-Jones units. Since $V_T = k_B T / e$

has a value of 25.9 mV at room temperature (300 K), the range of applied potentials explored spans nearly 6 V in real units, which is in line with the electrochemical window expected for common RTILs [3–7].

To compute the differential capacitance from the surface charge density data collected at a range of ΔV values using the partial derivative definition in Eq. 3.10, the $\langle \sigma_q \rangle$–ΔV relationship was first interpolated using a cubic smoothing spline. Then, the $\langle \sigma_q \rangle$ values are numerically differentiated with respect to the interpolated ΔV values using first-order accurate forward and backward differences for the endpoints and second-order accurate central differences for the interior points. We note that the fluctuation definition in Eq. 3.10 gives consistent results for C_d, and a comparison is available in the Appendix. Fig. 3.9 shows the surface charge density and the differential capacitance at different applied potentials, with the differential capacitance decaying as roughly $\Delta V^{-1/2}$ at large ΔV for all Yukawa interaction strengths α as predicted by Kornyshev [2].

For RTIL systems with $\alpha < \alpha_t$, the C_d–ΔV curves have the well-known bell-shaped profiles that the Kornyshev model predicted for densely packed systems with equisized ions [2]. As α increases, the magnitude of the surface charge density increases at all applied potentials since the increasingly attractive Yukawa interactions between co-ions and the charge fluctuations from the image charge interactions shown in Fig. 3.2 promote charge separation. Consequently, the differential capacitance peak at $\Delta V = 0$ also increases, as shown previously in Fig. 3.2b.

After the transition point $\alpha_t = 0.72$, there is a discontinuous jump in the surface charge density at $\Delta V = 0$ due to the symmetry breaking from SSCS. This first-order transition is accompanied by the emergence of the metastable phase that both the CW and BM models predicted, where there are two surface charge density curves corresponding to the two possible charge separation directions. Naturally, there are also two corresponding differential capacitance curves that cross each other at $\Delta V = 0$, with the systems in the lower branches being more thermodynamically favorable since the charge polarization in the system is aligned with the applied electric field. The metastable systems in the upper branches are possible because the RTIL itself can generate its own electric field with SSCS. However, when the applied field magnitude exceeds that of the intrinsic field and thermal fluctuations can overcome the nucleation barrier for SSCS, the metastable state disappears and the only globally stable state is achieved.

Fig. 3.9 shows that for $\alpha = 0.73$ near the spinodal, there are two green $\langle \sigma_q \rangle$ and
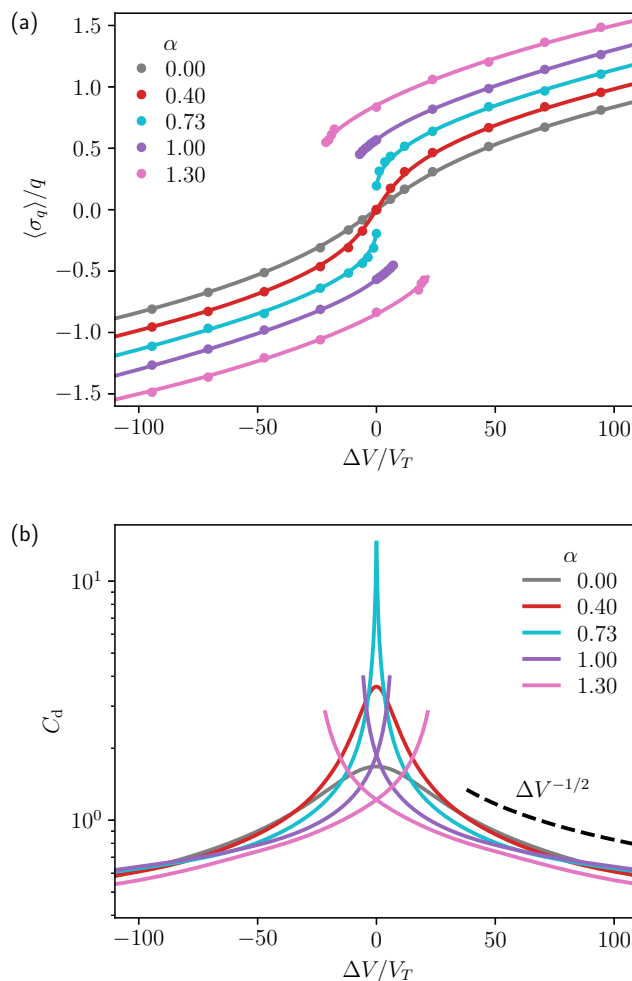
Figure 3.9: (a) Ensemble-averaged surface charge density $\langle \sigma_q \rangle$ and (b) differential capacitance C_{d} as functions of the potential difference ΔV at various Yukawa interaction strengths α. In (a), the dots and lines represent raw data points and fits, respectively.

C_{d} curves with very little overlap in the ΔV space. As α increases further, the metastable region enlarges to a wider range of applied potentials, allowing for the charge separation to be in either direction despite the potential difference. The metastable region can span up to nearly 1.1 V in real units for a strong $\alpha = 1.3$ system, as shown by the purple curves.

These metastable states likely explain the hysteresis in the experimentally measured capacitance of RTIL EDLCs when the charging direction was reversed [56, 57]. Since hysteresis can lead to uncontrolled energy dissipation and SSCS allows for metastable states to exist, SSCS is undesirable in EDLCs and should be prevented by weakening the ion–ion correlations, either by using more chemically compatible

anions and cations or decreasing the incompatibility by adding an organic solvent [19].

Comparison with systems with nonmetal boundaries

To compare with systems without image charge interactions, we removed the image charges to simulate NM boundaries that have the same relative permittivity as the RTIL. With the Yeh–Berkovitz correction for slab systems [58], we continue using the fast PPPM method to evaluate the long-range electrostatic interactions despite the lack of periodicity in the z-direction, but with constant surface charge instead of constant potential so that the system dipole is correctly accounted for. At $\alpha = 0$ and with no applied potential, Fig. 3.10a shows that the dipole distribution becomes sharply peaked, which is indicative of severely diminished charge fluctuations. This result agrees with recent findings [55] that the image charge interactions from using PC boundaries induce greater charge fluctuations that promote charge separation. As such, we expected the onset of SSCS in systems with NM boundaries to be at a Yukawa interaction strength much larger than the $\alpha_t = 0.72$ for systems with PC boundaries.

Surprisingly, SSCS is *not* observed for the range of Yukawa interaction strengths explored ($0 \leq \alpha \leq 1.8$) when the image charges are eliminated, with the surface charge vanishing even at strong Yukawa interaction strengths or when the system starts from a charge-separated state. Fig. 3.10b shows that a system with a strong Yukawa interaction strength $\alpha = 1.6$ develops bicontinuous domains with interpenetrating networks of anions and cations, and Fig. 3.10c shows that a system with an even stronger Yukawa interaction strength $\alpha = 1.8$ undergoes bulk microphase separation, a transition that is also observed in a bulk periodic system with no electrodes as seen in the Appendix.

Therefore, the attractive image charge interactions from PC boundaries play a crucial role in the behavior and energy storage properties of RTIL EDLCs. Observing SSCS requires not only the ion–ion correlations be strong enough to offset the electrostatic interactions at short ranges so that co-ions can pack tightly together on the surfaces, but also a net electrostatic attraction of the ions to the interface by the image charge interactions. The results show that RTIL EDLCs with NM boundaries have very low polarizability even with strong Yukawa interaction strengths and applied potentials, but can remarkably charge separate at $\Delta V = 0$ with PC boundaries due to the increased charge fluctuations from the image charge interactions.
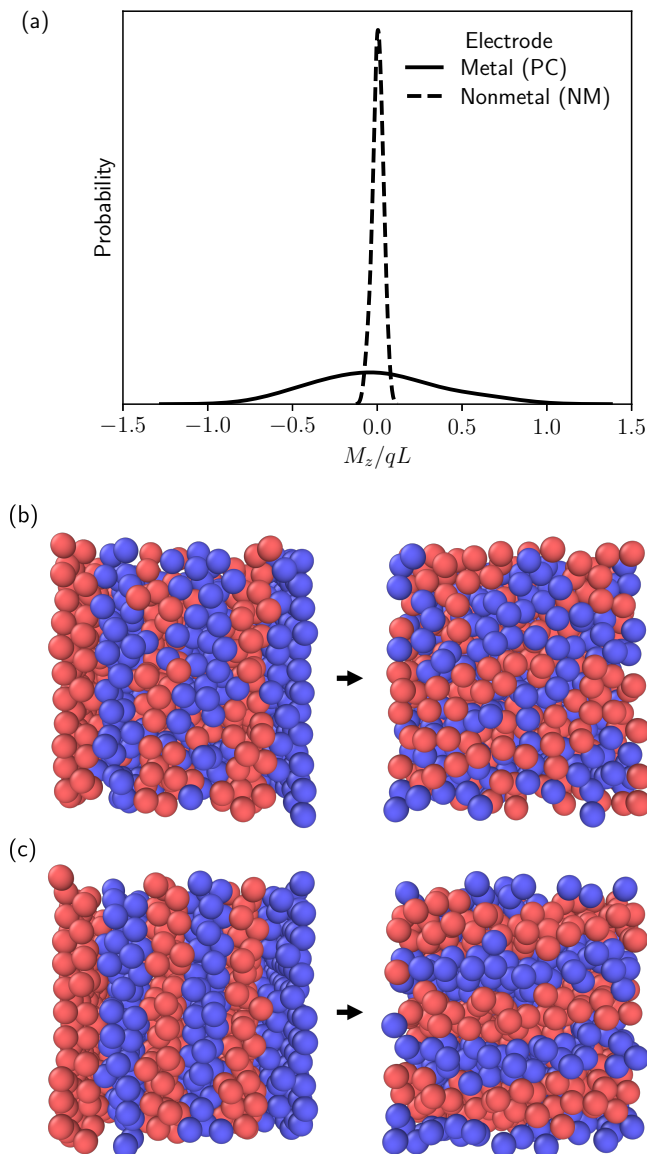
Figure 3.10: (a) Comparison of charge fluctuations with perfectly conducting and nonmetal boundaries at $\alpha = 0$ and $\Delta V = 0$, and system screenshots of the starting charge-separated (left) and equilibrium states (right) for (b) $\alpha = 1.6$ and (c) $\alpha = 1.8$ with $\Delta V = 0$ and nonmetal boundaries.

3.4 Conclusion

In conclusion, we have conducted MD simulations to directly simulate the behavior of RTIL EDLCs with metal boundaries in the absence of any mean-field approximations. The coarse-grained RTIL model that we constructed incorporates the ion–ion correlations using short-range Yukawa interactions—as was done in the previous MFTs—and accounts for the PC boundaries using the method of image charges.

Using our model, we observed a SSCS transition with no applied potential driven by the coupling of the ion–ion correlations in RTILs and the enhanced charge fluctuations from the image charge interactions. Consequently, we also saw metastable charge-separated states with applied potentials since the intrinsic electric field from SSCS can either amplify or counteract the applied field, depending on the alignment of the system dipole with the field direction. The behavior of these transitions is qualitatively consistent with those predicted in the CW and BM models.

Interestingly, we discovered a prominent surface in-plane structuring with no applied potential as the Yukawa interaction strength increased. With the image charge interactions drawing the ions to the interface, the competition between the short-range Yukawa interactions and the long-range electrostatics causes a transient surface in-plane microphase separation, while the increased lateral interactions from the higher surface ion number density lead to increased translational order in the adlayers that was present in both the transitional and equilibrium states. Although the in-plane microphase separation was sometimes observed without the increased translational order, the enhanced crystal packing was always accompanied by the in-plane microphase separation.

Perhaps most importantly, we found that the electrode boundary condition has a large influence on the behavior and properties of RTIL EDLCs, in that the enhanced charge fluctuations with PC boundaries make the RTILs more susceptible to applied potentials. By removing the attractive image charge interactions to simulate a NM boundary with the same relative permittivity as the RTIL, we did not observe SSCS even with very strong Yukawa interaction strengths.

While the current model has identified the key effects of image charge interactions, it does not account for important effects and properties that can affect the EDL structure and dynamics, such as the ion asymmetry [2, 15], structure, and polarizability [55, 59–62]. However, previous MFTs [19, 63] analogous to our coarse-grained model show that SSCS should be a common feature of RTIL EDLCs and that the anomalous increase in capacitance observed experimentally [64] in RTIL EDLCs under confinement can be explained when they have undergone SSCS. These results indirectly suggest that the key findings of this chapter are relevant in real RTILs despite the simplifications used in our model. Nevertheless, more detailed atomistic simulations using polarizable force fields [65, 66] that capture the specific chemistries of common RTILs would highlight the molecular mechanisms of the EDL formation in real RTILs and associate the interaction parameters in the coarse-

grained models with the molecular properties of the RTILs. These comprehensive simulations would also reveal how ion transport properties and charging dynamics of RTILs are affected by the image charge effects from the metal electrodes and help guide the design of optimized RTIL EDLCs.

3.5 Appendix

Reduced Lennard-Jones units

The fundamental quantities are the mass m, the particle size σ, and the energy scale ϵ. The reduced units for the basic and derived parameters are tabulated in Table 3.1.

Basic parameter	Reduced unit	Derived parameter	Reduced unit
Distance	$r^* = \dfrac{r}{\sigma}$	Charge density	$\rho_q^* = \dfrac{\sigma^3}{\sqrt{4\pi\varepsilon_0\sigma\epsilon}}\rho_q$
Energy	$U^* = \dfrac{U}{\epsilon}$	Surface charge density	$\sigma_q^* = \dfrac{\sigma^2}{\sqrt{4\pi\varepsilon_0\sigma\epsilon}}\sigma_q$
Number density	$\rho^* = \rho\sigma^3$	Electric dipole	$M_z^* = \dfrac{M_z}{\sigma\sqrt{4\pi\varepsilon_0\sigma\epsilon}}$
Temperature	$T^* = \dfrac{k_B T}{\epsilon}$	Electric field	$E^* = \dfrac{\sigma\sqrt{4\pi\varepsilon_0\sigma\epsilon}}{\epsilon}E$
Time	$t^* = t\sqrt{\dfrac{\epsilon}{m\sigma^2}}$	Voltage	$V^* = \dfrac{\sqrt{4\pi\varepsilon_0\sigma\epsilon}}{\epsilon}V$
Charge	$q^* = \dfrac{q}{\sqrt{4\pi\varepsilon_0\sigma\epsilon}}$	Differential capacitance	$C_d^* = \dfrac{\sigma}{4\pi\varepsilon_0}C_d$

Table 3.1: Relevant physical quantities expressed in reduced Lennard-Jones units.

Using the reduced units in Table 3.1, the key dimensionless quantities and equations in the main text are derived as follows. The $*$ superscript denotes a dimensionless quantity (but has been excluded in the main text for convenience).

Timescale

For common RTILs like [EMIM$^+$][BF$_4^-$] or [EMIM$^+$][NTf$_2^-$], the average dimension is approximately $\sigma = 0.6 \times 10^{-9}$ m and the average molecular weight is on the order

of $m = 300$ g/mol [67]. At room temperature (300 K), the relevant timescale is

$$\tau = \sqrt{\frac{m\sigma^2}{\epsilon}} = \sqrt{\frac{\left((300\,\text{g/mol})/(6.022 \times 10^{23}\,\text{mol}^{-1})\right)(0.6\,\text{nm})^2}{(1.380649 \times 10^{-23}\,\text{J/K})(300\,\text{K})}} \approx 6.6\,\text{ps},$$

which is on the order of picoseconds.

Bjerrum length

The reduced Bjerrum length λ_B^* is

$$\lambda_B^* = \frac{\lambda_B}{\sigma} = \frac{1}{\sigma}\left(\frac{e^2}{4\pi\varepsilon_0\varepsilon_r k_B T}\right)$$

$$= \frac{\left(\sqrt{4\pi\varepsilon_0\sigma\epsilon}\,e^*\right)^2}{4\pi\varepsilon_0\varepsilon_r\,(\epsilon T^*)\,\sigma} = \frac{4\pi\varepsilon_0\sigma\epsilon(e^*)^2}{4\pi\varepsilon_0\sigma\epsilon\varepsilon_r T^*}$$

$$= \frac{(e^*)^2}{\varepsilon_r T^*}$$

Coulomb potential

The reduced Coulomb potential U_{Coul}^* (Eq. 3.2) is

$$U_{\text{Coul}}^* = \frac{U_{\text{Coul}}}{\epsilon} = \frac{1}{\epsilon}\left(\frac{q_i q_j}{4\pi\varepsilon_0\varepsilon_r r_{ij}}\right)$$

$$= \frac{\left(\sqrt{4\pi\varepsilon_0\sigma\epsilon}\,q_i^*\right)\left(\sqrt{4\pi\varepsilon_0\sigma\epsilon}\,q_j^*\right)}{4\pi\varepsilon_0\varepsilon_r\left(\sigma r_{ij}^*\right)\epsilon} = \frac{4\pi\varepsilon_0\sigma\epsilon q_i^* q_j^*}{4\pi\varepsilon_0\sigma\epsilon\varepsilon_r r_{ij}^*}$$

$$= \frac{q_i^* q_j^*}{\varepsilon_r r_{ij}^*}$$

With $q = ze$, the reduced Coulomb potential can also be expressed in terms of the reduced Bjerrum length:

$$U_{\text{Coul}}^* = \frac{(z_i e^*)\,(z_j e^*)}{\varepsilon_r r_{ij}^*}\left(\frac{T^*}{T^*}\right) = \frac{z_i z_j T^*}{r_{ij}^*}\frac{(e^*)^2}{\varepsilon_r T^*} = \frac{z_i z_j \lambda_B T^*}{r_{ij}^*}$$

For symmetric monovalent ions ($z_i = \pm 1$ or $q_i = \pm e$), the magnitude of the reduced charge is given by equating the two definitions of the Coulomb potential above:

$$\frac{q_i^* q_j^*}{\varepsilon_r r_{ij}^*} = \frac{z_i z_j \lambda_B T^*}{r_{ij}^*} \implies q^* = \sqrt{\varepsilon_r \lambda_B T^*}$$

WCA potential

For $r_{ij} \leq 2^{1/6}\sigma$, the reduced WCA potential U_{WCA}^* (Eq. 3.4) is

$$U_{\text{WCA}}^* = \frac{U_{\text{WCA}}}{\epsilon} = \frac{1}{\epsilon}\left(4\epsilon_{ij}\left[\left(\frac{\sigma_{ij}}{r_{ij}}\right)^{12} - \left(\frac{\sigma_{ij}}{r_{ij}}\right)^{6}\right] + \epsilon_{ij}\right)$$

$$= 4\epsilon_{ij}^*\left[\left(\frac{\sigma\sigma_{ij}^*}{\sigma r_{ij}^*}\right)^{12} - \left(\frac{\sigma\sigma_{ij}^*}{\sigma r_{ij}^*}\right)^{6}\right] + \epsilon_{ij}^*$$

$$= 4\epsilon_{ij}^*\left[\left(\frac{\sigma_{ij}^*}{r_{ij}^*}\right)^{12} - \left(\frac{\sigma_{ij}^*}{r_{ij}^*}\right)^{6}\right] + \epsilon_{ij}^*$$

Gaussian potential

For $r_{ij} \leq \sigma$, the reduced Gaussian potential U_{Gauss}^* (Eq. 3.5) is

$$U_{\text{Gauss}}^* = \frac{U_{\text{Gauss}}}{\epsilon} = \frac{1}{\epsilon}\left(A_{ij}\left[\exp\left(-B_{ij}r_{ij}^2\right) - \exp\left(-\sigma^2 B_{ij}\right)\right]\right)$$

$$= A_{ij}^*\left[\exp\left(-\left(B_{ij}^*/\sigma^2\right)\left(\sigma r_{ij}^*\right)^2\right) - \exp\left(-\sigma^2\left(B_{ij}^*/\sigma^2\right)\right)\right]$$

$$= A_{ij}^*\left[\exp\left(-B_{ij}^*(r_{ij}^*)^2\right) - \exp\left(-B_{ij}^*\right)\right]$$

Yukawa potential

The reduced Yukawa potential U_{Yukawa}^* (Eq. 3.6) is

$$U_{\text{Yukawa}}^* = \frac{U_{\text{Yukawa}}}{\epsilon} = \frac{1}{\epsilon}\left(-\alpha\frac{q_i q_j}{4\pi\varepsilon_0\varepsilon_r r_{ij}}\left[\exp\left(-r_{ij}/\ell_c\right) - \exp\left(-L_z/(2\ell_c)\right)\right]\right)$$

$$= -\alpha\frac{z_i z_j \lambda_{\text{B}} T^*}{r_{ij}^*}\left[\exp\left(-\left(\sigma r_{ij}^*\right)/(\sigma\ell_c^*)\right) - \exp\left(-\left(\sigma L_z^*\right)/(2\sigma\ell_c^*)\right)\right]$$

$$= -\alpha\frac{z_i z_j \lambda_{\text{B}} T^*}{r_{ij}^*}\left[\exp\left(-r_{ij}^*/\ell_c^*\right) - \exp\left(-L_z^*/(2\ell_c^*)\right)\right]$$

Debye length

With $\rho = \rho_+^{\text{bulk}} + \rho_-^{\text{bulk}}$ and $z_i = \pm1$, the reduced Debye length λ_{D}^* is

$$\lambda_{\text{D}}^* = \frac{\lambda_{\text{D}}}{\sigma} = \frac{1}{\sigma}\left(\frac{e^2}{\varepsilon_0\varepsilon_r k_{\text{B}}T}\left(\rho_+^{\text{bulk}}z_+^2 + \rho_-^{\text{bulk}}z_-^2\right)\right)^{-1/2} = \frac{1}{\sigma}\left(4\pi\lambda_{\text{B}}\rho\right)^{-1/2}$$

$$= \left(4\pi\sigma^2\left(\sigma\lambda_{\text{B}}^*\right)\left(\rho^*/\sigma^3\right)\right)^{-1/2}$$

$$= \left(4\pi\lambda_{\text{B}}^*\rho^*\right)^{-1/2}$$

Surface charge density

The reduced surface charge density σ_q^* (Eq. 3.8) is

$$\sigma_q^* = \frac{\sigma^2}{\sqrt{4\pi\varepsilon_0\sigma\epsilon}}\sigma_q = \frac{\sigma^2}{\sqrt{4\pi\varepsilon_0\sigma\epsilon}}\left(\frac{\varepsilon_0\varepsilon_r\Delta V}{L_z} - \frac{1}{L_z}\int_0^{L_z} z\rho_q\,dz\right)$$

$$= \frac{\sigma^2}{\sqrt{4\pi\varepsilon_0\sigma\epsilon}}\left(\frac{\varepsilon_0\varepsilon_r\left(\epsilon\Delta V^*/\sqrt{4\pi\varepsilon_0\sigma\epsilon}\right)}{\sigma L_z^*} - \frac{1}{\sigma L_z^*}\int_0^{L_z^*}(\sigma z^*)\left(\frac{\sqrt{4\pi\varepsilon_0\sigma\epsilon}\rho_q^*}{\sigma^3}\right)dz^*\right)$$

$$= \frac{\varepsilon_r\Delta V^*}{4\pi L_z^*} - \frac{1}{L_z^*}\int_0^{L_z^*} z^*\rho_q^*\,dz^*$$

Differential capacitance

The reduced partial derivative definition of differential capacitance C_d^* (Eq. 3.10) is

$$C_d^* = \frac{\sigma}{4\pi\varepsilon_0}C_d = \frac{\sigma}{4\pi\varepsilon_0}\left(\frac{L_xL_y}{k_BT}\langle(\delta\sigma_q)^2\rangle\right)$$

$$= \frac{\sigma}{4\pi\varepsilon_0}\left(\frac{(\sigma L_x^*)(\sigma L_y^*)}{\epsilon T^*}\left\langle\left(\frac{\sqrt{4\pi\varepsilon_0\sigma\epsilon}}{\sigma^2}\delta\sigma_q^*\right)^2\right\rangle\right)$$

$$= \frac{L_x^*L_y^*}{T^*}\langle(\delta\sigma_q^*)^2\rangle$$

Thermal voltage

The reduced thermal voltage V_T^* is

$$V_T^* = \frac{\sqrt{4\pi\varepsilon_0\sigma\epsilon}}{\epsilon}V_T = \frac{\sqrt{4\pi\varepsilon_0\sigma\epsilon}}{\epsilon}\left(\frac{k_BT}{e}\right) = \frac{\sqrt{4\pi\varepsilon_0\sigma\epsilon}}{\epsilon}\left(\frac{\epsilon T^*}{\sqrt{4\pi\varepsilon_0\sigma\epsilon}e^*}\right) = \frac{T^*}{e^*}$$

Finite size effect

The finite size effect in our systems should be minimal. In Fig. 3.3 of the main text, all the charge density profiles reach bulk electroneutrality and are flat in the center of the system. Furthermore, we ran additional simulations using an $\alpha = 1.3$ system elongated in the z-direction with dimensions $7.617 \times 7.617 \times 21.5443$, and the calculated surface charge density is comparable to that from the cubic $10.77 \times 10.77 \times 10.77$ systems. System screenshots and charge density profiles are shown in Fig. 3.11.

Determining the transition point

For systems with no applied potential, the transition point α_t was determined by analyzing the evolution of the charge densities in the left and right halves of the real
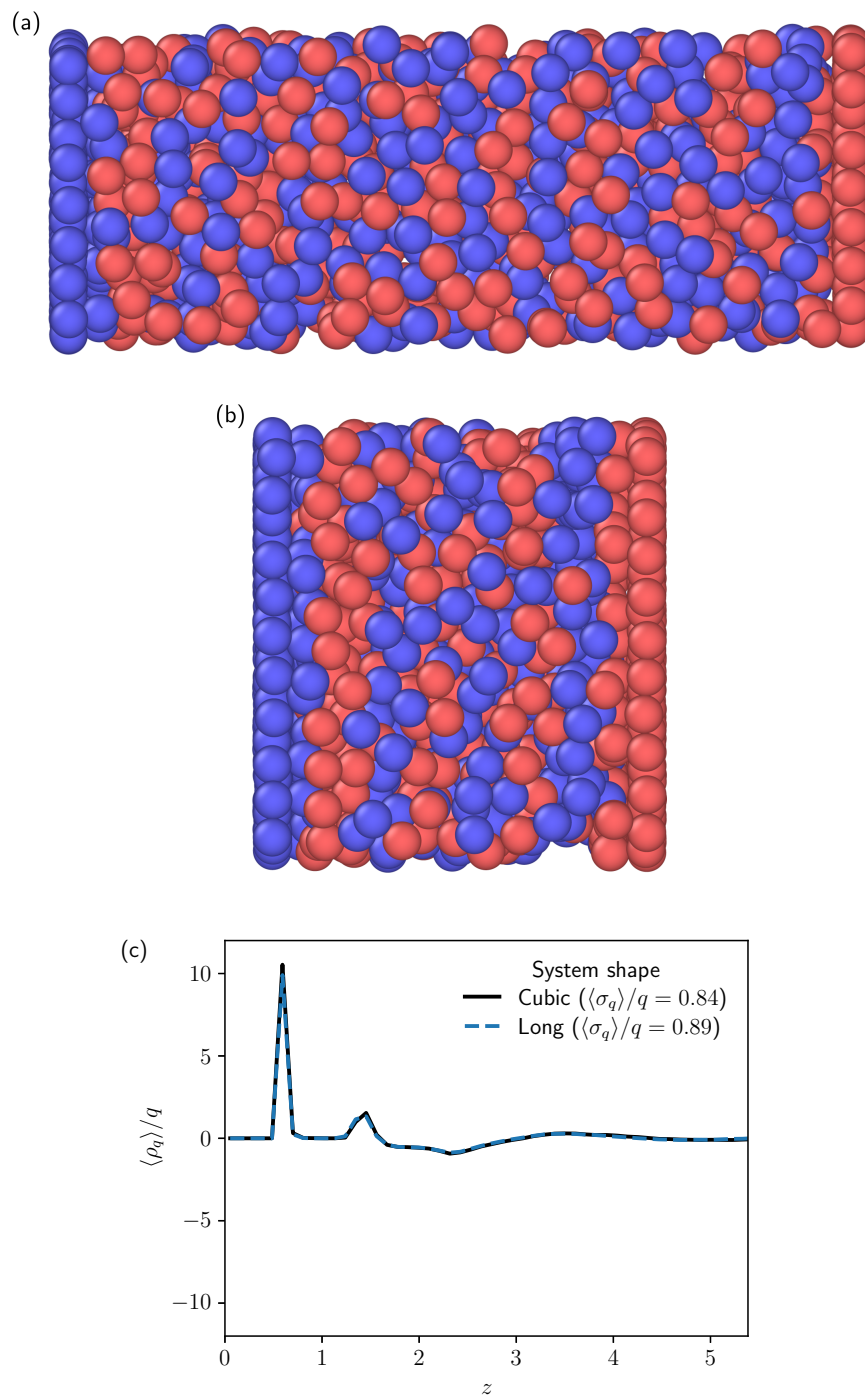
Figure 3.11: Visualization of the (a) elongated real system and (b) cubic real system used in the main text with Yukawa interaction strength $\alpha = 1.3$ and $\Delta V = 0$. (c) Ensemble-averaged surface charge density $\langle \sigma_q \rangle$ near the left electrode for the two systems in (a) and (b).

system, which are given by

$$
\rho_q^{\text{half}}(t) = \begin{cases} \dfrac{2}{L_z} \displaystyle\int_0^{L_z/2} \rho_q(z,t)\,dz, & \text{left} \\[3mm] \dfrac{2}{L_z} \displaystyle\int_{L_z/2}^{L_z} \rho_q(z,t)\,dz, & \text{right} \end{cases}, \tag{3.11}
$$

where L_z is the length of the real system in the z-direction and $\rho_q(z,t)$ is the instantaneous local charge density profile.

In Fig. 3.12, the time traces of the half-system charge densities $\rho_q^{\text{half}}(t)$ are shown for RTILs with Yukawa interaction strengths $\alpha = 0.71$, $\alpha = 0.72$, and $\alpha = 0.74$. $\rho_q^{\text{half}}(0)$ is non-zero because the simulations were started from charge-separated states, and the top (resp. bottom) rows correspond to systems that started with the anions (resp. cation) accumulated on the left (resp. right) electrode.

For systems before the transition point, such as the $\alpha = 0.71$ systems in Fig. 3.12a, the initial charge separation is rarely maintained, with the surface charges quickly dissipating to form either thermodynamically favorable homogeneous or fluctuation-driven weakly charge-separated states. As such, the homogeneous state is the most probable state, leading to the unimodal dipole distributions seen in Fig. 3.2c of the main text. However, for the systems at $\alpha = 0.72$ shown in Fig. 3.12b, the initial charge separation either persists or reverses direction, forming transient homogeneous states in the process. As a result, the unimodal dipole distribution turns into a bimodal distribution since the charge-separated state is more common and long-lived than the metastable homogeneous state. The metastability of both the ordered and disordered states and the bimodal nature of the dipole distribution suggest that the transition at $\alpha_t = 0.72$ is weakly first-ordered [48].

Fig. 3.8 in the main text also supports the conclusion that the transition point is at $\alpha = 0.72$. While the surface ion number density increased slowly with the Yukawa correlation strength for $\alpha < 0.72$, it grew sharply after $\alpha = 0.72$, with $\partial \rho_s / \partial \alpha$ being over an order of magnitude greater. This is driven by the SSCS possible after the transition point and the stronger Yukawa interactions, which favor the close packing of co-ions and induces a greater accumulation effect on the surfaces.

For systems past the transition point and the spinodal for the homogeneous state, such as the $\alpha = 0.74$ systems shown in Fig. 3.12c, the initial charge separation direction is maintained throughout the entire simulation and the homogeneous state is not observed. While the dipole distribution is still bimodal due to the two possible SSCS directions, charge reversal is very improbable.
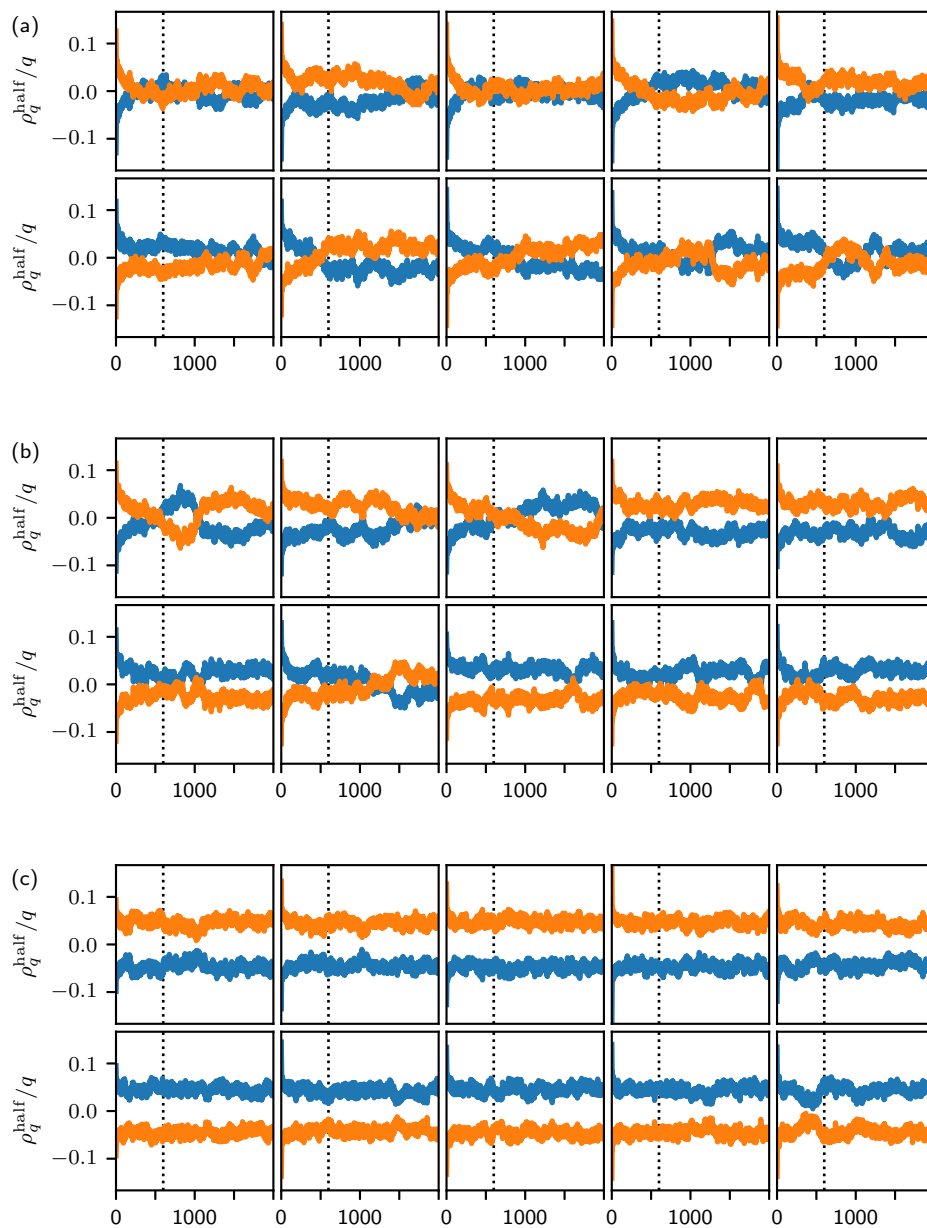
Figure 3.12: Time traces of the charge densities in the left (blue) and right (orange) halves of the real system for Yukawa interaction strengths (a) $\alpha = 0.71$, (b) $\alpha = 0.72$, and (c) $\alpha = 0.74$. The dotted lines show when production data collection begins.
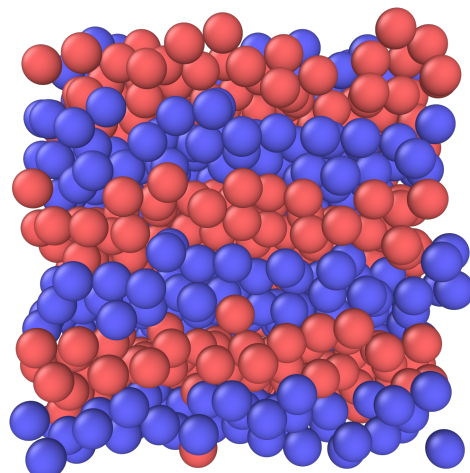
Figure 3.13: Visualization of an equilibrated fully periodic bulk system for Yukawa interaction strength $\alpha = 1.8$ with $\Delta V = 0$.

Due to the symmetry in the RTILs, the charge density profiles for systems after the transition point were sign-corrected so that the ρ_q is positive and negative on the left and right electrodes, respectively. For systems with the opposite charge separation direction, the charge density profiles were flipped in the z-direction, equivalent to exchanging the identities of the anions and cations or swapping the signs on the calculated surface charge densities and system dipoles. This data processing results in the single positive $\langle \sigma_q \rangle$–α curve and the corresponding dipole distributions for $\alpha > \alpha_t$ in Fig. 3.2 of the main text.

Bulk phase separation at strong Yukawa interaction strengths

The equilibrium state for an $\alpha = 1.8$ system with NM boundaries is the same as a bulk $\alpha = 1.8$ system that has underwent a bulk phase separation, as shown in Fig. 3.10c in the main text and Fig. 3.13.

Constant potential vs. constant charge simulations

While the potential difference was modeled using an electric field in the main text, it can also be induced by placing explicit ions with opposite but equal charges $\pm q_s$ on the opposing electrode surfaces. The single layer of surface ions is found at $z = 0$ and $z = L_z$, and is arranged on a hexagonal close-packed (HCP) lattice with spacing $(1/2, \sqrt{3}/4, \sqrt{6}/6)$. With this configuration, the surface ions achieve the maximum packing density for spheres when they have the same interaction range $\sigma_{ij} = 0.5$ as the smooth electrodes used in the electric field case, and this close-packing of the

surface ions minimizes the electric field variations in the x- and y-directions due to the discrete nature of the surface charge. To accommodate the periodicity of the HCP lattice in the x- and y-directions, the real system is no longer perfectly cubic; instead, it has dimensions $L_x = 11$, $L_y = 6\sqrt{3} \approx 10.39$, and $L_z = 9\sqrt{6}/2 \approx 11.02$, which works out to $N_s = 528$ surface ions on each electrode. With $N = 1,000$ ions and a volume of $V = L_x L_y L_z \approx 1,260.06$, the ion number density is $\rho \approx 0.79$, which is comparable to the $\rho = 0.8$ used in the main text.

For systems with perfectly conducting electrodes, the charges on the surface ions can be associated with the electric field through the surface charge density. As shown in Eq. 3.8 of the main text, the total surface charge density $\langle \sigma_q \rangle$ can be separated into a static part σ_q^s and a polarization part $\langle \sigma_q^p \rangle$ [44, 45]. With $\langle \sigma_q^p \rangle$ representing the average charge dipole in the real system, only the static surface charge density is related to the applied electric field through $4\pi\sigma_q^s = \varepsilon_r E$ and is used to determine the charges of the explicit surface ions via

$$\frac{q_s}{2} = \frac{A\sigma_q^s}{N_s} = \frac{L_x L_y \varepsilon_r E}{4\pi N_s}, \tag{3.12}$$

where $A = L_x L_y$ is the electrode area and the 2 in the numerator is a scaling factor that must be included for systems with image charge interactions when using a three-dimensional Ewald summation method to evaluate the Coulomb interactions since only half of the calculated energy of the repeat unit should translate to the electrostatic forces on the real ions [44, 55].

These two methods are compared by testing four distinct system configurations: 1) an $11.00 \times 10.39 \times 11.02$ real system with an applied electric field and smooth metal electrodes, 2) a $10.77 \times 10.77 \times 10.77$ cubic real system with an applied electric field and smooth metal electrodes, 3) an $11.00 \times 10.39 \times 11.02$ real system with explicit surface charges and uneven metal electrodes, and 4) an $11.00 \times 10.39 \times 11.02$ real system with explicit surface charges and smooth metal electrodes. For the first two systems, the electrodes are idealized surfaces that interact with the real ions using a WCA potential with $\sigma_{ij} = 0.5$ and $\epsilon_{ij} = 100$, as outlined in the main text. In the third system, the electrodes are uneven due to the spherical surface ions, which interact with the real ions via both the previous WCA potential and a Coulomb potential (Eq. 3.2 of the main text). In the fourth system, the surface ions are embedded within an idealized surface with the same interaction potential as the first two systems. Because the excluded volume interactions are accounted for by the
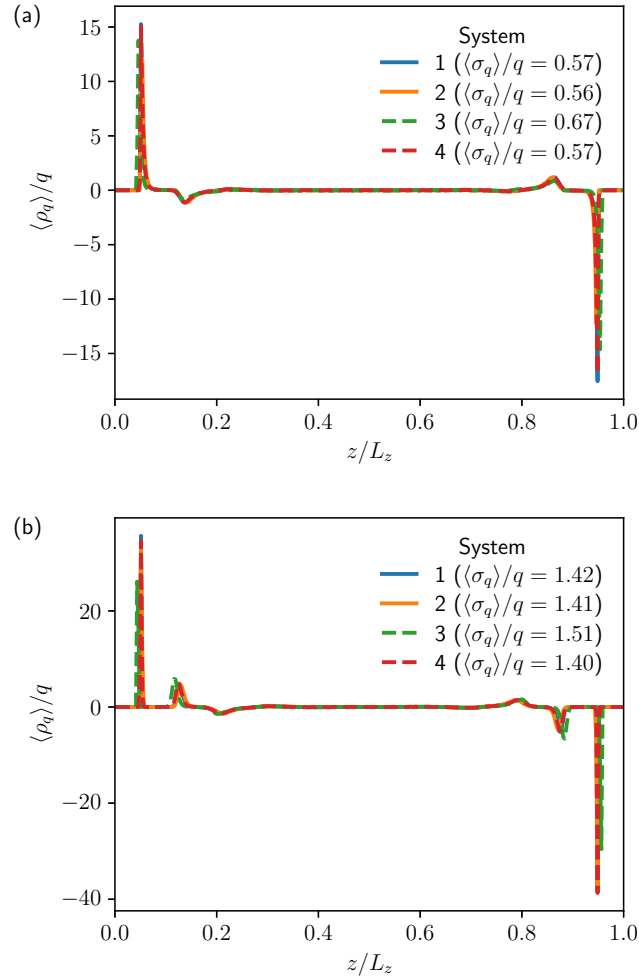
Figure 3.14: Ensemble-averaged charge density profiles $\langle \rho_q \rangle$ for systems with Yukawa interaction strength $\alpha = 1$ and (a) no external field ($E = 0$) or (b) an electric field with magnitude $E = 1$ for four distinct system configurations.

idealized surface, the surface ions only interact electrostatically with the real ions via the Coulomb potential.

Fig. 3.14 compares the charge density profiles computed with 400 bins for the four system configurations with applied electric fields of magnitudes $E = 0$ and $E = 1$. It shows that systems 1, 2, and 4 have fully consistent charge density profiles for both electric field strengths tested, indicating that the different approaches of applying the potential difference and the slight asymmetry in the box dimensions do not affect the EDL structure in the RTILs. Despite its charge density profile being very similar in magnitude and shape with the other systems, system 3 has a higher total surface charge density because the real ions in the adlayers are able to get closer

to their corresponding image charges by positioning themselves in the hollows on the surface. While this explicit surface charge model more accurately represent the discrete atoms that constitute the metal electrode, it introduces the unevenness or curvature of the surface, which is outside the scope of the current study and complicates the underlying physics, and is much more computationally expensive due to the addition of $2N_\mathrm{s} = 1,056$ surface ions. As such, the systems in our study were modeled as cubic real systems with applied electric fields for simplicity and computational performance.

Comparison of differential capacitance definitions

As defined in Eq. 11 of the main text, the differential capacitance C_d can be computed either by interpolating and then numerically differentiating the surface charge density $\langle \sigma_q \rangle$ with respect to the potential difference ΔV or by calculating the average mean-square surface charge density fluctuation $\langle (\delta \sigma_q)^2 \rangle$ [48]. Fig. 3.15 shows that the C_d values evaluated using the two definitions for RTIL EDLCs with varying Yukawa interaction strengths are largely consistent with each other.
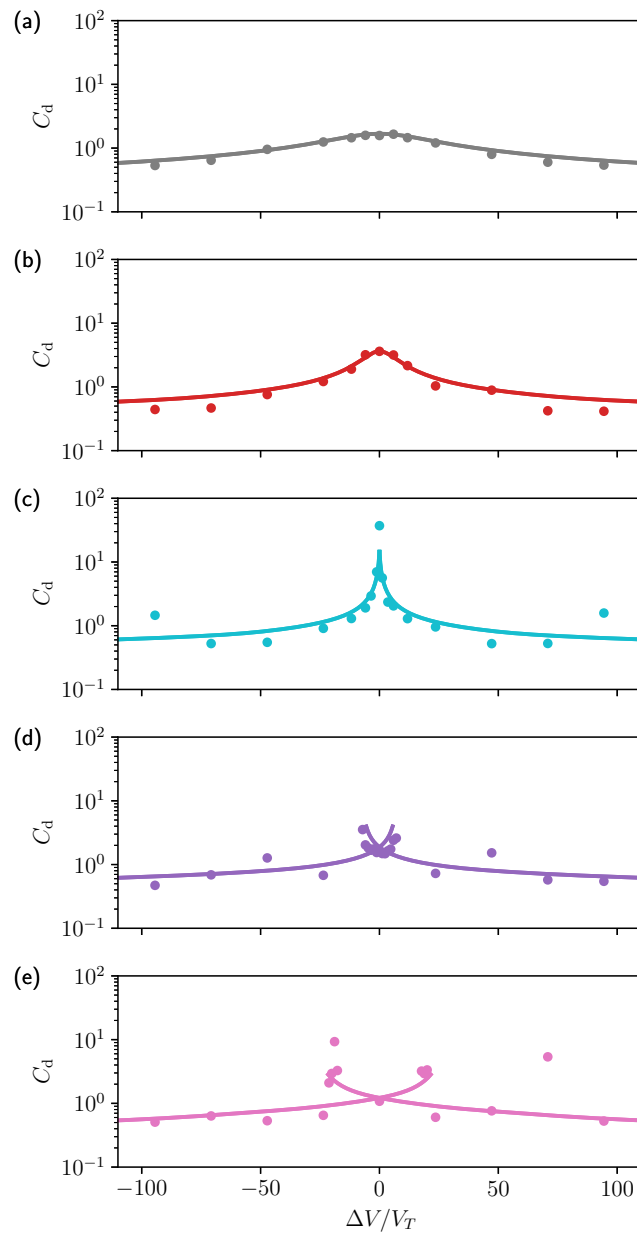
Figure 3.15: Differential capacitance C_d as a function of the potential difference ΔV for systems with Yukawa interaction strengths (a) $\alpha = 0$, (b) $\alpha = 0.4$, (c) $\alpha = 0.73$, (d) $\alpha = 1$, and (e) $\alpha = 1.3$. The lines and dots represent the interpolated and differentiated $\langle \sigma_q \rangle$–ΔV relationship and the C_d calculated using the mean-square surface charge density fluctuations, respectively.

References

(1) Ye, B. B.; Wang, Z.-G. *Phys. Chem. Chem. Phys.* **2022**, *24*, 11573–11584, DOI: `10.1039/D2CP00166G`.

(2) Kornyshev, A. A. *J. Phys. Chem. B* **2007**, *111*, 5545–5557, DOI: `10.1021/jp067857o`.

(3) Suarez, P. A.; Selbach, V. M.; Dullius, J. E., et al. *Electrochim. Acta* **1997**, *42*, 2533–2535, DOI: `10.1016/S0013-4686(96)00444-6`.

(4) Barisci, J. *Electrochem. Commun.* **2004**, *6*, 22–27, DOI: `10.1016/j.elecom.2003.09.015`.

(5) Sato, T.; Masuda, G.; Takagi, K. *Electrochim. Acta* **2004**, *49*, 3603–3611, DOI: `10.1016/j.electacta.2004.03.030`.

(6) Van Aken, K. L.; Beidaghi, M.; Gogotsi, Y. *Angew. Chem. Int. Ed.* **2015**, *54*, 4806–4809, DOI: `10.1002/anie.201412257`.

(7) Mousavi, M. P. S.; Wilson, B. E.; Kashefolgheta, S., et al. *ACS Appl. Mater. Interfaces* **2016**, *8*, 3396–3406, DOI: `10.1021/acsami.5b11353`.

(8) Arbizzani, C.; Biso, M.; Cericola, D., et al. *J. Power Sources* **2008**, *185*, 1575–1579, DOI: `10.1016/j.jpowsour.2008.09.016`.

(9) Ruiz, V.; Huynh, T.; Sivakkumar, S. R.; Pandolfo, A. G. *RSC Adv.* **2012**, *2*, 5591, DOI: `10.1039/c2ra20177a`.

(10) Pell, W.; Conway, B. *J. Power Sources* **1996**, *63*, 255–266, DOI: `10.1016/S0378-7753(96)02525-6`.

(11) Christen, T.; Carlen, M. W. *J. Power Sources* **2000**, *91*, 210–216, DOI: `10.1016/S0378-7753(00)00474-2`.

(12) Cui, J.; Kobayashi, T.; Sacci, R. L., et al. *J. Phys. Chem. B* **2020**, *124*, 9931–9937, DOI: `10.1021/acs.jpcb.0c07582`.

(13) Gouy, M. *J. Phys. Theor. Appl.* **1910**, *9*, 457–468, DOI: `10.1051/jphystap:019100090045700`.

(14) Chapman, D. L. *Lond. Edinb. Dubl. Phil. Mag.* **1913**, *25*, 475–481, DOI: `10.1080/14786440408634187`.

(15) Fedorov, M. V.; Kornyshev, A. A. *J. Phys. Chem. B* **2008**, *112*, 11868–11872, DOI: `10.1021/jp803440q`.

(16) Fedorov, M. V.; Kornyshev, A. A. *Electrochim. Acta* **2008**, *53*, 6835–6840, DOI: `10.1016/j.electacta.2008.02.065`.

(17) Begić, S.; Chen, F.; Jónsson, E.; Forsyth, M. *Phys. Rev. Mater.* **2019**, *3*, 095801, DOI: `10.1103/PhysRevMaterials.3.095801`.

(18) Lee, A. A.; Perkin, S. *J. Phys. Chem. Lett.* **2016**, *7*, 2753–2757, DOI: `10.1021/acs.jpclett.6b01324`.

(19) Chao, H.; Wang, Z.-G. *J. Phys. Chem. Lett.* **2020**, *11*, 1767–1772, DOI: `10.1021/acs.jpclett.0c00023`.

(20) Zhong, Y.-X.; Yan, J.-W.; Li, M.-G., et al. *J. Am. Chem. Soc.* **2014**, *136*, 14682–14685, DOI: `10.1021/ja508222m`.

(21) Li, M.-G.; Chen, L.; Zhong, Y.-X., et al. *Electrochim. Acta* **2016**, *197*, 282–289, DOI: `10.1016/j.electacta.2015.12.227`.

(22) Netz, R.; Orland, H. *Eur. Phys. J. E* **2000**, *1*, 203, DOI: `10.1007/s101890050023`.

(23) Levin, Y. *Rep. Prog. Phys.* **2002**, *65*, 1577–1632, DOI: `10.1088/0034-4885/65/11/201`.

(24) Santangelo, C. D. *Phys. Rev. E* **2006**, *73*, 041512, DOI: `10.1103/PhysRevE.73.041512`.

(25) Mezger, M.; Schroder, H.; Reichert, H., et al. *Science* **2008**, *322*, 424–428, DOI: `10.1126/science.1164502`.

(26) Skinner, B.; Loth, M. S.; Shklovskii, B. I. *Phys. Rev. Lett.* **2010**, *104*, arXiv: 0910.3635, 128302, DOI: `10.1103/PhysRevLett.104.128302`.

(27) Bazant, M. Z.; Storey, B. D.; Kornyshev, A. A. *Phys. Rev. Lett.* **2011**, *106*, 046102, DOI: `10.1103/PhysRevLett.106.046102`.

(28) Lee, A. A.; Kondrat, S.; Vella, D.; Goriely, A. *Phys. Rev. Lett.* **2015**, *115*, 106101, DOI: `10.1103/PhysRevLett.115.106101`.

(29) Bohinc, K.; Shrestha, A.; Brumen, M.; May, S. *Phys. Rev. E* **2012**, *85*, 031130, DOI: `10.1103/PhysRevE.85.031130`.

(30) Caetano, D. L. Z.; Bossa, G. V.; de Oliveira, V. M., et al. *Phys. Chem. Chem. Phys.* **2016**, *18*, 27796–27807, DOI: `10.1039/C6CP04199J`.

(31) Bossa, G. V.; Caetano, D. L.; de Carvalho, S. J.; May, S. *Electrochim. Acta* **2019**, *321*, 134655, DOI: `10.1016/j.electacta.2019.134655`.

(32) Limmer, D. T. *Phys. Rev. Lett.* **2015**, *115*, 256102, DOI: `10.1103/PhysRevLett.115.256102`.

(33) Bossa, G. V.; May, S. *Phys. Rev. Res.* **2020**, *2*, 032040, DOI: `10.1103/PhysRevResearch.2.032040`.

(34) Brazovskiǐ, S. A. In *World Scientific Series in 20th Century Physics*; WORLD SCIENTIFIC: 1996; Vol. 11, pp 109–113, DOI: `10.1142/9789814317344_0016`.

(35) Hockney, R. W.; Eastwood, J. W., *Computer simulation using particles*, Special student ed; A. Hilger: Bristol [England] ; Philadelphia, 1988.

(36) Plimpton, S.; Pollock, R.; Stevens, M. In *Proceedings of Eighth SIAM Conference on Parallel Processing for Scientific Computing*, 1997.

(37) Frisch, H. L. *Science* **1965**, *150*, 1249–1254, DOI: `10.1126/science.150.3701.1249`.

(38) Jamei, R.; Kivelson, S.; Spivak, B. *Phys. Rev. Lett.* **2005**, *94*, 056805, DOI: `10.1103/PhysRevLett.94.056805`.

(39) Mahmoudian, S.; Rademaker, L.; Ralko, A.; Fratini, S.; Dobrosavljević, V. *Phys. Rev. Lett.* **2015**, *115*, 025701, DOI: `10.1103/PhysRevLett.115.025701`.

(40) Ludwig, N. B.; Dasbiswas, K.; Talapin, D. V.; Vaikuntanathan, S. *J. Chem. Phys.* **2018**, *149*, 164505, DOI: `10.1063/1.5043410`.

(41) Bozym, D. J.; Uralcan, B.; Limmer, D. T., et al. *J. Phys. Chem. Lett.* **2015**, *6*, 2644–2648, DOI: `10.1021/acs.jpclett.5b00899`.

(42) Downing, R.; Bossa, G. V.; May, S. *J. Phys. Chem. C* **2018**, *122*, 28537–28544, DOI: `10.1021/acs.jpcc.8b09756`.

(43) Wakai, C.; Oleinikova, A.; Ott, M.; Weingärtner, H. *J. Phys. Chem. B* **2005**, *109*, 17028–17030, DOI: `https://doi.org/10.1021/jp053946+`.

(44) Hautman, J.; Halley, J. W.; Rhee, Y.-J. *J. Chem. Phys.* **1989**, *91*, 467–472, DOI: `10.1063/1.457481`.

(45) Qing, L.; Zhao, S.; Wang, Z.-G. *J. Phys. Chem. B* **2021**, *125*, 625–636, DOI: `10.1021/acs.jpcb.0c09332`.

(46) Johnson, J. B. *Nature* **1927**, *119*, 50–51, DOI: `10.1038/119050c0`.

(47) Nyquist, H. *Phys. Rev.* **1928**, *32*, 110–113, DOI: `10.1103/PhysRev.32.110`.

(48) Merlet, C.; Péan, C.; Rotenberg, B., et al. *J. Phys. Chem. Lett.* **2013**, *4*, 264–268, DOI: `10.1021/jz3019226`.

(49) Merlet, C.; Limmer, D. T.; Salanne, M., et al. *J. Phys. Chem. C* **2014**, *118*, 18291–18298, DOI: `10.1021/jp503224w`.

(50) Noh, C.; Jung, Y. *Phys. Chem. Chem. Phys.* **2019**, *21*, 6790–6800, DOI: `10.1039/C8CP07200K`.

(51) Atkin, R.; El Abedin, S. Z.; Hayes, R., et al. *J. Phys. Chem. C* **2009**, *113*, 13266–13272, DOI: `10.1021/jp9026755`.

(52) Dwelle, K. A.; Willard, A. P. *J. Phys. Chem. C* **2019**, *123*, 24095–24103, DOI: `10.1021/acs.jpcc.9b06635`.

(53) Cruz, C.; Lomba, E.; Ciach, A. *J. Mol. Liq.* **2021**, 117078, DOI: `10.1016/j.molliq.2021.117078`.

(54) Bagchi, D.; Nguyen, T. D.; Olvera de la Cruz, M. *Proc. Natl. Acad. Sci. U.S.A.* **2020**, *117*, 19677–19684, DOI: `10.1073/pnas.2007545117`.

(55) Son, C. Y.; Wang, Z.-G. *Proc. Natl. Acad. Sci. U.S.A.* **2021**, *118*, e2020615118, DOI: `10.1073/pnas.2020615118`.

(56) Drüschler, M.; Huber, B.; Passerini, S.; Roling, B. *J. Phys. Chem. C* **2010**, *114*, 3614–3617, DOI: `10.1021/jp911513k`.

(57) Zhou, W.; Inoue, S.; Iwahashi, T., et al. *Electrochem. Commun.* **2010**, *12*, 672–675, DOI: `10.1016/j.elecom.2010.03.003`.

(58) Yeh, I.-C.; Berkowitz, M. L. *J. Chem. Phys.* **1999**, *111*, 3155–3162, DOI: `10.1063/1.479595`.

(59) Frydel, D. *J. Chem. Phys.* **2011**, *134*, 234704, DOI: `10.1063/1.3598476`.

(60) Gongadze, E.; Iglič, A. *Bioelectrochemistry* **2012**, *87*, 199–203, DOI: `10.1016/j.bioelechem.2011.12.001`.

(61) McDaniel, J. G.; Yethiraj, A. *J. Phys. Chem. Lett.* **2018**, *9*, 4765–4770, DOI: `10.1021/acs.jpclett.8b02120`.

(62) McDaniel, J. G.; Yethiraj, A. *J. Phys. Chem. B* **2019**, *123*, 3499–3512, DOI: `10.1021/acs.jpcb.9b00963`.

(63) Lian, Z.; Chao, H.; Wang, Z.-G. *ACS Nano* **2021**, *15*, 11724–11733, DOI: `10.1021/acsnano.1c02506`.

(64) Largeot, C.; Portet, C.; Chmiola, J., et al. *J. Am. Chem. Soc.* **2008**, *130*, 2730–2731, DOI: `10.1021/ja7106178`.

(65) Canongia Lopes, J. N.; Pádua, A. A. H. *Theor. Chem. Acc.* **2012**, *131*, 1129, DOI: `10.1007/s00214-012-1129-7`.

(66) Goloviznina, K.; Canongia Lopes, J. N.; Costa Gomes, M.; Pádua, A. A. H. *J. Chem. Theory Comput.* **2019**, *15*, 5858–5871, DOI: `10.1021/acs.jctc.9b00689`.

(67) Jitvisate, M.; Seddon, J. R. T. *J. Phys. Chem. Lett.* **2018**, *9*, 126–131, DOI: `10.1021/acs.jpclett.7b02946`.

Chapter 4

GAUSSIAN CORE MODEL WITH SMEARED ELECTROSTATICS

Lately, molecular dynamics (MD) simulations have emerged as an essential tool for understanding the structure, dynamics, and phase behavior of charged soft matter systems. To explore phenomena across greater length and time scales in MD simulations, molecules are often coarse-grained for better computational performance. However, commonly used force fields—like the one used in the previous chapter—represent particles as hard-core interaction centers with point charges, which often overemphasizes the packing effect and short-range electrostatics, especially in systems with bulky deformable organic molecules and systems with strong coarse-graining. This underscores the need for an efficient soft-core model to physically capture the effective interactions between coarse-grained particles. In this chapter, we implement a soft-core model uniting the Gaussian core model with smeared electrostatic interactions that is phenomenologically equivalent to recent theoretical models. We first parametrize it generically using water as the model solvent. Then, we benchmark its performance in the OpenMM toolkit for different boundary conditions to highlight a computational speedup of up to $34\times$ compared to commonly used force fields and existing implementations.

This chapter includes content from our previously published article:

Ye, B. B.; Chen, S.; Wang, Z.-G. *J. Chem. Theory Comput.* **2024**, acs.jctc.4c00603, DOI: 10.1021/acs.jctc.4c00603

4.1 Introduction

In recent years, computer simulations have become an essential tool for gaining physical insights into intriguing phenomena in polymeric and soft matter systems. Notably, MD simulations with atomistic force fields, which can accurately reproduce the structural, thermodynamic, and dynamic properties of materials [2, 3], have been used to understand molecular details and observe dynamic processes in those systems. However, even with the rapid advancement of computing power over the past few decades, atomistic MD simulations are often unable to capture phenomena that require considerable system sizes or extensive equilibrium periods due to the

high computational costs of evaluating the interactions among the numerous atoms in large systems.

This limitation has motivated the development of several coarse-grained simulation methods that improve computational performance by simplifying the representation of atomistic systems. A widely used approach is coarse-grained MD simulation, in which groups of atoms or molecules are mapped onto simple, featureless beads to decrease the number of degrees of freedom [4, 5]. By carefully determining force field parameters using bottom-up (structure-based) and/or top-down (thermodynamics-based) approaches, coarse-grained MD models can faithfully replicate key experimental data despite the loss of detail from the coarse-graining [6]. Another coarse-graining strategy is to convert the particle-based representation into a field-based representation through identify transformations. Field-theoretic simulations (FTSs) are particularly well-suited for efficient exploration of mesoscopic-length-scale phenomena in high-density systems and polymeric liquids with high molecular weights [7–13]. However, FTS does not provide dynamic information and the field variables do not directly inform the molecular-level structure.

Within the common coarse-grained MD models [14–17], such as the Kremer–Grest model for polymeric systems [18], the nonbonded interactions are generally treated using a combination of 12-6 Lennard-Jones (LJ) and point-charge Coulomb potentials. While these potentials are ubiquitous in MD simulations, they can be unsuitable for modeling organic molecules that can deform and interpenetrate, or systems that have undergone strong coarse-graining. The LJ potential is inherently a hard-core model because it has a divergence in potential energy when the particle centers come into contact. This places a tight upper bound on the simulation timestep, and can lead to a caging effect that severely hinders the diffusion of particles or even unphysical bulk liquid–solid phase transitions at high geometric packing [19]. Similarly, the Coulomb potential cannot capture the charge delocalization in bulky organic ions because it assigns the entirety of a particle's charge to its interaction center. As such, softer interactions are better suited to reflect the less pronounced packing effects and short-range electrostatics in coarse-grained soft matter systems.

Dissipative particle dynamics (DPD) [20, 21], a mesoscale simulation method commonly used to model fluidic systems, addresses the shortcomings of hard-core models by treating excluded volume interactions using a soft-core potential [22]. To model charged particles, the charges are smeared onto an arbitrarily-sized grid to prevent unbreakable ion pairs [23]. While the DPD potential is well-suited for mod-

eling the soft interactions between coarse-grained bulky molecules or even entire liquid elements, its quadratic form is not readily amenable to theoretical analysis. Perhaps more importantly, there is no analytically closed form for the electrostatic potential, so it is usually evaluated on CPU without Ewald summation in the MD software that supports DPD. This makes the evaluation of the electrostatic interactions much slower than the GPU-accelerated implementations commonly used in LJ-based charged systems.

Therefore, there is a need for a more physical and efficient GPU-enabled coarse-grained MD model that can simulate large-scale soft matter systems over long time frames. To this end, we implement a coarse-grained MD model that is motivated by and compatible with previous Gaussian soft-core models, such as the Gaussian overlap model by Berne and Pechukas [24] and the Gaussian core model (GCM) by Stillinger [25–27]. These types of models have been used recently to study the liquid–liquid phase separation and dynamics in polymer solutions and melts [11, 12, 28–31]. In particular, Jedlinska et al. [32] and Lequieu [13] have employed Gaussian-distributed particle densities in their multirepresentation simulation approaches to convert between particle- and field-based representations. Our model, henceforth referred to as GCMe, combines the GCM with smeared electrostatic interactions from Gaussian charge distributions [33–35]. This combination maintains the soft nature of DPD and its advantages, can model the charge smearing in large ions, and still has simple analytically tractable expressions for the interaction potentials. In this chapter, we establish the thermodynamic basis of GCMe and highlight the computational speedup that is possible with our GCMe implementation in the high-performance OpenMM toolkit for different types of system boundaries.

4.2 Model and methods

In GCMe, featureless spherical particles with smeared charges interact via centrosymmetric pair potentials. A charged particle i has Gaussian-distributed mass density

$$\rho_{i,m}(\mathbf{r}) = \left(\frac{3}{2\pi\sigma_i^2}\right)^{3/2} \exp\left(-\frac{3}{2\sigma_i^2}(\mathbf{r} - \mathbf{r}_i)^2\right) \tag{4.1}$$

and charge density

$$\rho_{i,q}(\mathbf{r}) = \frac{z_i e}{(2a_i^2)^{3/2}} \exp\left(-\frac{\pi}{2a_i^2}(\mathbf{r} - \mathbf{r}_i)^2\right), \tag{4.2}$$

where σ_i and a_i are the mass and electrostatic smearing radii, respectively, z_i is the charge number, and e is the elementary charge. These Gaussian distributions have recently been used in theoretical models [11, 12, 28–31, 36, 37] because they have conveniently defined Fourier transforms and approach the Dirac delta function, the limit of a point charge, as the smearing radii approach zero, and the particular form of the charge density distribution in Eq. 4.2 reproduces the Born energy for the self-energy of an ion i [37].

The pair interaction potentials for Eqs. 4.1 and 4.2 are analytically solvable integrals, and the derivations can be found in the Supporting Information (SI). The excluded volume interaction between two particles i and j is given by

$$u_{\text{ex}}(r_{ij}) = A_{ij} \left(\frac{3}{2\pi\sigma_{ij}^2} \right)^{3/2} \exp\left(-\frac{3}{2\sigma_{ij}^2} r_{ij}^2 \right), \tag{4.3}$$

where $\sigma_{ij} = \sqrt{\sigma_i^2 + \sigma_j^2}$, r_{ij} is the separation distance, and A_{ij} specifies the strength of the excluded volume interactions. Since Eq. 4.3 has the form of a Gaussian interaction potential, the local excluded volume interaction between two smeared mass densities is equivalent to a Gaussian interaction between two point particles.

The smeared electrostatic interaction has the form

$$u_{\text{elec}}(r_{ij}) = \frac{z_i z_j e^2}{4\pi\varepsilon_0\varepsilon_r r_{ij}} \operatorname{erf}\left(\frac{\pi^{1/2}}{2^{1/2}a_{ij}} r_{ij} \right), \tag{4.4}$$

where $a_{ij} = \sqrt{a_i^2 + a_j^2}$, ε_0 is the vacuum permittivity, and ε_r is the relative permittivity. Unlike the point-charge Coulomb potential, the smeared electrostatic potential remains finite even as the separation distance tends to zero. Importantly, the self-energy of an ion i ($r_{ii} \to 0$) can now be defined and is simply the Born energy $z_i^2 e^2/(8\pi\varepsilon_0\varepsilon_r a)$. For two particles that come into contact ($r_{ij} \to 0$), the smeared electrostatic potential reaches an asymptotic value of $z_i z_j e^2/(2^{3/2}\pi\varepsilon_0\varepsilon_r a_{ij})$. To prevent ions from collapsing on top of each other, the excluded volume repulsion must overcome the electrostatic attraction between two oppositely charged particles, so the relationship

$$\frac{A_{ij}}{\sigma_{ij}^3 k_{\text{B}}T} \gg \frac{4\pi^{3/2} z_i z_j \lambda_{\text{B}}}{3^{3/2} a_{ij}}, \tag{4.5}$$

where $\lambda_{\text{B}} = e^2/(4\pi\varepsilon_0\varepsilon_r k_{\text{B}}T)$ is the Bjerrum length, must hold.

Another advantage of the smeared electrostatic potential is that it can still be efficiently evaluated in reciprocal space using three-dimensional Ewald summation

[38]. The particle-mesh Ewald method for the smeared electrostatic potential splits the total coulombic energy into four parts as follows:

$$
\begin{aligned}
U_{\text{elec}} &= \frac{e^2}{8\pi\varepsilon_0\varepsilon_{\text{r}}} \sum_{\mathbf{n}} \sum_{i,j}^{N} \frac{z_i z_j}{r_{ij,\mathbf{n}}} \operatorname{erf}\left(\frac{\pi^{1/2}}{2^{1/2}a_{ij}} r_{ij,\mathbf{n}}\right) \\
&= U_{\text{elec, real}} + U_{\text{elec, recip}} + U_{\text{elec, corr}} + U_{\text{elec, self}} \\
&= \frac{e^2}{8\pi\varepsilon_0\varepsilon_{\text{r}}} \sum_{\mathbf{n}}' \sum_{i,j}^{N} \frac{z_i z_j}{r_{ij,\mathbf{n}}} \left[\operatorname{erf}\left(\frac{\pi^{1/2}}{2^{1/2}a_{ij}} r_{ij,\mathbf{n}}\right) - \operatorname{erf}\left(\frac{r_{ij,\mathbf{n}}}{2^{1/2}G}\right)\right] \\
&\quad + \frac{1}{2\varepsilon_0\varepsilon_{\text{r}}V} \sum_{\mathbf{k}\neq\mathbf{0}} \frac{\exp\left(-G^2 k^2/2\right)}{k^2} |S(\mathbf{k})|^2 \\
&\quad - \frac{e^2}{4\pi(2\pi)^{1/2}\varepsilon_0\varepsilon_{\text{r}}G} \sum_{i}^{N} z_i^2 \\
&\quad + \frac{e^2}{8\pi\varepsilon_0\varepsilon_{\text{r}}} \sum_{i}^{N} \frac{z_i^2}{a_i},
\end{aligned}
\tag{4.6}
$$

where $\mathbf{n}$ is the cell-coordinate vector specifying the position of a periodic cell, the prime (′) in the sum in the $U_{\text{elec, real}}$ term indicates that terms where $i = j$ are omitted for $\mathbf{n} = \mathbf{0}$, G is the width of the Gaussian charge distributions introduced to screen the smeared charges, $\mathbf{k}$ and $k = |\mathbf{k}|$ are the reciprocal lattice vector and its magnitude, respectively, and $S(\mathbf{k}) = e\sum_{j}^{N} z_j \exp\left(i\mathbf{k}\cdot\mathbf{r}_j\right)$ [34, 35, 39, 40]. The screening charge distributions are not strictly necessary, as the evaluation of the position-dependent terms in Eq. 4.6 can be carried out entirely in reciprocal space by choosing $G = a_{ij}/\pi^{1/2}$, but they are generally included to improve computational efficiency by moving part of the calculation effort to the real space [35, 40].

In Eq. 4.6, the $U_{\text{elec, recip}}$ and $U_{\text{elec, corr}}$ terms are equivalent to those found in the standard Ewald summation for the point-charge Coulomb potential [41–43]. The $U_{\text{Coul, recip}}$ term captures the coulombic energy of point charges (carrying the same charges as the smeared charges) interacting with equal but opposite charge distributions compensating for the screening charge distributions in reciprocal space after the cutoff, and the $U_{\text{Coul, corr}}$ term is a constant term that corrects for the self-interactions between the point charges and the compensating charge distributions spuriously included in $U_{\text{Coul, recip}}$.

The only differences between the Ewald summations for smeared charges and point charges are manifested in the $U_{\text{elec, real}}$ term and an additional constant $U_{\text{elec, self}}$ term that accounts for the self-energies of the ions [39]. The $U_{\text{elec, real}}$ term evaluates

short-range electrostatic interactions within a designated cutoff in real space. Inside the brackets, the first term corresponds to the interaction between two smeared charges i and j (instead of two point charges), while the second term accounts for the interaction between a point charge and the screening charge distribution for charge j that cancels out the compensating interaction in $U_{\text{Coul, recip}}$.

As such, existing mesh-based schemes for evaluating the standard Ewald summation can be used in Eq. 4.6 by simply modifying the real-space contribution and including the self-energies. Schematics depicting and comparing the real-space, reciprocal-space, correction, and self-energy contributions to the Ewald summations for point charges and GCMe smeared charges can be found in Figs. 4.2 and 4.3 in the Appendix.

4.3 Parametrization

An important criterion for coarse-grained models is that the thermodynamics of the fluid, which is described by the fluctuations in the system, should be reproduced faithfully. After selecting appropriate σ_i and a_i values for a system of interest, there is only one undefined GCMe parameter, the repulsion parameter A_{ij}. In principle, A_{ij} can be determined precisely via systematic structure- or thermodynamics-based coarse-graining procedures [6]. However, in this chapter, we aim to simply model generic soft matter systems in a manner consistent with how equivalent DPD simulations would be configured. Following the formulation of the DPD method [22, 23, 44], we also parametrize GCMe by associating the value of A_{ij} with the compressibility of water, a commonly-used solvent in soft matter systems. Like other coarse-grained models, this generically parametrized GCMe will likely underrepresent the system's configurational entropy due to the smoothing out of atomistic details [45]. This loss of entropy can be mitigated by a number of different approaches [46, 47] but is not the focus of the current work.

To connect A_{ij} to the compressibility, we start with an expression relating pressure p to the simulation number density ρ. Using the virial theorem and the additivity of the pairwise forces, the pressure can be determined using

$$
\begin{aligned}
p &= \rho k_{\text{B}} T + \frac{1}{3V} \left\langle \sum_{i<j} (\mathbf{r}_i - \mathbf{r}_j) \cdot \mathbf{f}_i \right\rangle \\
&= \rho k_{\text{B}} T + \frac{2\pi}{3} \rho^2 \int_0^\infty r^3 f_{ij}(r) g_{ij}(r) \, dr,
\end{aligned}
\tag{4.7}
$$

where $k_{\text{B}} T$ is the thermal energy scale, V is the system volume, $\mathbf{f}_i$ and $\mathbf{r}_i$ are the force

acting on and the position of particle i, respectively, and f_{ij} and g_{ij} are the pairwise GCMe force and radial distribution function between particles i and j. For soft sphere models, the main contributions to the pressure come from the leading-order ρ terms [22], so an approximation for the equation of state that holds at sufficiently high number densities is

$$p \approx \rho k_{\mathrm{B}} T + \omega A_{ij} \rho^2, \tag{4.8}$$

where ω is a dimensionless scaling constant. With Eq. 4.8, the dimensionless compressibility κ^{-1} is related to A_{ij} via

$$
\begin{aligned}
\kappa^{-1} &= \frac{1}{n k_{\mathrm{B}} T \kappa_T} = \frac{1}{k_{\mathrm{B}} T} \left(\frac{\partial p}{\partial \rho} \right)_T \left(\frac{\partial \rho}{\partial n} \right)_T \\
&= \frac{1}{N_{\mathrm{m}}} \left(1 + \frac{2 \omega A_{ij} \rho}{k_{\mathrm{B}} T} \right),
\end{aligned}
\tag{4.9}
$$

where n is the number density of water molecules, κ_T is the isothermal compressibility, and $N_{\mathrm{m}} \equiv (\partial n / \partial \rho)_T$ is a real-space renormalization factor, or the number of water molecules represented by each simulation particle.

To determine ω and obtain the equation of state, we conducted a series of MD simulations in the isothermal–isobaric (NpT) ensemble at room temperature $T = 300$ K and varying p and A_{ij} values. The cubic systems were initialized with $N = 10,000$ randomly placed particles with size $d = 2\sigma = 0.275$ nm and mass $m = 18.02$ g/mol. For each simulation, energy minimization and system equilibration were performed over 1×10^7 timesteps of step size $t = 0.01\tau$, where $\tau = \sqrt{md^2/(N_A k_{\mathrm{B}} T)} \approx 0.739$ ps is the intrinsic time scale and N_A is the Avogadro constant, and data were collected over an additional 4×10^7 timesteps, which are on the order of 300 ns.

By plotting the excess pressure (or the nonideal contributions) normalized by A_{ij}, Fig. 4.1a shows that all systems fall on a master curve, indicating a simple scaling relation. When the excess pressure is normalized by ρ^2, it levels off to an asymptotic value of $\omega = 0.499$ at large ρ in Fig. 4.1b, confirming that the main contribution to the excess pressure is from the ρ^2 term and that Eq. 4.8 is valid. With $\omega = 0.499$ and a dimensionless compressibility of $\kappa^{-1} = 15.9835$ for water, Eq. 4.9 provides the key GCMe parametrization relationship

$$A_{ij} = \frac{(15.9835 N_{\mathrm{m}} - 1) k_{\mathrm{B}} T}{0.998 \rho}, \tag{4.10}$$

with ρ and N_{m} being free parameters.

From a computational perspective, it is favorable to choose the lowest ρ value that still satisfies the scaling relation since the number of pair interactions scales
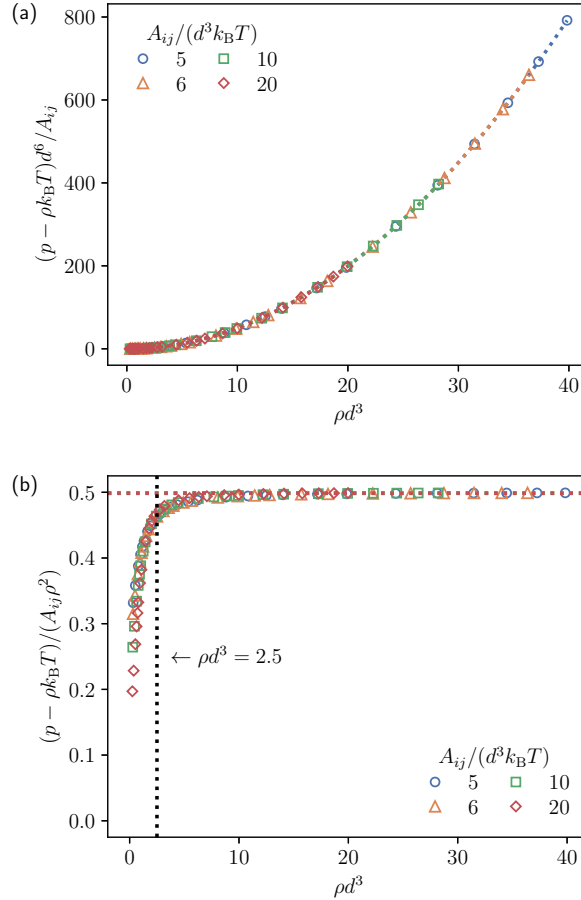
Figure 4.1: (a) A_{ij}- and (b) $A_{ij}\rho^2$-normalized excess pressure $p - \rho k_{\mathrm{B}} T$ as functions of the number density ρ and repulsion parameter A_{ij} for the Gaussian core model. The dotted lines in (a) show the best quadratic fits. The horizontal dotted lines in (b) specify the asymptotic ω values, while the vertical dotted line indicates the optimal number density ρ.

linearly with ρ and the complexity of a single step of a MD simulation increases with the square of ρ. Fig. 4.1b indicates that $\rho = 2.5 d^{-3}$, which is indicated by the black vertical dotted line, is a reasonable choice. Similarly, for the coarse-graining level N_{m}, we recommend the commonly used four-to-one mapping scheme where each simulation particle roughly encompasses the volume of a $(\mathrm{CH}_2)_3$ group in a straight-chain alkane [23, 44, 48]. This real-space renormalization not only affects A_{ij} via Eq. 4.10 and the length, mass, and time scales, which are now $d = (\rho d^3 N_{\mathrm{m}})^{1/3} \times (0.275 \text{ nm}) \approx 0.592$ nm, $m = N_{\mathrm{m}} \times (18.02 \text{ g/mol}) \approx 72.1$ g/mol, and $\tau \approx 3.18$ ps, respectively, but also speeds up the simulation for a given system volume because there are now fewer particle positions to update.

Finally, to extend GCMe from melts to polymeric mixtures and solutions, the particles can be connected to form polymers, with the connectivity handled using a commonly-used bond potential such as the harmonic and finite extensible nonlinear elastic (FENE) [18] bond potentials. The correct scaling of $R_{\mathrm{g}} \sim N^{3/5}$ is attained for a single GCMe polymer in an athermal solvent, as shown in Fig. 4.5 in the Appendix. To study liquid–liquid interfaces, a connection between GCMe and the Flory–Huggins theory [49, 50] can be made to reinterpret A_{ij} in terms of an energetic χ-parameter. This mapping is available in the Appendix.

4.4 Performance

We have implemented GCMe in OpenMM [51], a high-performance MD simulation toolkit, to take advantage of its class-leading GPU acceleration among the popular MD packages [52, 53] and leverage its extensibility and modularity to implement Eqs. 4.3 and 4.4 as custom pair potentials (available in our open-source MDCraft Python package).

To highlight the performance (or simulation throughput, defined as simulation time per elapsed real time) of our GCMe implementation, we benchmarked systems using the Weeks–Chandler–Andersen (WCA) and Coulomb potentials and GCMe with various boundary conditions and integration step sizes in both OpenMM 7.7.0 and LAMMPS (21 Nov 2023). LAMMPS [54] currently contains the only other GCMe implementation through a combination of `pair_style gauss` in the base package and `pair_style buck6d/coul/gauss/long` in the MOF-FF package [55]. For the method of image charges, we employed the GPU-only `openmm_constV` OpenMM plugin [56] and the CPU-only LAMMPS `fix imagecharges` command [57]. All benchmarks were performed using a desktop computer with an Intel Core i9-10900K CPU and an NVIDIA RTX 3080 (10 GB) GPU running Ubuntu 20.04 LTS through the Windows Subsystem for Linux. The results are tabulated in Table 4.1.

For identical GCMe systems with different boundary conditions, our testing shows that our GPU-accelerated implementation in OpenMM is on average over an order of magnitude faster than the existing multithreaded LAMMPS implementation, with the largest speedup of 23× observed in the slab system with image charges. When compared to systems utilizing the LJ-based Weeks–Chandler–Andersen (WCA) and point-charge Coulomb potentials, our GCMe implementation in OpenMM provides an 8× performance uplift over the fastest OpenMP-accelerated LAMMPS method we

Table 4.1: Comparison of simulation timesteps (ts) per second across systems with $N = 1,000$ particles and varying reduced number densities ρ^*, models, boundary conditions, reduced step sizes t^*, and simulation toolkits.

ρ^*	Model	System	t^*	Toolkit	ts/s
0.8	WCA/Coulomb	Slab w/ IC[a]	0.005	LAMMPS (OpenMP)[d]	429
				OpenMM (CUDA)[e]	3,257
2.5	GCMe	Bulk[b]	0.005	LAMMPS (OpenMP)[f]	342
				OpenMM (CUDA)[e]	4,299
			0.020	LAMMPS (OpenMP)[f]	320
				OpenMM (CUDA)[e]	4,250
		Slab[b,c]	0.005	LAMMPS (OpenMP)[f]	263
				OpenMM (CUDA)[e]	2,760
			0.020	LAMMPS (OpenMP)[f]	255
				OpenMM (CUDA)[e]	2,832
		Slab w/ IC[b,c]	0.005	LAMMPS (OpenMP)[f]	163
				OpenMM (CUDA)[e]	3,772
			0.020	LAMMPS (OpenMP)[f]	152
				OpenMM (CUDA)[e]	3,689

[a] The simulation system has dimensions of $8.0d \times 7.8d \times 20.0d$, where d is the particle diameter.

[b] The simulation system has dimensions of $5.5d \times 5.2d \times 14.0d$.

[c] Each surface contains 288 particles with size $d/2$ arranged in a hexagonal close-packed (HCP) lattice carrying charges such that the constant surface charge density is $\sigma_q = 0.005\,\mathrm{e/nm}^2$.

[d] The simulation was allocated two CPU threads (higher values led to simulation instability).

[e] The simulations were allocated a single GPU.

[f] The simulations were allocated eight CPU threads (higher values did not improve performance).

had access to in our previous study [58]. Furthermore, larger step sizes can be taken in GCMe while still properly maintaining temperature control, since the potential energy does not diverge when particles come into contact, unlike the WCA and point-charge Coulomb potentials. As such, we can achieve a further four-fold performance boost by using a step size of $t = 0.02\tau$ in GCMe, enabling an OpenMM simulation of a slab system with image charges that is up to 34× faster than a comparable system simulated with WCA and Coulomb potentials. Remarkably, this speedup does not even account for the multiple orders of magnitude faster dynamics from the removal of the caging effect [44], which further extends the physical time and length scales attainable with a soft-core model like GCMe.

4.5 Conclusion

In conclusion, we have developed and implemented GCMe, a soft-core model for MD simulations that combines the GCM and smeared electrostatic interactions and is directly compatible with the models used in recent theoretical studies [11, 12, 28–31, 37] to study charged soft matter systems. The key feature of GCMe lies in its soft interaction potentials, which have clear physical origins and can accurately capture the weaker packing effects and short-range electrostatics in deformable organic molecules and systems with strong coarse-graining. Moreover, the excluded volume and electrostatic potentials do not diverge when particles overlap, allowing larger simulation timesteps to be taken. This, when combined with the optimized GPU-accelerated framework in the high-performance OpenMM toolkit, gives our GCMe implementation class-leading efficiency among similar coarse-grained simulation methods. Our benchmarks show that GCMe in OpenMM is at least 8× faster than the only existing GCMe implementation currently available, and can be up to 34× faster than the coarse-grained methods we had access to in our recent study [58]. This significant performance improvement enables simulating systems with hundreds of thousands of charged particles (corresponding to millions of atoms) over time scales on the order of milliseconds in just a few hours on modern computer hardware.

As we are interested in modeling coarse-grained soft matter systems using GCMe, we have generically parametrized it by determining a relationship between the repulsion parameter A_{ij} and the dimensionless compressibility of water, a common solvent. In principle, GCMe can model more realistic systems by rigorously parametrizing them with important effects and properties accounted for, such as particle size asymmetry, solvent type and quality, and explicit ion polarizability. In our current implementation, our study was limited to systems with parallel planar surfaces with infinite permittivity or the same permittivity as the electrolyte due to the use of the efficient method of image charges to model boundary polarization effects. However, GCMe can readily be expanded to surfaces with arbitrary permittivities and complex geometries (e.g., curved, cylindrical [59], spherical [60], and undulating surfaces [61, 62]) by employing more sophisticated methods, such as the induced charge computation method [63, 64] and the constant potential method [65, 66], to capture the polarization effects. We expect GCMe to be able to integrate with these polarization methods since it already uses discrete smeared charges to represent surface particles.

With the system-specific parametrization and the innate efficiency of our model, we

expect GCMe to be able to predict and explore rich bulk and interfacial phenomena in a wide variety of large soft matter systems over long time scales. In particular, we envision GCMe being useful for investigating the thermodynamics and charge transport in highly concentrated electrolytes, where anomalous phenomena like underscreening [67, 68] have been reported.

4.6 Appendix

Derivation of the excluded volume interaction potential

For a particle i with mass m_i, its smeared density ρ_i over radius σ_i is

$$\rho_i(\mathbf{r}) = \left(\frac{3}{2\pi\sigma_i^2}\right)^{3/2} \exp\left[-\frac{3(\mathbf{r} - \mathbf{r}_i)^2}{2\sigma_i^2}\right].$$

The excluded volume interaction potential between two particles i and j is

$$u_{ex}(r_{ij}) = A_{ij} \int \rho_i(\mathbf{r})\rho_j(\mathbf{r})\, d\mathbf{r}$$

$$= A_{ij} \left(\frac{3}{2\pi\sigma_i\sigma_j}\right)^3 \int \exp\left[-\frac{3(\mathbf{r} - \mathbf{r}_i)^2}{2\sigma_i^2}\right] \exp\left[-\frac{3(\mathbf{r} - \mathbf{r}_j)^2}{2\sigma_j^2}\right] d\mathbf{r}.$$

Evaluating the Gaussian integral over three dimensions gives

$$u_{\mathrm{ex}}(r_{ij}) = A_{ij} \left(\frac{3}{2\pi\sigma_{ij}^2}\right)^{3/2} \exp\left[-\frac{3\left(\mathbf{r}_i - \mathbf{r}_j\right)^2}{2\sigma_{ij}^2}\right],$$

where $\sigma_{ij}^2 = \sigma_i^2 + \sigma_j^2$.

Derivation of the smeared electrostatic interaction potential

The Fourier and inverse Fourier transforms are

$$\hat{f}(\mathbf{k}) = \int f(\mathbf{r}) \exp\left(-i\mathbf{k} \cdot \mathbf{r}\right) d\mathbf{r} \quad \longleftrightarrow \quad f(\mathbf{r}) = \frac{1}{(2\pi)^3} \int \hat{f}(\mathbf{k}) \exp\left(i\mathbf{k} \cdot \mathbf{r}\right) d\mathbf{k}.$$

For an ion i with charge $q_i = z_i e$, its smeared charge density ρ_i over radius a_i is

$$\rho_i(\mathbf{r}) = \frac{z_i e}{(2a_i^2)^{3/2}} \exp\left[-\frac{\pi (\mathbf{r} - \mathbf{r}_i)^2}{2a_i^2}\right]. \tag{4.11}$$

The electrostatic interaction potential between two particles i and j is

$$u_{\mathrm{Coul}}(r_{ij}) = \int \rho_i(\mathbf{r})\, C(\mathbf{r} - \mathbf{r}')\, \rho_j(\mathbf{r}')\, d\mathbf{r}'\, d\mathbf{r}, \tag{4.12}$$

where $C(\mathbf{r} - \mathbf{r}') = (4\pi\varepsilon_0\varepsilon_{\mathrm{r}}|\mathbf{r} - \mathbf{r}'|)^{-1}$ is the Coulomb operator.

With $r = |\mathbf{r}|$ and the change of variable $\bar{\mathbf{r}} = \mathbf{r} - \mathbf{r}'$, the Fourier transform of $C\,(\mathbf{r} - \mathbf{r}')$ multiplied by a Yukawa-type function $\exp\left(-\lambda\,|\bar{\mathbf{r}}|\right)$ that tends to 1 as $\lambda \to 0$ is

$$
\begin{aligned}
\hat{C}(\mathbf{k}) &= \lim_{\lambda \to 0} \int \frac{1}{4\pi\varepsilon_0\varepsilon_{\mathrm{r}}\,|\bar{\mathbf{r}}|} \exp\left(-i\mathbf{k}\cdot\bar{\mathbf{r}}\right) \exp\left(-\lambda\,|\bar{\mathbf{r}}|\right) d\bar{\mathbf{r}} \\
&= \frac{1}{4\pi\varepsilon_0\varepsilon_{\mathrm{r}}} \lim_{\lambda \to 0} \int \frac{\exp\left(-ik\bar{r}\cos\theta - \lambda\bar{r}\right)}{\bar{r}}\,d\bar{\mathbf{r}}.
\end{aligned}
\tag{4.13}
$$

Integrating Eq. 4.13 in the spherical coordinate system using an u-substitution $u = \cos\theta$ and then by parts,

$$
\begin{aligned}
\hat{C}(\mathbf{k}) &= \frac{1}{4\pi\varepsilon_0\varepsilon_{\mathrm{r}}} \lim_{\lambda \to 0} \int_0^\infty \bar{r}^2 \int_0^\pi \sin\theta \int_0^{2\pi} \frac{\exp\left(-ik\bar{r}\cos\theta - \lambda\bar{r}\right)}{\bar{r}}\,d\varphi\,d\theta\,d\bar{r} \\
&= \frac{1}{\varepsilon_0\varepsilon_{\mathrm{r}}k} \lim_{\lambda \to 0} \int_0^\infty \sin\left(k\bar{r}\right) \exp\left(-\lambda\bar{r}\right) d\bar{r} \\
&= \frac{1}{\varepsilon_0\varepsilon_{\mathrm{r}}k} \lim_{\lambda \to 0} \frac{k}{\lambda^2 + k^2} = \frac{1}{\varepsilon_0\varepsilon_{\mathrm{r}}k^2}.
\end{aligned}
\tag{4.14}
$$

With the change of variable $\bar{\mathbf{r}} \equiv \mathbf{r} - \mathbf{r}_i$, the Fourier transform of Eq. 4.11 is

$$
\hat{\rho}_i(\mathbf{k}) = \frac{z_i e}{(2a_i^2)^{3/2}} \int \exp\left[-\left(\frac{\pi\bar{\mathbf{r}}\cdot\bar{\mathbf{r}}}{2a_i^2} + i\mathbf{k}\cdot\bar{\mathbf{r}}\right)\right] d\bar{\mathbf{r}} = z_i e \exp\left(-\frac{a_i^2 k^2}{2\pi}\right).
\tag{4.15}
$$

Substituting Eqs. 4.14 and 4.15 into Eq. 4.12 and taking the inverse Fourier transform by integrating over all $\mathbf{r}$ and $\mathbf{r}'$ and using the definition of a delta function $\delta(\mathbf{r}) = (2\pi)^{-3} \int \exp\left(i\mathbf{k}\cdot\mathbf{r}\right) d\mathbf{k}$,

$$
\begin{aligned}
u_{\mathrm{elec}}(r_{ij}) &= \frac{z_i z_j e^2}{(2\pi)^9 \varepsilon_0\varepsilon_{\mathrm{r}}} \int \frac{\mathrm{e}^{-(a_i^2 k_1^2 + a_j^2 k_3^2)/(2\pi)}\,\mathrm{e}^{i\mathbf{k}_1\cdot(\mathbf{r}-\mathbf{r}_i) + i\mathbf{k}_2\cdot(\mathbf{r}-\mathbf{r}') + i\mathbf{k}_3\cdot\left(\mathbf{r}'-\mathbf{r}_j\right)}}{k_2^2} d\mathbf{r}'\,d\mathbf{r}\,d\mathbf{k}_1\,d\mathbf{k}_2\,d\mathbf{k}_3 \\
&= \frac{z_i z_j e^2}{(2\pi)^3 \varepsilon_0\varepsilon_{\mathrm{r}}} \int \frac{\exp\left[ikr_{ij}\cos\theta - a_{ij}^2 k^2/(2\pi)\right]}{k^2} d\mathbf{k},
\end{aligned}
\tag{4.16}
$$

where $a_{ij}^2 = a_i^2 + a_j^2$ and $r_{ij} = \left|\mathbf{r}_i - \mathbf{r}_j\right|$.

Integrating Eq. 4.16 in the spherical coordinate system using an u-substitution $u = \cos\theta$, the definition $2\sin\left(kr_{ij}\right)/k = \int_{-r_{ij}}^{r_{ij}} \exp\left(iks\right) ds$, and a change of variables

$$s = (2^{1/2}a_{ij}/\pi^{1/2})t,$$

$$u_{\text{elec}}(r_{ij}) = \frac{z_i z_j e^2}{(2\pi)^3 \varepsilon_0 \varepsilon_r} \int_0^\infty k^2 \int_0^\pi \sin\theta \int_0^{2\pi} \frac{\exp\left[ikr_{ij}\cos\theta - a_{ij}^2 k^2/(2\pi)\right]}{k^2} \, d\varphi \, d\theta \, dk$$

$$= \frac{z_i z_j e^2}{(2\pi)^2 \varepsilon_0 \varepsilon_r r_{ij}} \int_0^\infty \frac{2\sin(kr_{ij})}{k} \exp\left(-\frac{a_{ij}^2 k^2}{2\pi}\right) dk$$

$$= \frac{z_i z_j e^2}{2^{3/2}\pi \varepsilon_0 \varepsilon_r a_{ij} r_{ij}} \int_0^{r_{ij}} \exp\left(-\frac{\pi}{2a_{ij}^2}s^2\right) ds$$

$$= \frac{z_i z_j e^2}{4\pi \varepsilon_0 \varepsilon_r r_{ij}} \operatorname{erf}\left(\frac{\pi^{1/2}}{2^{1/2}a_{ij}}r_{ij}\right).$$

Limits of the GCMe interaction potentials

When the separation distance between particles become very large ($r_{ij} \to \infty$) or when the electrostatic smearing radius approaches zero ($a_{ij} \to 0$), the smeared electrostatic potential converges to the Coulomb potential as expected:

$$\lim_{r_{ij}\to\infty} u_{\text{elec}}(r_{ij}) = \frac{z_i z_j e^2}{4\pi \varepsilon_0 \varepsilon_r r_{ij}} \lim_{r_{ij}\to\infty}\left[\operatorname{erf}\left(\frac{\pi^{1/2}}{,}2^{1/2}a_{ij}r_{ij}\right)\right] = \frac{z_i z_j e^2}{4\pi \varepsilon_0 \varepsilon_r r_{ij}},$$

$$\lim_{a_{ij}\to0} u_{\text{elec}}(r_{ij}) = \frac{z_i z_j e^2}{4\pi \varepsilon_0 \varepsilon_r r_{ij}} \lim_{a_{ij}\to0}\left[\operatorname{erf}\left(\frac{\pi^{1/2}}{2^{1/2}a_{ij}}r_{ij}\right)\right] = \frac{z_i z_j e^2}{4\pi \varepsilon_0 \varepsilon_r r_{ij}}.$$

When the separation distance between particles become very small ($r_{ij} \to 0$), the excluded volume and smeared electrostatic potentials have the values

$$\lim_{r_{ij}\to0} u_{\text{ex}}(r_{ij}) = A_{ij}\left(\frac{3}{2\pi\sigma_{ij}^2}\right)^{3/2} \lim_{r_{ij}\to0}\left[\exp\left(-\frac{3}{2\sigma_{ij}^2}r_{ij}^2\right)\right] = A_{ij}\left(\frac{3}{2\pi\sigma_{ij}^2}\right)^{3/2}$$

and

$$\operatorname{erf}\left(\frac{\pi^{1/2}}{2^{1/2}a_{ij}}r_{ij}\right) = \frac{2^{1/2}}{a_{ij}}r_{ij} + O(r_{ij}^3) \longrightarrow \lim_{r_{ij}\to0} u_{\text{elec}}(r_{ij}) = \frac{z_i z_j e^2}{2^{3/2}\pi \varepsilon_0 \varepsilon_r a_{ij}}.$$

If ions i and j have the same Born radii $a = a_i = a_j$, the smeared electrostatic potential as $r_{ij} \to 0$ becomes

$$\lim_{r_{ij}\to0} u_{\text{elec}}(r_{ij}) \approx \frac{z_i z_j e^2}{4\pi \varepsilon_0 \varepsilon_r a}.$$

The self-energy of an ion i is

$$u_{\text{elec, self}} = \frac{1}{2} \lim_{r_{ii}\to0} u_{\text{elec}}(r_{ii}) \approx \frac{z_i^2 e^2}{8\pi \varepsilon_0 \varepsilon_r a_i}, \tag{4.17}$$

which is simply the Born energy [37].

Ewald summation
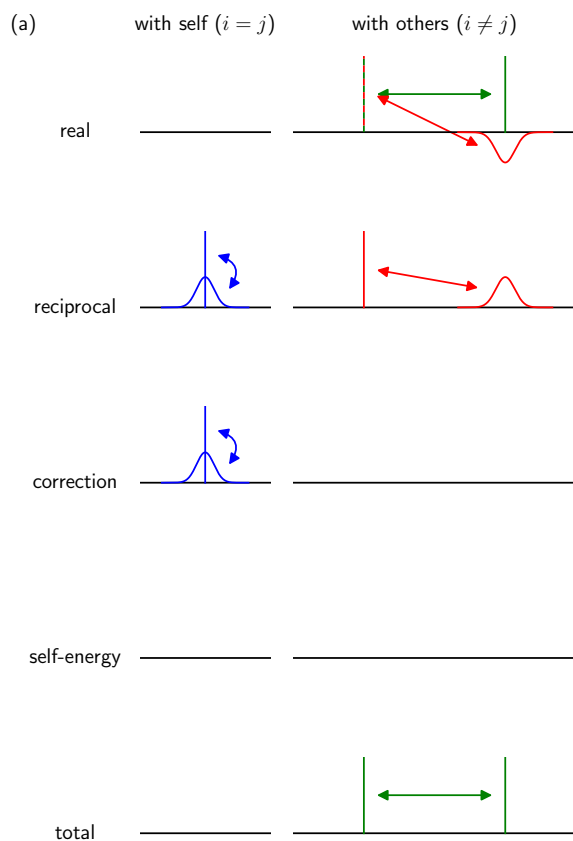
Figure 4.2: Schematic representations of the real-space, reciprocal-space, and self-energy contributions to the Ewald summations for point charges. The vertical lines and wide distributions represent point charges and screening/compensating charge distributions, respectively, each with charge magnitude $|q_i| = e$.
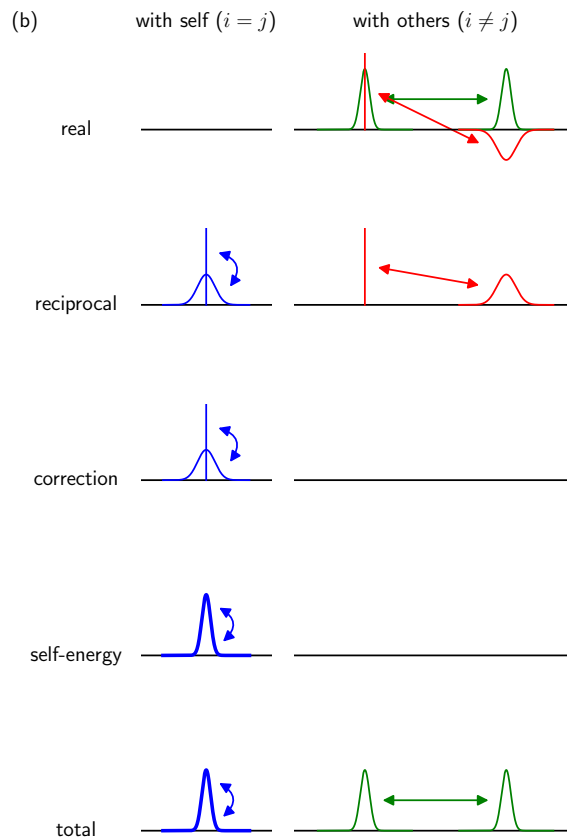
Figure 4.3: Schematic representations of the real-space, reciprocal-space, correction, and self-energy contributions to the Ewald summations for GCMe smeared charges. The vertical lines, narrow distributions, and wide distributions represent point charges, GCMe smeared charges, and screening/compensating charge distributions, respectively, each with charge magnitude $|q_i| = e$. Note that the correction term is subtracted in the summation.

Most probable pair separation distance
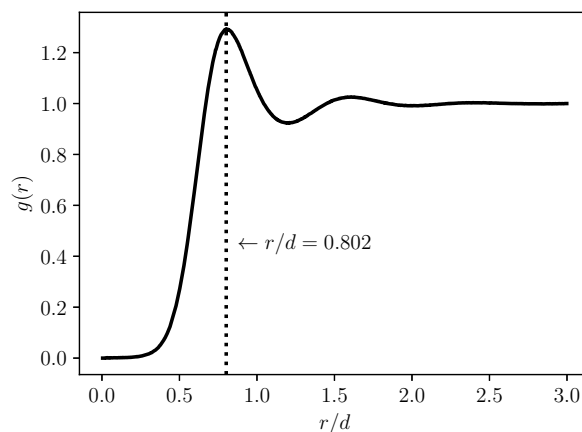
Figure 4.4: Radial distribution function $g(r)$ for uncharged nonbonded particles interacting via the parameterized GCMe with $N_\mathrm{m} = 4$. The oscillations indicate a pronounced liquid structure. The first peak, indicated by the dotted line, is the most probable separation distance between two particles.

Scaling law for polymer in athermal solvent

For a polymer in an athermal solvent, the radius of gyration scales as $R_\mathrm{g} \approx bN^{3/5}$, where b is the bond length and N is the chain length [69].

To test whether GCMe polymers can get the correct scaling, we simulated neutral systems with $M = 1$ polymer chain with varying chain lengths N and explicit solvent particles in the canonical (NVT) ensemble at temperature $T = 300$ K. The chain connectivity is modeled by a harmonic bond potential

$$u_\mathrm{harm}(r_{ij}) = \frac{1}{2}k(r_{ij} - b)^2,$$ (4.18)

where $k = 100k_\mathrm{B}T/d^2$ is the force constant. The monomer–monomer, monomer–solvent, and solvent–solvent interactions are identical to approximate an athermal solvent. Indeed, the fits of the R_g–N relationships for equilibrium bond lengths $b = 0.7d$ and $b = 0.8d$ in Fig. 4.5 give $R_\mathrm{g} \sim N^{0.592}$ and $R_\mathrm{g} \sim N^{0.599}$, respectively, which agree with the scaling law.
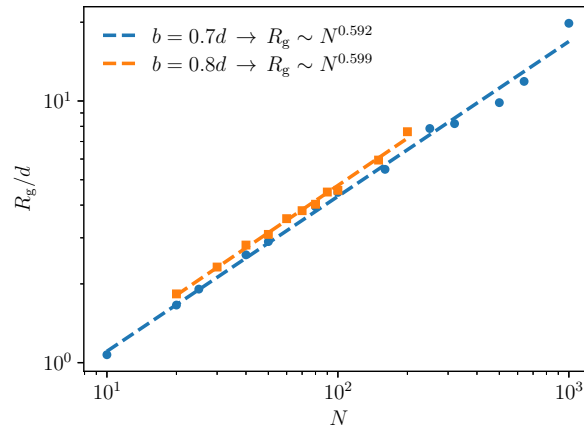
Figure 4.5: Radius of gyration R_g as a function of the chain length N and the equilibrium bond length b. The dashed lines are fits of the raw data.

Flory–Huggins parameter mapping

Since the GCM is phenomenologically equivalent to and can be considered a continuous version of the lattice-based Flory–Huggins (FH) theory [49, 50], it can be used to study liquid–liquid and liquid–solid interfaces. For a binary polymer mixture of A and B chains, the FH theory gives a free energy per unit volume f of

$$\frac{f}{k_B T} = \frac{\phi_A}{N_{p,A}} \ln \phi_A + \frac{\phi_B}{N_{p,B}} \ln \phi_B + \chi \phi_A \phi_B,$$

where ϕ_A and ϕ_B are the volume fractions of components A and B (with $\phi_A + \phi_B = 1$ such that all lattice sites are filled), $N_{p,A}$ and $N_{p,B}$ are the chain lengths of the A and B chains, and χ is a free mixing parameter. The sign of χ dictates the nature of the interactions between the A and B components: A–A and B–B contacts are favored when $\chi > 0$ while A–B interactions are preferred when $\chi < 0$. When χ gets sufficiently large, there are two minima separated by a maximum in the free energy curve, as shown in Fig. 4.6, indicating an equilibrium phase-separated state with A- and B-rich domains. If the chain lengths are equal ($N_p = N_{p,A} = N_{p,B}$), the minimum free energy is located at $\mu = \partial f / \partial \phi_A = 0$, or

$$\chi N_p = \frac{\ln\left[(1 - \phi_A)/\phi_A\right]}{1 - 2\phi_A}. \tag{4.19}$$

In the GCM, the χ parameter can be modeled by the excess repulsion parameter $\Delta A = A_{AB} - A_{AA}$, with $A_{AA} = A_{BB}$. As a first step to map ΔA to the χ parameter, we ran a series of MD simulations of A and B monomers in the canonical (NVT) ensemble at temperature $T = 300\,\text{K}$ and varying ΔA values, with each system having
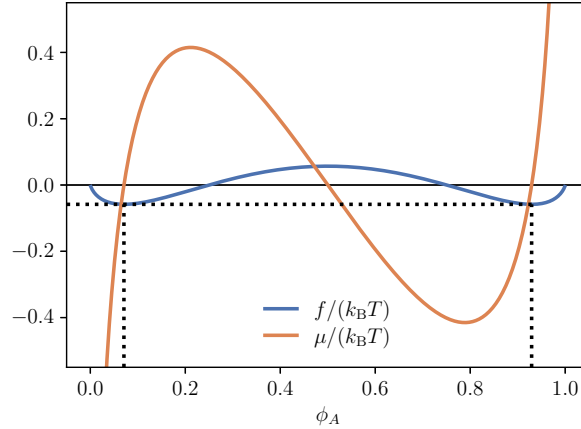
Figure 4.6: Free energy f (solid line) and chemical potential μ (dashed line) in the FH theory for $N_\mathrm{p} = 1$ and $\chi = 3$. The dotted lines indicate the coexistence volume fractions and the corresponding free energy.

dimensions of $20d \times 20d \times 50d$ and $N_A = N_B = 25,000$ particles of each type. The initial macrophase-separated configurations were generated by randomly placing only A or B particles in the left and right halves of the simulation box, respectively. For each simulation, energy minimization and system equilibration were performed over 5×10^6 timesteps of step size $t = 0.01\tau$, and data was collected over at least an additional 2×10^7 timesteps, which is on the order of 630 ns.

To determine the χ–ΔA relationship, we first computed the number density profiles of A and B particles across the interface by binning the z-axis into intervals, counting the number of relevant particles, and dividing the counts by the volume of the bins. Selected number density profiles are shown in Fig. 4.7. Then, the volume fraction $\phi_A = \rho_A/(\rho_A + \rho_B)$ for each ΔA value was evaluated using the average values of ρ_A and ρ_B over the A-rich domain where the total number density is homogeneous. Finally, the χ values were calculated by substituting the ϕ_A values into Eq. 4.19. Fig. 4.8 shows that χ is linearly proportional to ΔA, and linear regression over the intermediate ΔA regime yields the explicit scaling

$$\chi = 41.15\Delta A/A_{AA} = 1.63\Delta A/(d^3 k_\mathrm{B}T) \tag{4.20}$$

for systems with a number density of $\rho = 2.5d^{-3}$. As such, Eq. 4.20 is an effective mapping of the GCM onto the FH theory.
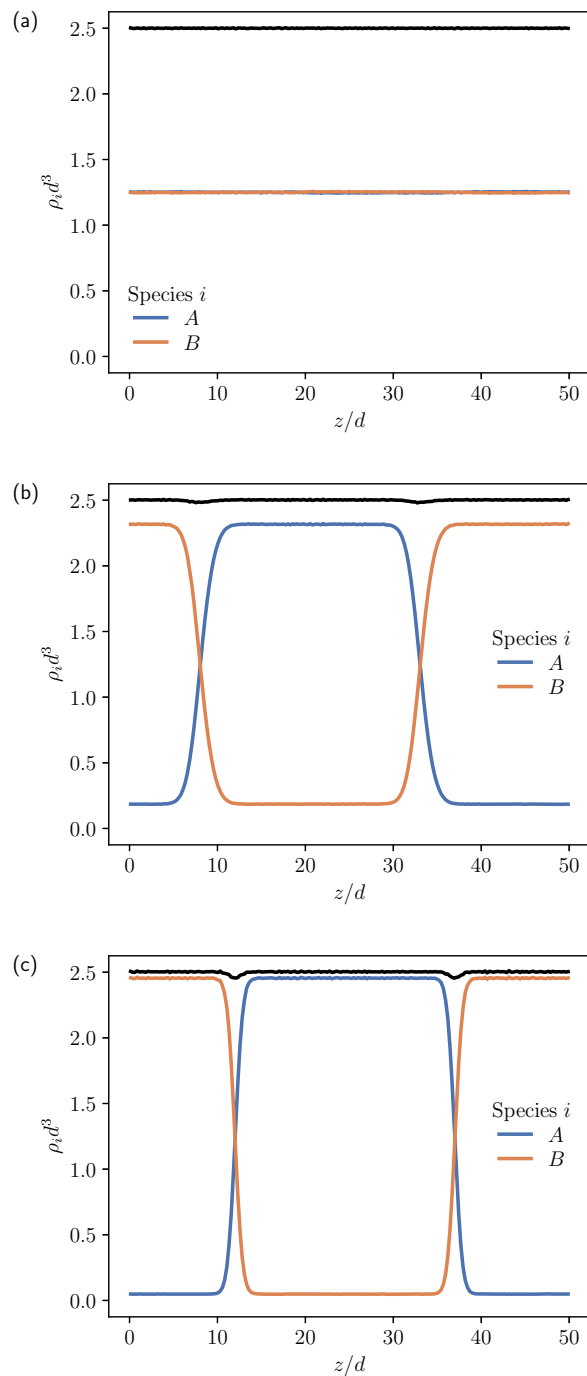
Figure 4.7: Number density profiles $\rho_i(z)$ of the A and B particles at excess repulsion parameters $\Delta A/A_{AA}$ of (a) 0.050, (b) 0.075, and (c) 0.100 in the Gaussian core model.
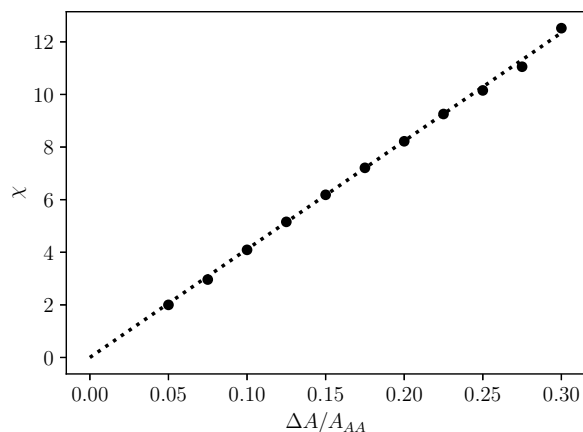
Figure 4.8: The Flory–Huggins χ parameter as a function of the excess repulsion parameter ΔA for systems with a number density of $\rho = 2.5d^{-3}$. The dotted line shows the best linear fit.

References

(1)   Ye, B. B.; Chen, S.; Wang, Z.-G. *J. Chem. Theory Comput.* **2024**, acs.jctc.4c00603, DOI: `10.1021/acs.jctc.4c00603`.

(2)   Gartner, T. E.; Jayaraman, A. *Macromolecules* **2019**, *52*, 755–786, DOI: `10.1021/acs.macromol.8b01836`.

(3)   Joshi, S. Y.; Deshmukh, S. A. *Mol. Simul.* **2021**, *47*, 786–803, DOI: `10.1080/08927022.2020.1828583`.

(4)   Nielsen, S. O.; Lopez, C. F.; Srinivas, G.; Klein, M. L. *J. Phys.: Condens. Matter* **2004**, *16*, R481–R512, DOI: `10.1088/0953-8984/16/15/R03`.

(5)   Ingólfsson, H. I.; Lopez, C. A.; Uusitalo, J. J., et al. *WIREs Comput. Mol. Sci.* **2014**, *4*, 225–248, DOI: `10.1002/wcms.1169`.

(6)   Brini, E.; Algaer, E. A.; Ganguly, P., et al. *Soft Matter* **2013**, *9*, 2108–2119, DOI: `10.1039/C2SM27201F`.

(7)   Fredrickson, G. H.; Ganesan, V.; Drolet, F. *Macromolecules* **2002**, *35*, 16–39, DOI: `10.1021/ma011515t`.

(8)   Lee, J.; Popov, Y. O.; Fredrickson, G. H. *J. Chem. Phys.* **2008**, *128*, 224908, DOI: `10.1063/1.2936834`.

(9)   Matsen, M. W. *J. Chem. Phys.* **2020**, *152*, 110901, DOI: `10.1063/1.5145098`.

(10) Fredrickson, G. H.; Delaney, K. T., *Field-theoretic simulations in soft matter and quantum fluids*; International series of monographs on physics 173; Oxford University Press: New York, NY, 2023, DOI: `10.1093/oso/9780192847485`.

(11) Villet, M. C.; Fredrickson, G. H. *J. Chem. Phys.* **2014**, *141*, 224115, DOI: `10.1063/1.4902886`.

(12) Delaney, K. T.; Fredrickson, G. H. *J. Phys. Chem. B* **2016**, *120*, 7615–7634, DOI: `10.1021/acs.jpcb.6b05704`.

(13) Lequieu, J. *J. Chem. Phys.* **2023**, *158*, 244902, DOI: `10.1063/5.0153104`.

(14) Jorgensen, W. L.; Madura, J. D.; Swenson, C. J. *J. Am. Chem. Soc.* **1984**, *106*, 6638–6646, DOI: `10.1021/ja00334a030`.

(15) Jorgensen, W. L.; Swenson, C. J. *J. Am. Chem. Soc.* **1985**, *107*, 569–578, DOI: `10.1021/ja00289a008`.

(16) Jorgensen, W. L. *J. Phys. Chem.* **1986**, *90*, 1276–1284, DOI: `10.1021/j100398a015`.

(17) Souza, P. C. T.; Alessandri, R.; Barnoud, J., et al. *Nat. Methods.* **2021**, *18*, 382–388, DOI: `10.1038/s41592-021-01098-3`.

(18) Kremer, K.; Grest, G. S. *J. Chem. Phys.* **1990**, *92*, 5057–5086, DOI: `10.1063/1.458541`.

(19) Frisch, H. L. *Science* **1965**, *150*, 1249–1254, DOI: `10.1126/science.150.3701.1249`.

(20) Hoogerbrugge, P. J.; Koelman, J. M. V. A. *Europhys. Lett.* **1992**, *19*, 155–160, DOI: `10.1209/0295-5075/19/3/001`.

(21) Español, P.; Warren, P. *Europhys. Lett.* **1995**, *30*, 191–196, DOI: `10.1209/0295-5075/30/4/001`.

(22) Groot, R. D.; Warren, P. B. *J. Chem. Phys.* **1997**, *107*, 4423–4435, DOI: `10.1063/1.474784`.

(23) Groot, R. D. *J. Chem. Phys.* **2003**, *118*, 11265–11277, DOI: `10.1063/1.1574800`.

(24) Berne, B. J.; Pechukas, P. *J. Chem. Phys.* **1972**, *56*, 4213–4216, DOI: `10.1063/1.1677837`.

(25) Stillinger, F. H. *J. Chem. Phys.* **1976**, *65*, 3968–3974, DOI: `10.1063/1.432891`.

(26) Prestipino, S.; Saija, F.; Giaquinta, P. V. *Phys. Rev. E* **2005**, *71*, 050102, DOI: `10.1103/PhysRevE.71.050102`.

(27) Ruppeiner, G.; Mausbach, P.; May, H.-O. *Fluid Phase Equilib.* **2021**, *542-543*, 113033, DOI: `10.1016/j.fluid.2021.113033`.

(28) Guenza, M. *Phys. Rev. Lett.* **2001**, *88*, 025901, DOI: `10.1103/PhysRevLett.88.025901`.

(29) Guenza, M. *Macromolecules* **2002**, *35*, 2714–2722, DOI: `10.1021/ma011596t`.

(30) McCarty, J.; Delaney, K. T.; Danielsen, S. P. O.; Fredrickson, G. H.; Shea, J.-E. *J. Phys. Chem. Lett.* **2019**, *10*, 1644–1652, DOI: `10.1021/acs.jpclett.9b00099`.

(31) Shen, K.; Sherck, N.; Nguyen, M., et al. *J. Chem. Phys.* **2020**, *153*, 154116, DOI: `10.1063/5.0022808`.

(32) Jedlinska, Z. M.; Tabedzki, C.; Gillespie, C., et al. *J. Chem. Phys.* **2023**, *159*, 014108, DOI: `10.1063/5.0145006`.

(33) Warren, P. B.; Vlasov, A.; Anton, L.; Masters, A. J. *J. Chem. Phys.* **2013**, *138*, 204907, DOI: `10.1063/1.4807057`.

(34) Kiss, P. T.; Sega, M.; Baranyai, A. *J. Chem. Theory Comput.* **2014**, *10*, 5513–5519, DOI: `10.1021/ct5009069`.

(35) Eslami, H.; Khani, M.; Müller-Plathe, F. *J. Chem. Theory Comput.* **2019**, *15*, 4197–4207, DOI: `10.1021/acs.jctc.9b00174`.

(36) Kung, W.; Olvera De La Cruz, M. *J. Chem. Phys.* **2007**, *127*, 244907, DOI: `10.1063/1.2822277`.

(37) Wang, Z.-G. *Phys. Rev. E* **2010**, *81*, 021501, DOI: `10.1103/PhysRevE.81.021501`.

(38) Ewald, P. P. *Ann. Phys.* **1921**, *369*, 253–287, DOI: `10.1002/andp.19213690304`.

(39) Gingrich, T. R.; Wilson, M. *Chem. Phys. Lett.* **2010**, *500*, 178–183, DOI: `10.1016/j.cplett.2010.10.010`.

(40) Coslovich, D.; Hansen, J.-P.; Kahl, G. *J. Chem. Phys.* **2011**, *134*, 244514, DOI: `10.1063/1.3602469`.

(41) Darden, T.; York, D.; Pedersen, L. *J. Chem. Phys.* **1993**, *98*, 10089–10092, DOI: `10.1063/1.464397`.

(42) Essmann, U.; Perera, L.; Berkowitz, M. L., et al. *J. Chem. Phys.* **1995**, *103*, 8577–8593, DOI: `10.1063/1.470117`.

(43) Toukmaji, A. Y.; Board, J. A. *Comput. Phys. Commun.* **1996**, *95*, 73–92, DOI: `10.1016/0010-4655(96)00016-1`.

(44) Groot, R.; Rabone, K. *Biophys. J.* **2001**, *81*, 725–736, DOI: `10.1016/S0006-3495(01)75737-2`.

(45) Guenza, M. G.; Dinpajooh, M.; McCarty, J.; Lyubimov, I. Y. *J. Phys. Chem. B* **2018**, *122*, 10257–10278, DOI: `10.1021/acs.jpcb.8b06687`.

(46) Lyubimov, I.; Guenza, M. G. *Phys. Rev. E* **2011**, *84*, 031801, DOI: `10.1103/PhysRevE.84.031801`.

(47) Lyubimov, I. Y.; Guenza, M. G. *J. Chem. Phys.* **2013**, *138*, 12A546, DOI: `10.1063/1.4792367`.

(48) Li, X.; Gao, L.; Fang, W. *PLoS ONE* **2016**, *11*, ed. by Huang, X., e0154568, DOI: `10.1371/journal.pone.0154568`.

(49) Flory, P. J. *J. Chem. Phys.* **1941**, *9*, 660–660, DOI: `10.1063/1.1750971`.

(50) Huggins, M. L. *J. Chem. Phys.* **1941**, *9*, 440–440, DOI: `10.1063/1.1750930`.

(51) Eastman, P.; Swails, J.; Chodera, J. D., et al. *PLoS Comput. Biol.* **2017**, *13*, ed. by Gentleman, R., e1005659, DOI: `10.1371/journal.pcbi.1005659`.

(52) Kondratyuk, N.; Nikolskiy, V.; Pavlov, D.; Stegailov, V. *Int. J. High Perform. Comput. Appl.* **2021**, *35*, 312–324, DOI: `10.1177/10943420211008288`.

(53) Pavlov, D.; Kolotinskii, D.; Stegailov, V. In *Parallel Processing and Applied Mathematics*, Wyrzykowski, R., Dongarra, J., Deelman, E., Karczewski, K., Eds., Series Title: Lecture Notes in Computer Science; Springer International Publishing: Cham, 2023; Vol. 13826, pp 346–358, DOI: `10.1007/978-3-031-30442-2_26`.

(54) Thompson, A. P.; Aktulga, H. M.; Berger, R., et al. *Comput. Phys. Commun.* **2022**, *271*, 108171, DOI: `10.1016/j.cpc.2021.108171`.

(55) Bureekaew, S.; Amirjalayer, S.; Tafipolsky, M., et al. *Phys. Status Solidi B* **2013**, *250*, 1128–1141, DOI: `10.1002/pssb.201248460`.

(56) Son, C. Y.; Wang, Z.-G. *Proc. Natl. Acad. Sci. U.S.A.* **2021**, *118*, e2020615118, DOI: `10.1073/pnas.2020615118`.

(57) Dwelle, K. A.; Willard, A. P. *J. Phys. Chem. C* **2019**, *123*, 24095–24103, DOI: `10.1021/acs.jpcc.9b06635`.

(58) Ye, B. B.; Wang, Z.-G. *Phys. Chem. Chem. Phys.* **2022**, *24*, 11573–11584, DOI: `10.1039/D2CP00166G`.

(59) Feng, G.; Li, S.; Atchison, J. S.; Presser, V.; Cummings, P. T. *J. Phys. Chem. C* **2013**, *117*, 9178–9186, DOI: `10.1021/jp403547k`.

(60) Feng, G.; Jiang, D.-e.; Cummings, P. T. *J. Chem. Theory Comput.* **2012**, *8*, 1058–1063, DOI: `10.1021/ct200914j`.

(61) Wu, H.; Li, H.; Solis, F. J.; Olvera De La Cruz, M.; Luijten, E. *J. Chem. Phys.* **2018**, *149*, 164701, DOI: `10.1063/1.5047550`.

(62) Pogharian, N.; Dos Santos, A. P.; Ehlen, A.; Olvera De La Cruz, M. *J. Chem. Phys.* **2024**, *160*, 094704, DOI: `10.1063/5.0185570`.

(63) Boda, D.; Gillespie, D.; Nonner, W.; Henderson, D.; Eisenberg, B. *Phys. Rev. E* **2004**, *69*, 046702, DOI: `10.1103/PhysRevE.69.046702`.

(64) Nguyen, T. D.; Li, H.; Bagchi, D.; Solis, F. J.; Olvera De La Cruz, M. *Comput. Phys. Commun.* **2019**, *241*, 80–91, DOI: `10.1016/j.cpc.2019.03.006`.

(65) Siepmann, J. I.; Sprik, M. *J. Chem. Phys.* **1995**, *102*, 511–524, DOI: `10.1063/1.469429`.

(66) Reed, S. K.; Lanning, O. J.; Madden, P. A. *J. Chem. Phys.* **2007**, *126*, 084704, DOI: `10.1063/1.2464084`.

(67) Smith, A. M.; Lee, A. A.; Perkin, S. *J. Phys. Chem. Lett.* **2016**, *7*, 2157–2163, DOI: `10.1021/acs.jpclett.6b00867`.

(68) Huang, J. *J. Phys. Chem. C* **2018**, *122*, 3428–3433, DOI: `10.1021/acs.jpcc.7b11093`.

(69) Rubinstein, M.; Colby, R. H., *Polymer physics*; Oxford University Press: Oxford ; New York, 2003.

Chapter 5

CHAIN LENGTH AND SURFACE POLARIZABILITY EFFECTS IN POLYMERIC IONIC LIQUIDS

Building on our previous work on monomeric room-temperature ionic liquids (RTILs) and transitioning to the polyelectrolyte systems we aim to explore, this chapter examines polymeric ionic liquid (PIL) electric double-layer capacitors (EDLCs). PILs share many of the advantageous physicochemical properties of RTILs while benefitting from the increased stability and design versatility inherent to polyelectrolytes, positioning them as prime electrolyte candidates for electrochemical and electromechanical devices. Although recent experimental and theoretical studies have highlighted the wide electrochemical windows and exceptionally high electrical double-layer (EDL) capacitance of PILs, the underlying physical mechanisms remain unclear due to a lack of particle-based theoretical or simulation models. To address this gap, we utilize the Gaussian core model with smeared electrostatics (GCMe) to systematically investigate the effects of the potential difference, relative permittivity, chain length, and electrode polarizability on the EDL structure and capacitance behavior. This study aims to provide a deeper understanding of the factors influencing the performance of PIL EDLCs and contribute to their development.

5.1 Introduction

Polymeric ionic liquids (PILs) are a distinct class of polymers composed of ionic liquid monomeric units [1]. They exhibit an unique combination of the advantageous properties of ionic liquids and the sequence complexity and mechanical characteristics of polyelectrolytes [2, 3]. Like monomeric room-temperature ionic liquids (RTILs), PILs have low volatility [2–4], high chemical and thermal stability [2–5], and broad electrochemical windows [2, 4]. Additionally, they possess superior mechanical stability and are leakage-proof compared to their monomeric counterparts, owing to their polymeric backbones [2, 3, 6]. Notably, PILs have been shown to be able to overcome the typical trade-offs between mechanical strength and conductivity in polymer electrolytes [3, 7–11], achieving both high mechanical stability and ionic conductivity [5, 8, 12–14]. These distinctive physicochemical properties have attracted significant attention to PILs in recent years and made them prime candidates for a variety of applications, including drug delivery [4, 15–17],

catalysts [4, 18], precursors [3, 5, 19], surfactants [3, 5], and the design of smart materials [5].

One of the most notable applications of PILs is in electrochemical devices [2–6, 20], such as electric double-layer capacitors (EDLCs). A key performance indicator of an EDLC is its energy density, which is determined by the electrical double-layer (EDL) structure at the ion–electrode interface and influenced by the choice of the electrolyte and the electrode, and cyclability. The energy U that an EDLC can store scales as $CV^2/2$, where C is the capacitance and V is the voltage, so PILs are excellent electrolytes due to their wide operational voltage windows, high mechanical stability, and high conductivity. Indeed, experimental [21] and theoretical studies [22] of oligomeric ionic liquids have demonstrated exceptionally high EDL capacitance that surpasses what is possible with monomeric RTILs.

However, the molecular description of the EDLs in PIL EDLCs and the underlying physics behind this energy density improvement from RTIL EDLCs to PIL EDLCs are not fully understood, largely due to a lack of particle-based theoretical studies and computer simulations. To address this gap, we use the Gaussian core model with smeared electrostatics (GCMe) established in the previous chapter to systematically investigate the effects of the chain length and electrolyte and electrode polarizabilities on the energy storage of PIL EDLCs.

5.2   Model and methods

Simulations were carried out using OpenMM [23] in the canonical ensemble with $N_p = 10,000$ equisized charged monomers and a temperature of $T = 300$ K. Following our parametrization of the GCMe previously, the system has a number density of $\rho d^3 = 2.5$, and the ions are approximately the size of a $(CH_2)_3$ group in a straight-chain alkane ($N_m = 4$, $d = 0.592$ nm, $m = 72.1$ g/mol). The solvent-free electrolyte consists solely of symmetric (poly)anions and (poly)cations with the same chain length N. The chain connectivity is modeled by a harmonic bond potential

$$u_{\text{harm}}(r_{ij}) = \frac{1}{2}k_{ij}(x_{ij} - b_{ij})^2, \tag{5.1}$$

where $k_{ij} = 100k_BT/d^2$ is the force constant and $b_{ij} = 0.7d$ is the equilibrium bond length. These bond parameters align with those typically used in conjunction with soft-core models [24–26]. The electrolyte polarization is implicitly accounted for using a dielectric continuum with the relative permittivity of either a typical ionic liquid ($\varepsilon_r = 12$) [27–29] or water ($\varepsilon_r = 78$).

The real systems are initialized by first determining the L_x and L_y values that will accommodate the periodic placement of the surface particles, which are half the size of the electrolyte particles and arranged in a hexagonal close-packed lattice, and then L_z, which is constrained by the number of particles and number density. For the parameters we chose, our real systems have dimensions of approximately $12.5d \times 12.99d \times 49.27d$. Then, the system is randomly filled with N_p ions or $M \equiv N_p/N$ polyelectrolytes, and undergoes a local energy minimization. Finally, for the systems with perfectly conducting boundaries, the simulation box is doubled in width so that the real system can be reflected over the surface at $z = 0$ to generate the image charges. For the systems with nonmetal boundaries with no image charges, the z-dimension of the simulation box is instead tripled to introduce a sufficiently large void between periodic replicas in the z-direction so that the Yeh–Berkovitz correction [30, 31] can be used to remove the long-range electrostatic slab–slab interactions. In either case, because the simulations still have periodic boundary conditions, we can continue to use the fast PME method to evaluate the long-range electrostatic interactions, despite the lack of actual periodicity in the z-direction.

Potential differences ΔV in the z-direction are applied using the constant charge method (CCM), in which charges are assigned to the explicit particles that constitute the surfaces. Although CCM typically does not maintain electrode equipotentiality, it does so in systems with perfectly conducting boundaries when the image charge effect is included [32]. As such, CCM with the method of image charges is equivalent to the constant potential method or simply applying a uniform electric field $E = \Delta V/L_z$ in the z-direction. The target surface charge density $\sigma_{q,s}$ is related to the potential difference via Gauss's law:

$$\frac{q_{i,\,\text{wall}}}{2} = \frac{L_x L_y \sigma_{q,s}}{N_{\text{wall}}} = \frac{L_x L_y \varepsilon_0 \varepsilon_r E}{N_{\text{wall}}} = \frac{L_x L_y \varepsilon_0 \varepsilon_r \Delta V}{L_z N_{\text{wall}}}, \tag{5.2}$$

where $q_{i,\,\text{wall}}$ is the charge of a surface particle i, N_{wall} is the number of particles in each surface, and ε_0 is the vacuum permittivity.

For each simulation, system equilibration was performed over 5×10^6 timesteps of step size $t = 0.01\tau$, and data were collected over at least an additional 2×10^7 timesteps, which is on the order of 600 ns.

5.3   Results and discussion

To quantify the energy storage in EDLCs, we calculated the differential capacitance C_d. First, we evaluate the surface charge density, which has been shown [33, 34] to

be obtainable from the charge density profile $\rho_q(z)$ using

$$\langle\sigma_q\rangle = \sigma_{q,\text{s}} + \langle\sigma_{q,\text{p}}\rangle = \frac{\varepsilon_0\varepsilon_r\Delta V}{L_z} - \frac{1}{L_z}\int_0^{L_z} z\langle\rho_q(z)\rangle\,dz, \tag{5.3}$$

where the static term $\sigma_{q,\text{s}}$ accounts for the applied electric field and the polarization term $\sigma_{q,\text{p}}$ captures the spatial reorientation of ions in the electrolyte in response to the potential difference. The voltage-dependent differential capacitance is then given by

$$C_\text{d} = \frac{\partial\langle\sigma_q\rangle}{\partial\Delta V}, \tag{5.4}$$

with the area under the C_d–ΔV curve being proportional to the stored energy in the EDLC.

We start by examining how the chain length impacts the energy storage in systems with perfectly conducting electrodes and a high relative permittivity of $\varepsilon_\text{r} = 78$. As shown in Fig. 5.1, PIL EDLCs exhibit higher surface charge densities compared to RTIL EDLCs at all potential differences. This increase in the surface charge density in PIL EDLCs is driven by the connectivity between the charged monomers. When an ion is attracted to and moves towards the electrode, it forces adjacent bonded co-ions to follow, turning the ion–electrode interaction into an effective multivalent electrostatic interaction. Consequently, the electrodes saturate more quickly with ions of the same charge in the PIL EDLCs when a potential difference is first applied, as illustrated in Fig. 5.2.

Figure 5.2: System snapshots of electric double-layer capacitors using (a) a monomeric room-temperature ionic liquid ($N = 1$), (b) a polymeric ionic liquid with chain length $N = 2$, or (c) a polymeric ionic liquid with chain length $N = 10$ as the electrolyte with a static surface charge density of $\sigma_{q,\text{s}} = 0.0134e/d^2$ (or applied potential difference of $\Delta V = 5k_\text{B}T/e$) and perfectly conducting electrodes. The blue and red colors represent the anions and cations, respectively.

Since the differential capacitance represents the change in σ_q with respect to ΔV, we expect the C_d curves to have higher peaks for the PIL EDLCs. Indeed, the
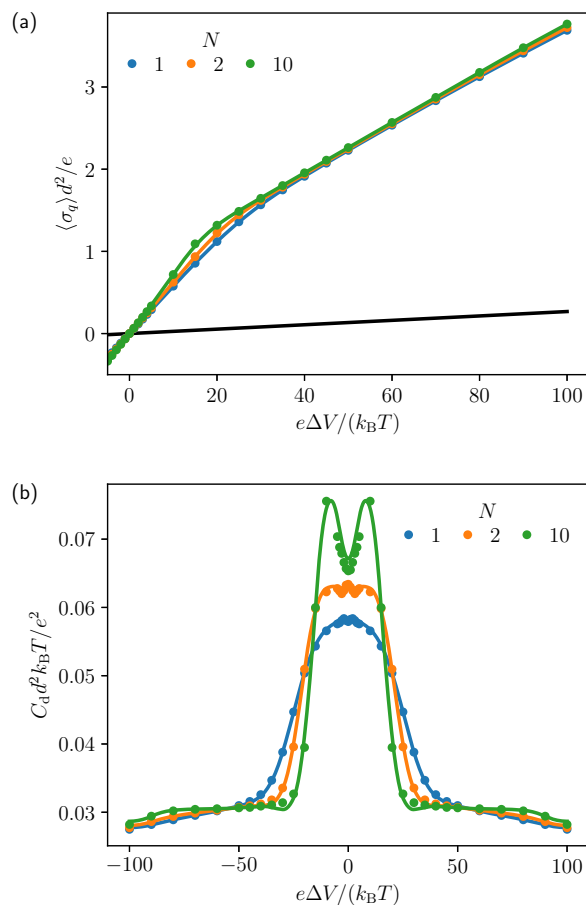
Figure 5.1: (a) Surface charge density σ_q and (b) differential capacitance C_d as functions of the potential difference ΔV for monomeric room-temperature ionic liquid and polymeric ionic liquid electric double-layer capacitors with high relative permittivities of $\varepsilon_r = 78$ and perfectly conducting electrodes. The black solid line in (a) denotes the static contributions to σ_q from the potential differences.

peak increases monotonically with the chain length for the PILs that we tested, as shown in Fig. 5.1b. The capacitance also starts decaying at a lower ΔV since the first layer next to the electrode saturates more quickly in PIL EDLCs. Perhaps more interestingly, the capacitance behavior transitions from a bell-shaped curve for RTIL EDLCs, as predicted by the Kornyshev model for dense electrolytes [28], to a camel-shaped one as the chain length increases. This results in two peaks in the capacitance of the $N = 10$ PIL systems that are no longer centered on $\Delta V = 0$ but rather at some moderate ΔV values of opposite signs. This significantly increases the area under the C_d–ΔV curve, greatly enhancing the energy storage potential of PIL EDLCs. The physical mechanism behind this phenomenon will become clearer when we look at systems with stronger electrostatics in the discussion that follows.
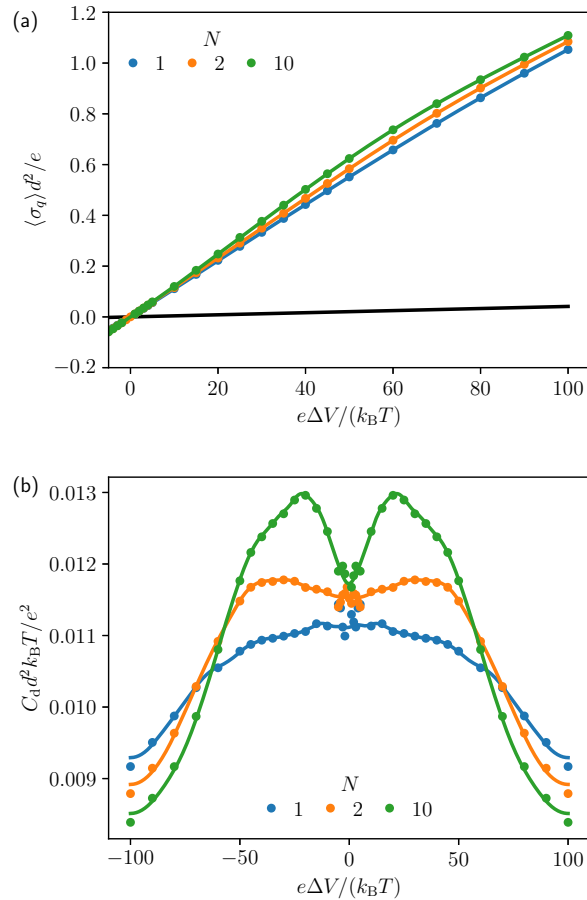
Figure 5.3: (a) Surface charge density σ_q and (b) differential capacitance C_d as functions of the potential difference ΔV for monomeric room-temperature ionic liquid and polymeric ionic liquid electric double-layer capacitors with low relative permittivities of $\varepsilon_\mathrm{r} = 12$ and perfectly conducting electrodes. The black solid line in (a) denotes the static contributions to σ_q from the potential differences.

For systems with a lower relative permittivity of $\varepsilon_\mathrm{r} = 12$, we observed σ_q–ΔV and C_d–ΔV relationships with behavior similar to those in the $\varepsilon_\mathrm{r} = 78$ systems in Fig. 5.3. However, the $N = 2$ PIL system also exhibits two capacitance peaks that are not centered on $\Delta V = 0$. Moreover, the range of potential differences over which the capacitance reaches its peak and begins to decline is now much wider, providing us with an opportunity to understand why the peak occurs at a non-zero ΔV in the $N = 10$ PIL systems. From the system snapshot in Fig. 5.4a, we observe that oppositely charged polyelectrolytes pair together in an alternating pattern while adsorbed on the electrodes when a weak potential difference is first applied. As ΔV increases to moderate values, Fig. 5.4b shows that this ordering begins to disappear, and polycations start to accumulate on the left electrode in greater numbers than the
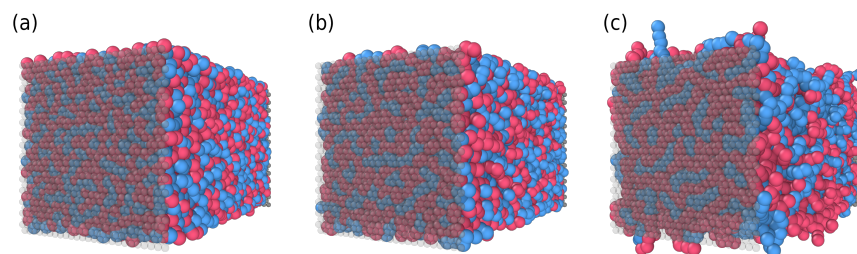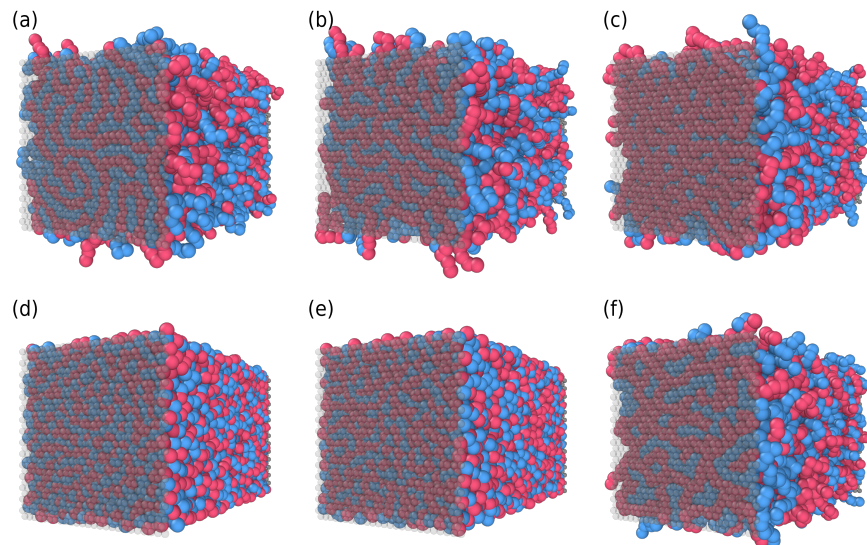
Figure 5.4: System snapshots of electric double-layer capacitors using (d, e) a monomeric ionic liquid ($N = 1$) or (a–c, f) a polymeric ionic liquid with chain length $N = 10$ as the electrolyte with static surface charge densities of (a, d) $\sigma_{q,s} = 0.0134e/d^2$ (or applied potential difference of $\Delta V = 5k_BT/e$), (b, e) $\sigma_{q,s} = 0.0536e/d^2$ (or $\Delta V = 20k_BT/e$), or (c, f) $\sigma_{q,s} = 0.458e/d^2$, and (a–e) perfectly conducting or (f) nonmetal electrodes. The blue and red colors represent the anions and cations, respectively.

polyanions. At even higher ΔV, the in-plane correlation between the polyanions and polycations has completely dissipated, and the adlayer comprises only polyanions, as shown in Fig. 5.4. This breaking of the polyelectrolyte pairs, which allows the adsorption of only one type of charged species on the electrodes, likely explains the sharper increases in the surface charge density in PIL EDLCs and the capacitance peak at some moderate ΔV since energy is predominantly stored when the EDL consists of layers with alternating charges away from the electrodes.

In contrast, such enhanced energy storage is not achievable in RTIL EDLCs due to the absence of collective monomer motion enabled by the connectivity in PILs. As shown in Figs. 5.4d and e, there is no evident ion pairing in RTIL EDLCs across the diverse ΔV values we tested. Hence, cations begin to accumulate on the electrodes and the anions are repelled, even at low ΔV. Consequently, the surface charge density increases most rapidly when a potential difference is first applied, resulting in a capacitance peak at $\Delta V = 0$. Similarly, there is no ordering in PIL EDLCs with nonmetal electrodes, even at high static surface charge densities, because of the lack of attractive image charge interactions that enable the repelled charged species—the

polyanions in Fig. 5.4f—to stay adsorbed on the left electrode.

Therefore, PILs can have significantly outperform monomeric RTILs in energy density when used as the electrolyte in EDLCs with perfectly conducting electrodes. With PILs, the connectivity between monomers brings multiple co-ions into the adlayer for each ion drawn to the electrode, resulting in a faster rise in the surface charge density and a higher capacitance peak. Additionally, the pairing of oppositely charged polyelectrolytes adsorbed on the electrodes—possible only with the attractive image charge interactions from perfectly conducting electrodes—leads to a transition from a bell-shaped capacitance curve to a camel-shaped one. This chain length effect and in-plane ordering come together to give PIL EDLCs much higher potential energy storage than RTIL EDLCs.

5.4 Conclusion

In this chapter, we highlighted the critical role of chain length and the influence of image charges in enhancing the energy density in ionic liquid EDLCs. PIL EDLCs exhibit higher surface charge densities at all potential differences compared to RTIL EDLCs due to the bonds between the constituent monomers. This connectivity enables PILs to saturate the electrodes more quickly with ions of the same charge when a potential difference is applied. Consequently, PIL EDLCs show higher but narrower capacitance peaks as the chain length increases.

In PIL EDLCs with perfectly conducting electrodes and utilizing PILs with higher chain lengths and lower relative permittivities, we also observed an in-plane pairing of oppositely charged polyelectrolytes adsorbed on the electrodes. This pairing required a strong external electric field to break apart, shifting the capacitance peak from $\Delta V = 0$ to a moderate ΔV and transitioning the capacitance curve from a bell shape typical of RTIL EDLCs to camel-shaped curves. The offset of the peaks, along with their higher magnitudes, significantly improves the energy storage potential in PIL EDLCs since the area underneath the C_d–ΔV curve is proportional to the stored energy. This phenomenon is not possible in monomeric RTIL EDLCs due to the lack of connectivity that turns the anion–cation interaction into a multivalent one, nor in PIL EDLCs with nonmetal electrodes due to the absense of attractive image charge interactions that allows both charged species to stay adsorbed to the electrodes even when the external electric field repels one of them.

Our findings emphasize that the interplay between PIL chain length, electrolyte polarizability, and electrode polarizability profoundly impacts the energy storage

mechanisms in EDLCs. Future investigations can build upon these insights by manipulating these key factors to optimize EDLC performance. Additionally, exploring other possible tuning methods, such as introducing asymmetry between the polyanion and polycation or increasing the screening length through the addition of organic solvents, could further increase the capacitance peaks for higher energy storage.

References

(1) *Polymerized Ionic Liquids*; Eftekhari, A., Ed.; The Royal Society of Chemistry: 2017, DOI: `10.1039/9781788010535`.

(2) Eshetu, G. G.; Mecerreyes, D.; Forsyth, M.; Zhang, H.; Armand, M. *Mol. Syst. Des. Eng.* **2019**, *4*, 294–309, DOI: `10.1039/C8ME00103K`.

(3) Ganesan, V. *Mol. Syst. Des. Eng.* **2019**, *4*, 280–293, DOI: `10.1039/C8ME00114F`.

(4) Lebedeva, O.; Kultin, D.; Kustov, L. *Eur. Polym. J.* **2024**, *203*, 112657, DOI: `10.1016/j.eurpolymj.2023.112657`.

(5) Mecerreyes, D. *Prog. Polym. Sci.* **2011**, *36*, 1629–1648, DOI: `10.1016/j.progpolymsci.2011.05.007`.

(6) Xiao, W.; Yang, Q.; Zhu, S. *Sci. Rep.* **2020**, *10*, 7825, DOI: `10.1038/s41598-020-64689-8`.

(7) Weber, R. L.; Ye, Y.; Schmitt, A. L., et al. *Macromolecules* **2011**, *44*, 5727–5735, DOI: `10.1021/ma201067h`.

(8) Ye, Y.; Choi, J.-H.; Winey, K. I.; Elabd, Y. A. *Macromolecules* **2012**, *45*, 7027–7035, DOI: `10.1021/ma301036b`.

(9) Sanoja, G. E.; Popere, B. C.; Beckingham, B. S., et al. *Macromolecules* **2016**, *49*, 2216–2223, DOI: `10.1021/acs.macromol.5b02614`.

(10) Harris, M. A.; Heres, M. F.; Coote, J., et al. *Macromolecules* **2018**, *51*, 3477–3486, DOI: `10.1021/acs.macromol.7b02729`.

(11) Mapesa, E. U.; Chen, M.; Heres, M. F., et al. *Macromolecules* **2019**, *52*, 620–628, DOI: `10.1021/acs.macromol.8b02143`.

(12) Shaplov, A. S.; Vlasov, P. S.; Lozinskaya, E. I., et al. *Macromolecules* **2011**, *44*, 9792–9803, DOI: `10.1021/ma2014518`.

(13) Choi, J.-H.; Ye, Y.; Elabd, Y. A.; Winey, K. I. *Macromolecules* **2013**, *46*, 5290–5300, DOI: `10.1021/ma400562a`.

(14) Zhang, Z.; Krajniak, J.; Keith, J. R.; Ganesan, V. *ACS Macro Lett.* **2019**, *8*, 1096–1101, DOI: `10.1021/acsmacrolett.9b00478`.

(15) Liu, C.; Raza, F.; Qian, H.; Tian, X. *Biomater. Sci.* **2022**, *10*, 2524–2539, DOI: `10.1039/D2BM00046F`.

(16) Qader, I. B.; Prasad, K. *Pharm. Res.* **2022**, *39*, 2367–2377, DOI: `10.1007/s11095-022-03315-w`.

(17) Gao, Y.; Zhang, W.; Li, L., et al. *Chem. Eng. J.* **2023**, *452*, 139248, DOI: `10.1016/j.cej.2022.139248`.

(18) Migowski, P.; Lozano, P.; Dupont, J. *Green Chem.* **2023**, *25*, 1237–1260, DOI: `10.1039/D2GC04749G`.

(19) Wang, F.; Duan, D.; Singh, M., et al. *Energy Environ. Mater.* **2023**, *6*, e12435, DOI: `10.1002/eem2.12435`.

(20) Safa, M.; Chamaani, A.; Chawla, N.; El-Zahab, B. *Electrochim. Acta* **2016**, *213*, 587–593, DOI: `10.1016/j.electacta.2016.07.118`.

(21) Matsumoto, M.; Shimizu, S.; Sotoike, R., et al. *J. Am. Chem. Soc.* **2017**, *139*, 16072–16075, DOI: `10.1021/jacs.7b09156`.

(22) Lian, C.; Su, H.; Liu, H.; Wu, J. *J. Phys. Chem. C* **2018**, *122*, 14402–14407, DOI: `10.1021/acs.jpcc.8b04464`.

(23) Eastman, P.; Swails, J.; Chodera, J. D., et al. *PLoS Comput. Biol.* **2017**, *13*, ed. by Gentleman, R., e1005659, DOI: `10.1371/journal.pcbi.1005659`.

(24) Terrón-Mejía, K. A.; López-Rendón, R.; Goicochea, A. G. *J. Phys.: Condens. Matter* **2016**, *28*, 425101, DOI: `10.1088/0953-8984/28/42/425101`.

(25) Li, X.; Gao, L.; Fang, W. *PLoS ONE* **2016**, *11*, ed. by Huang, X., e0154568, DOI: `10.1371/journal.pone.0154568`.

(26) Chen, S.; Wang, Z.-G. *Phys. Rev. Lett.* **2023**, *131*, 218201, DOI: `10.1103/PhysRevLett.131.218201`.

(27) Wakai, C.; Oleinikova, A.; Ott, M.; Weingärtner, H. *J. Phys. Chem. B* **2005**, *109*, 17028–17030, DOI: `https://doi.org/10.1021/jp053946+`.

(28) Kornyshev, A. A. *J. Phys. Chem. B* **2007**, *111*, 5545–5557, DOI: `10.1021/jp067857o`.

(29) Bazant, M. Z.; Storey, B. D.; Kornyshev, A. A. *Phys. Rev. Lett.* **2011**, *106*, 046102, DOI: `10.1103/PhysRevLett.106.046102`.

(30) Yeh, I.-C.; Berkowitz, M. L. *J. Chem. Phys.* **1999**, *111*, 3155–3162, DOI: `10.1063/1.479595`.

(31) Ballenegger, V.; Arnold, A.; Cerdà, J. J. *J. Chem. Phys.* **2009**, *131*, 094107, DOI: `10.1063/1.3216473`.

(32) Zeng, L.; Tan, X.; Ji, X., et al. *Journal of Energy Chemistry* **2024**, S2095495624001694, DOI: `10.1016/j.jechem.2024.02.043`.

(33) Hautman, J.; Halley, J. W.; Rhee, Y.-J. *J. Chem. Phys.* **1989**, *91*, 467–472, DOI: `10.1063/1.457481`.

(34) Qing, L.; Zhao, S.; Wang, Z.-G. *J. Phys. Chem. B* **2021**, *125*, 625–636, DOI: `10.1021/acs.jpcb.0c09332`.

ADSORPTION BEHAVIOR AND CHARGING DYNAMICS IN POLYANION–COUNTERION–SOLVENT SYSTEMS

Polyelectrolytes are prevalent and play crucial roles in natural environments, biological systems, and everyday products. In nature, they are found in the adhesives secreted by mussels and barnacles, enabling these organisms to stick to wet surfaces like rocks and ship hulls. In drug delivery, polyelectrolytes form the basis of hydrogels that interact with cells and tissues to control the release of therapeutic agents and facilitate wound healing. In personal care products like shampoos and conditioners, polyelectrolytes help detangle hair and remove dirt and oils by mediating interactions with negatively charged hair surfaces. Of utmost significance today is the use of polyelectrolytes in energy storage devices like batteries and electric double-layer capacitors (EDLCs), which power commonly used electronics ranging from smartphones and laptops to electric vehicles.

The common thread in these examples is the predominant role of electrostatic forces in adhesion and adsorption. Understanding these forces is essential for optimizing the performance of polyelectrolytes across various applications. In this chapter, we investigate how boundary polarizability affects the adsorption behavior of a salt-free polyanion–counterion–solvent system on perfectly conducting and nonmetal boundaries using our Gaussian core model with smeared electrostatics (GCMe). Then, we explore how the different adsorption behavior impacts the energy storage and charging/discharging dynamics of polyelectrolyte EDLCs. Although the discussion is framed in the context of polyelectrolyte EDLCs, our findings may have broader implications for the general applications of polyelectrolytes near neutral and charged surfaces.

This chapter includes content from our previously published article:

Ye, B. B.; Chen, S.; Wang, Z.-G. *J. Chem. Theory Comput.* **2024**, acs.jctc.4c00603, DOI: `10.1021/acs.jctc.4c00603`

6.1 Introduction
EDLCs have received significant interest in the recent years owing to their substantial power densities, fast charge and discharge rates, and sustainable cyclability compared

to other energy storage devices, such as batteries and fuel cells [2]. The performance of an EDLC is strongly correlated with the electrical double-layer (EDL) structure at the ion–electrode interface, which is largely dependent on the choice of the electrolyte and the electrode. The maximum energy U an EDLC can store scales as $CV^2/2$, where C is the capacitance and V is the voltage, so electrolytes with large operational voltage windows, great mechanical stability, and high conductivity have been sought after. As a result, polyelectrolytes and polymeric ionic liquids have recently attracted considerable attention since they satisfy the design criteria with their wide electrochemical windows, outstanding thermal stability, and notable mechanical strength and conductivity [3, 4]. Indeed, experimental studies and computer simulations [5–7] have shown that polyelectrolytes have exceptionally high EDL capacitance, making them prime electrolyte candidates for the next generation of EDLCs.

On the other hand, limited attention has been given to how the polarizability of the boundary material affects the adsorption behavior and transport of the charged species in polyelectrolyte EDLCs, in part due to the technical challenges of efficiently conducting particle-based simulations while accounting for image charge effects. Existing studies have largely focused on how repulsive image charges and finite potential differences influence polyelectrolyte adsorption behavior and energy storage. For example, Monte Carlo simulations by Wang et al. [8] have elucidated how repulsive image charges can either enhance or penalize polyelectrolyte adsorption depending on the polyelectrolyte charge fraction and surface charge distribution. MD efforts by Bagchi et al. [9] have revealed that repulsive image charges give rise to enhanced energy storage in polyelectrolyte EDLCs at low surface charge densities due to charge amplification. However, the effect of attractive image charges on polyelectrolyte adsorption behavior is not well understood. To this end, we use our Gaussian core model with smeared electrostatics (GCMe) to study the adsorption behavior of polyanions on neutral parallel planar perfectly conducting and nonmetal boundaries. We then explore how these interactions influence the energy storage and charging/discharging dynamics with when potential differences are applied.

6.2 Model and methods

Simulations were carried out using OpenMM [10] in the canonical ensemble with $N_p = 96,000$ equisized particles and a temperature of $T = 300$ K. The salt-free electrolyte consists of polyanions with chain length $N = 60$, their counterions, each with ion fraction x_p, and solvent particles to fill the empty space. The chain

connectivity in the polyanions is modeled by a harmonic bond potential

$$u_{\text{harm}}(r_{ij}) = \frac{1}{2}k(r_{ij} - b)^2, \tag{6.1}$$

where $k = 100k_{\text{B}}T/d^2$ is the force constant and $b = 0.8d$ is the equilibrium bond length, which coincides with where the radial distribution function for a neutral GCMe fluid (Fig. 4.4) has its maximum. The solvent polarization is implicitly accounted for using a dielectric continuum with the relative permittivity of water $\varepsilon_{\text{r}} = 78$.

The real systems are initialized by first determining the L_x and L_y values that will accommodate the periodic placement of the surface particles, which are half the size of the electrolyte particles and arranged in a hexagonal close-packed lattice, and then L_z, which is constrained by the number of particles and number density. For the parameters we chose, our real systems have dimensions of approximately $25d \times 25.11d \times 61.16d$. Then, the system is randomly filled with the polyanions, counterions, and solvent particles, and undergoes a local energy minimization. Finally, for the systems with perfectly conducting boundaries, the simulation box is doubled in width so that the real system can be reflected over the surface at $z = 0$ to generate the image charges. For the systems with nonmetal boundaries with no image charges, the z-dimension of the simulation box is instead tripled to introduce a sufficiently large void between periodic replicas in the z-direction so that the Yeh–Berkovitz correction [11, 12] can be used to remove the long-range electrostatic slab–slab interactions. In either case, because the simulations still have periodic boundary conditions, we can continue to use the fast PME method to evaluate the long-range electrostatic interactions despite the lack of actual periodicity in the z-direction.

For each simulation, system equilibration was performed over 5×10^6 timesteps of step size $t = 0.02\tau$, and data were collected over at least an additional 2×10^7 timesteps, which are on the order of 1 μs.

6.3 Results and discussion

Adsorption behavior with neutral surfaces

The polyanion and counterion number density profiles for the systems with nonmetal boundaries are presented in Fig. 6.1. As expected, they exhibit the same general trends as the density profiles obtained using classical polymer density functional theory (PDFT) [13, 14]. In systems with low polyanion fractions, such as the

Figure 6.1: Ensemble-averaged (a) polyanion and (b) counterion number density profiles normalized by their respective total number densities, and (c) the charge density profile normalized by the total counterion charge density near a surface for a salt-free polyanion–counterion–solvent system confined by nonmetal boundaries. The total number density differs from the bulk number density in the center of the system by less than 2%.
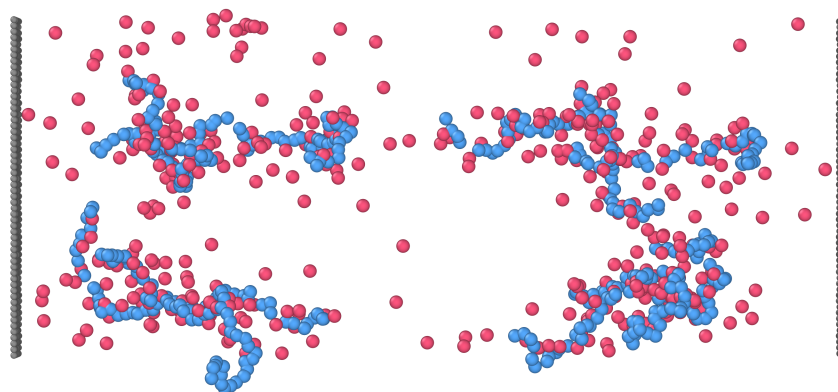
Figure 6.2: Representative simulation snapshot of the real polyanion–counterion–solvent system with nonmetal boundaries at $x_p = 0.005$. Solvent particles are not shown.

$x_p = 0.005$ system shown in Fig. 6.2, there is a net depletion of polyanions near the surfaces due to the conformational entropy penalty for them to adsorb onto the surfaces. Instead, the polyanions aggregate a short distance from the surfaces, as shown by the peak centered at $z = 7.5d$ in Fig. 6.1a. The counterions are also depleted in the vicinity of the surfaces due to their favorable interactions with the polyanions, although to a lesser extent since they are nonbonded and do not suffer from an entropic penalty when they absorb onto the surfaces. This local charge imbalance gives rise to an effective EDL, shown in Fig. 6.1c, where the positively-charged inner layers are screened by the negatively-charged outer layers.

As x_p increases, the nominal Debye length $\lambda_D = [4\pi\lambda_B\rho(x_p + x_+)]^{-1/2}$, which is a measure of the range of an ion's electrostatic effects, decreases. This increased screening renders the repulsive polyanion–polyanion and counterion–counterion electrostatic interactions weaker, enabling both charged species to accumulate in greater numbers near the boundaries. As a result, there are strong peaks immediately next to, and oscillatory behavior away from, the surface in our simulation density profiles, unlike those predicted by PDFT [14]. Notably, GCMe is able to capture the accumulation of polyanions and counterions on the surfaces driven by the packing effect from the solvent particles, an effect not as pronounced in PDFT due to its treatment of the solvent using a local incompressibility condition.

With the inclusion of attractive image charges, the arrangement of polyanions and counterions near the perfectly conducting boundaries is vastly different. In what
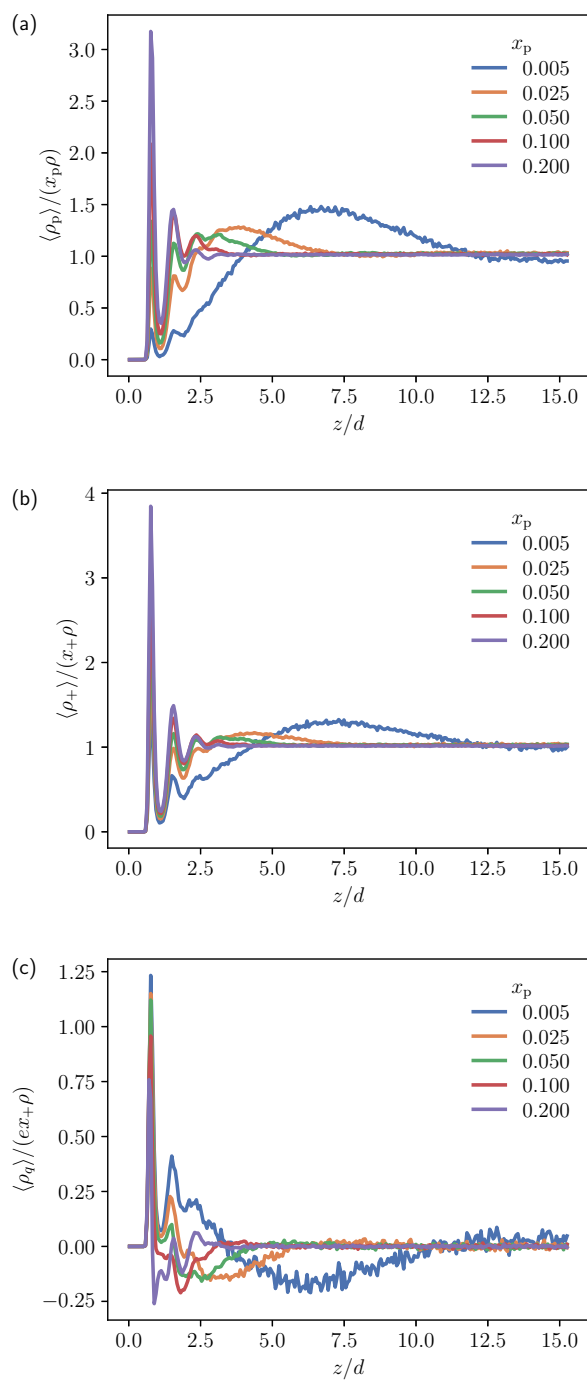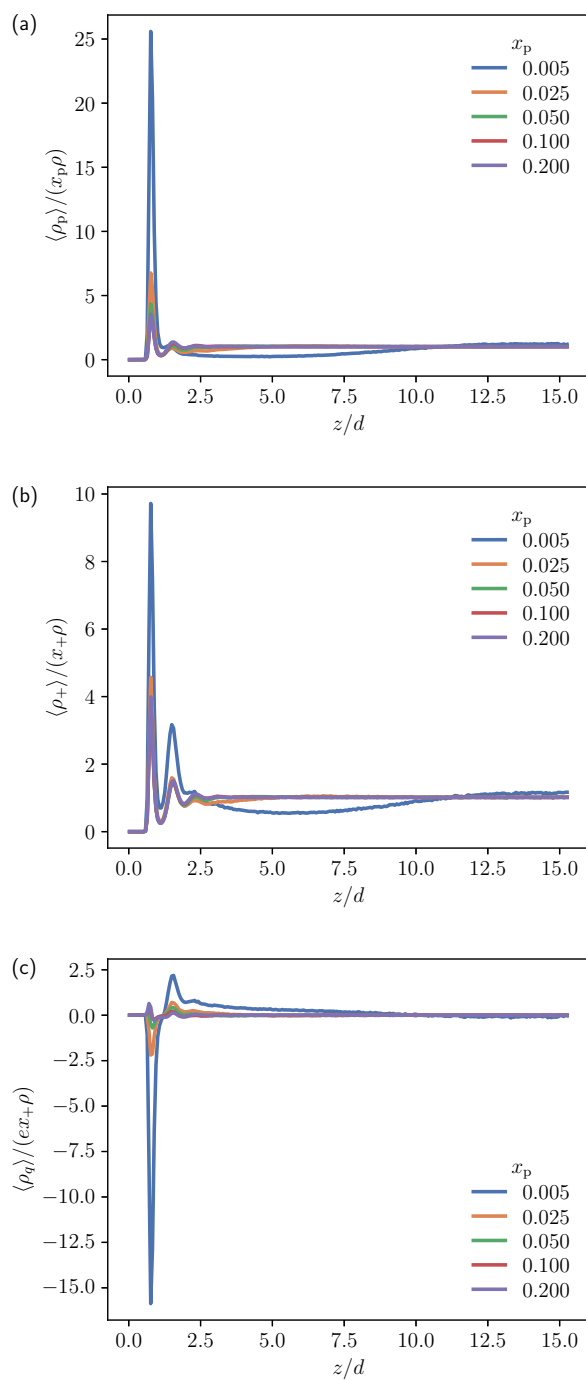
Figure 6.3: Ensemble-averaged (a) polyanion and (b) counterion number density profiles normalized by their respective total number densities, and (c) the charge density profile normalized by the total counterion charge density near a surface for a salt-free polyanion–counterion–solvent system confined by perfectly conducting boundaries. The total number density differs from the bulk number density in the center of system by less than 2%.
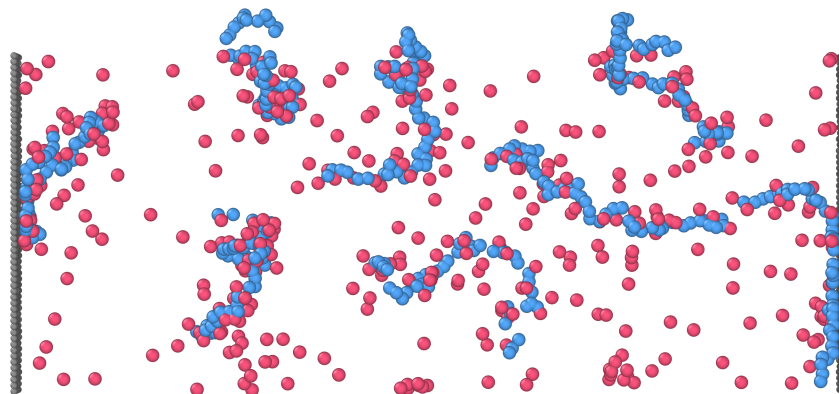
Figure 6.4: Representative simulation snapshot of the real polyanion–counterion–solvent system with perfectly conducting boundaries at $x_p = 0.005$. Solvent particles are not shown.

appears to be a complete reversal from the systems with nonmetal boundaries, there is a strong accumulation of both species on the surfaces and, consequently, a depletion in the outer layers of the EDL. At the low $x_p = 0.005$, the singular intial peak in Fig. 6.3a and the simulation snapshot in Fig. 6.4 clearly show that the polyanions prefer to be adsorbed on the surfaces, suggesting that the attractive image charge interactions can overcome the entropic penalty. Fig. 6.3b shows that there is also an influx of counterions due to the attractive electrostatic polyanion–counterion interactions, but not in equal proportion to the polyanions. As a result, there is now a considerable net negative charge next to the surfaces, as shown in Fig. 6.3c, and a second diffuse layer of counterions is needed to neutralize the first polyanion layer. Additionally, Fig. 6.11 in the Appendix shows that systems with low ion fractions now have positive bulk electrostatic potentials (evaluated using Eq. 6.7 presented subsequently in this chapter), as opposed to the negative ones observed in comparable systems with nonmetal boundaries.

Perhaps surprisingly, when x_p first begins to increase, the number of polyanions and cations adsorbed on the surfaces relative to that in the bulk instead decreases. A simple explanation is that the decreased screening length diminishes the image charge interactions, lessening the driving force for the adsorption of either charged species to the surfaces. This effect is so much more significant than the coinciding weakening of the repulsive electrostatic interactions between like species that the net result is a substantial decrease in the amount of both polyanions and counterions in the EDL. As the polyanion fraction increases further, i.e., $x_p \geq 0.05$, the changes in
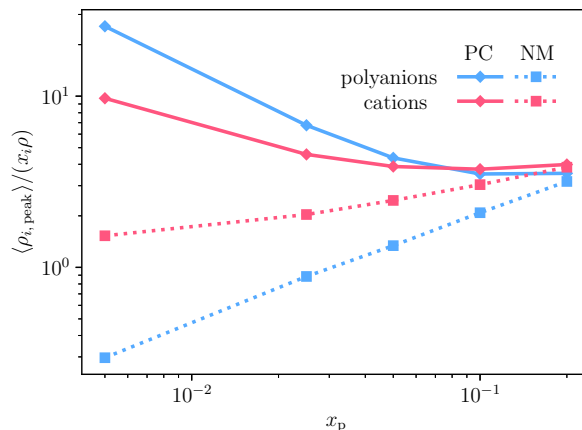
Figure 6.5: Ensemble-averaged polyanion and counterion number densities $\rho_{i,\text{peak}}$ in the first adsorption layer next to the boundaries as functions of the polyanion fraction for perfectly conducting (PC) and nonmetal (NM) boundaries.

the polyanion and counterion distributions near and away from the surfaces become less pronounced, as evidenced by the converging number densities in Fig. 6.3. In particular, the systems with perfectly conducting electrodes end up having a makeup comparable to that of the systems with nonmetal boundaries at high x_p. This is best illustrated in Fig. 6.5, where the polyanion and counterion number densities in the first layer of the EDL for the nonmetal and systems with perfectly conducting boundaries reach similar values at $x_\text{p} = 0.2$.

Therefore, the attractive image charge interactions from perfectly conducting boundaries can have a marked effect on the EDL structure in polyelectrolyte EDLCs, especially at low ion fractions. While the systems with nonmetal boundaries have a moderate net positive layer next to the surfaces due to an uneven depletion of polyanions and counterions, the systems with perfectly conducting boundaries have a sizable net negative adsorption layer due to the enhanced adsorption of polyanions driven by their net electrostatic attraction to the surfaces by the image charges.

Energy storage with charged surfaces

Given the anomalous adsorption behavior, we anticipate different structures and dynamics in the systems with perfectly conducting boundaries since the more pronounced charge separation suggests that they are more susceptible to applied potentials [15, 16]. As such, we are interested in exploring the energy storage and charging/discharging dynamics of polyanion–counterion–solvent EDLCs with applied potential differences ΔV.

To apply potential differences and simulate the charging of the polyelectrolyte EDLCs, we use the constant charge method (CCM) to assign equal but opposite charges to the particles that constitute the opposing surfaces such that each surface had a fixed surface charge density $\sigma_{q,\mathrm{f}}$. The charge magnitude $q_{i,\mathrm{wall}}$ is given by

$$\frac{q_{i,\mathrm{wall}}}{n_{\mathrm{b}}} = \frac{L_x L_y \sigma_{q,\mathrm{f}}}{N_{\mathrm{wall}}}, \tag{6.2}$$

where N_{wall} is the number of particles in each surface and

$$n_{\mathrm{b}} = \begin{cases} 2, & \text{for perfectly conducting boundaries} \\ 1, & \text{for nonmetal boundaries} \end{cases} \tag{6.3}$$

is a scaling factor that must be included for systems with image charge interactions when using a three-dimensional Ewald summation method to evaluate the Coulomb interactions since only half of the calculated energy of the repeat unit should translate to the electrostatic forces on the real ions [15, 17].

Then, to quantify the energy storage, we computed the surface charge density and differential capacitance, measures of the charge accumulated on the surfaces and the amount of energy stored in the EDLCs, respectively. As shown by Hautman et al. [17] and derived by Qing et al. [18], the total surface charge density σ_q is given by

$$\langle \sigma_q \rangle = \sigma_{q,\mathrm{s}} + \langle \sigma_{q,\mathrm{p}} \rangle = \frac{\varepsilon_0 \varepsilon_{\mathrm{r}} \Delta V}{L_z} - \frac{1}{L_z} \int_0^{L_z} z \langle \rho_q(z) \rangle \, dz, \tag{6.4}$$

where ΔV is the potential difference across the electrolyte between the two surfaces. The static term $\sigma_{q,\mathrm{s}}$ captures the direct response of the electrolyte to the applied potential difference, while the polarization term $\sigma_{q,\mathrm{p}}$ accounts for the system dipole generated by the adsorption of the charged species onto the surfaces. The differential capacitance C_{d} is related to the total surface charge density via

$$C_{\mathrm{d}} = \frac{\partial \sigma_q}{\partial \Delta V}, \tag{6.5}$$

with the area under the C_{d}–ΔV curve being proportional to the stored energy.

It is important to note that in the systems with perfectly conducting boundaries, the potential difference is known and related to the fixed or static surface charge density via Gauss's law

$$\sigma_{q,\mathrm{f}} = \sigma_{q,\mathrm{s}} = \frac{\varepsilon_0 \varepsilon_{\mathrm{r}} \Delta V}{L_z} \tag{6.6}$$

since surface equipotentiality is maintained despite the use of CCM due to the inclusion of the image charge effect [19]. On the other hand, only the fixed surface

charge density (which is equal to the total surface charge density, as shown in Fig. 6.6) is known in the systems with nonmetal surfaces, and the potential difference $\Delta V \equiv \Psi(z = L_z) - \Psi(z = 0)$ must be determined by numerically solving the one-dimensional Poisson's equation for electrostatics

$$\frac{\partial^2 \Psi}{\partial z^2} = -\frac{\rho_q(z)}{\varepsilon_0 \varepsilon_r}, \tag{6.7}$$

where $\Psi(z)$ is the position-dependent potential with respect to the reference potential on the left surface, which we arbitrarily set to $\Psi_0 = 0\,\text{V}$.
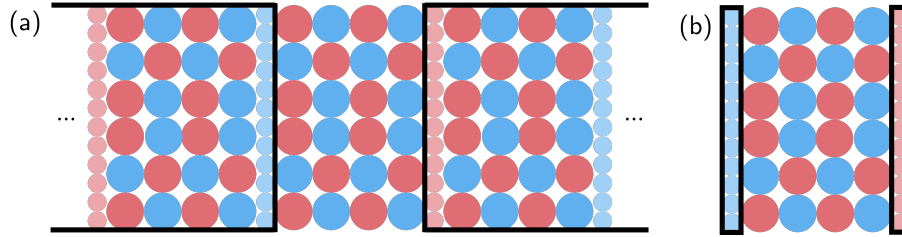

Figure 6.6: Schematic representations of the contributions to the surface charge densities (or potential difference) of (a) perfectly conducting and (b) nonmetal boundaries with the constant charge method. The solid black borders indicate what charges are included in the total surface charge density σ_q. The large circles represent ions (outside black borders) and image charges (inside black borders), the small circles represent surface particles, and the blue and red colors represent negative and positive charges, respectively.
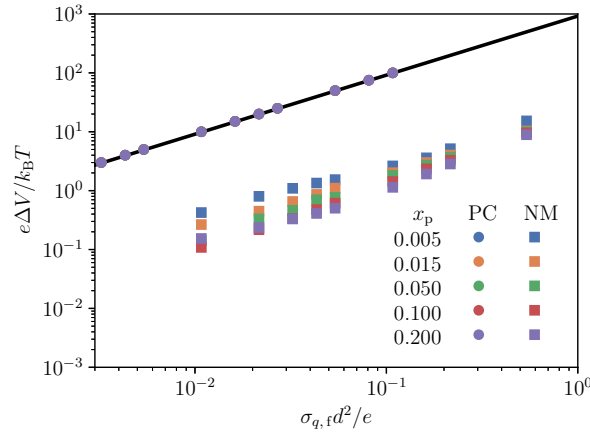
Figure 6.7: Potential difference ΔV between the two perfectly conducting (PC) or nonmetal (NM) surfaces in a polyelectrolyte electric double-layer capacitor as a function of the fixed surface charge density $\sigma_{q,\text{f}}$. The solid black line denotes the potential difference in a perfect conductor according to Gauss's law.

Indeed, Fig. 6.7 demonstrates that the potential differences evaluated using Eqs. 6.6 and 6.7 are equivalent for systems with perfectly conducting boundaries. In these

systems, the potential differences have contributions from both the fixed surface charge density and the image charges. In contrast, for systems with nonmetal boundaries, ΔV is more than an order of magnitude lower at the same $\sigma_{q,\mathrm{f}}$ due to the absence of the attractive image charges. Additionally, ΔV decreases as the electrolyte becomes more concentrated and the screening length increases. This indicates that significantly more energy is required to charge nonmetal surfaces to achieve the same potential difference as in systems with perfectly conducting boundaries.

When compared at the same range of potential differences, Figs. 6.8 and 6.9 show that the surface charge densities and differential capacitance exhibit almost identical behavior in systems with perfectly conducting and nonmetal boundaries. The σ_q–ΔV curves are sigmoidal, with the fastest increase in the surface charge density occurring at low potential differences before slowing down due to crowding effects. Consequently, the C_d–ΔV curves are bell-shaped. Interestingly, for polyanion fractions above $x_\mathrm{p} = 0.025$, the σ_q–ΔV and C_d–ΔV curves nearly overlap, suggesting that the same energy storage can be achieved with dilute polyelectrolyte solutions without requiring very high polyelectrolyte concentrations. This has significant implications for experimental studies and real-world energy storage devices involving polyelectrolytes from a cost savings perspective.

Perhaps more notably, Fig. 6.9 reveals that systems with nonmetal boundaries have a higher capacitance peak at $\Delta V = 0$ V than those with perfectly conducting electrodes, indicating that the former can store slightly more energy at low potential differences. This is contrary to expectations, as the attractive image charge interaction is expected to enhance energy storage. However, the underlying mechanism for this becomes clear when considering the adsorption behaviors on the neutral surfaces shown in Figs. 6.1 and 6.3. In systems with perfectly conducting boundaries, the polyanions and counterions are already near the surfaces, whereas in the systems with nonmetal boundaries, the charged species are both depleted from the surfaces. When a potential difference is first applied, the EDL structure changes little in systems with perfectly conducting boundaries but changes drastically in systems with nonmetal boundaries, resulting in a sharper increase in surface charge density in the latter systems. This suggests that the image charge interaction, when it does not induce a phase separation (like spontaneous surface charge separation), is a near-surface effect whose impact can only be discerned when external forces, such as potential differences, are not dominant.
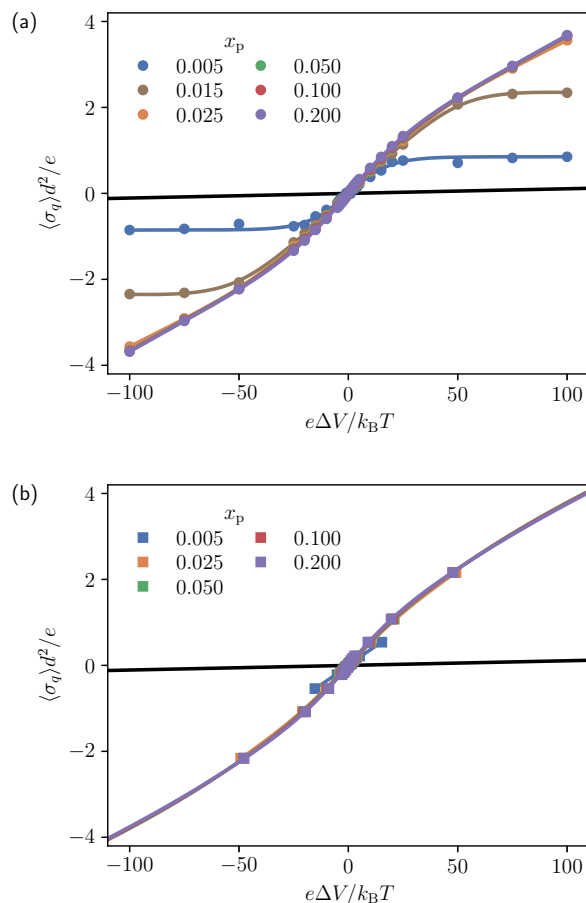
Figure 6.8: Surface charge density σ_q as a function of the potential difference ΔV and the polyanion fraction x_p for polyelectrolyte electric double-layer capacitors with (a) perfectly conducting or (b) nonmetal boundaries. The colored curves are interpolations of the raw data. The abnormal asymptotic behavior in low polyanion fraction systems at large ΔV is an artifact of using NVT ensembles, as all ions are adsorbed on the surfaces and none are left in the bulk.

Charging and discharging dynamics with charged surfaces

We investigate the charging and discharging dynamics of polyanion–counterion–solvent systems by analyzing how the surface charge density σ_q responds to the application or removal of potential differences. Our focus is on systems with perfectly conducting boundaries due to their expected non-monotonic non-monotonic charging behavior and the necessity to maintain equipotentiality during the charging and discharging processes. To mitigate finite size effects and efficiently obtain non-equilibrium simulation trajectories that avoid metastable states while waiting for ion reorientation on the surfaces, we used smaller systems with $N_p = 48,000$ particles and dimensions of $26d \times 25.98d \times 28.42d$ to enlarge the surface area with-
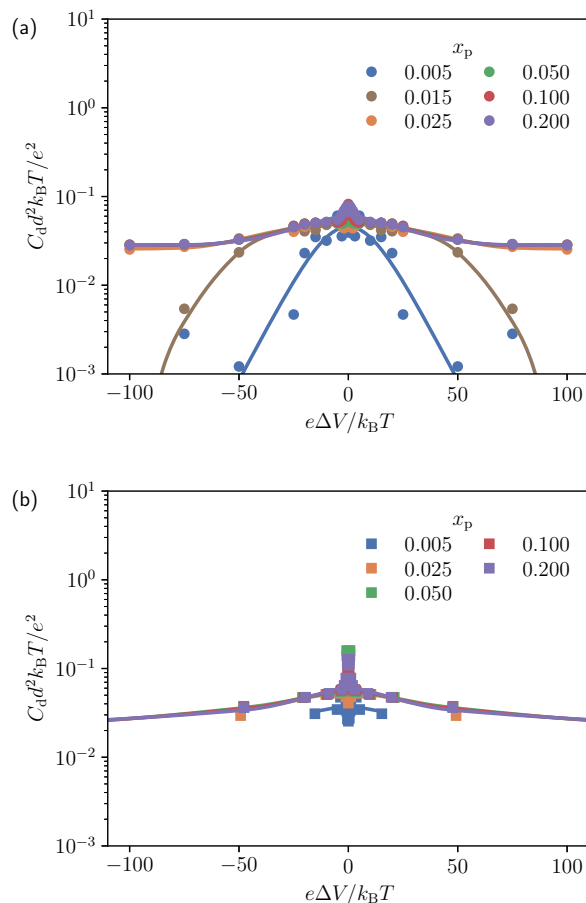
Figure 6.9: Differential capacitance C_{d} as a function of the potential difference ΔV and the polyanion fraction x_{p} for polyelectrolyte electric double-layer capacitors with (a) perfectly conducting or (b) nonmetal boundaries. The colored curves are interpolations of the raw data. The abnormal asymptotic behavior in low polyanion fraction systems at large ΔV is an artifact of using NVT ensembles, as all ions are adsorbed on the surfaces and none are left in the bulk.

out introducing confinement effects. Additionally, we used shorter polymers with a chain length of $N = 30$, which our preliminary testing indicated have the same adsorption behavior as those with $N = 60$.

Charging times τ_{c} and discharging times τ_{d} were extracted from the time traces of $\sigma_q(t)$ after a potential difference is applied or removed, respectively, by fitting stretched exponential functions with the forms

$$1 - \frac{\sigma_q(t)}{\langle \sigma_q \rangle} = \exp[-(t/\tau_{\mathrm{c}})^{\beta_{\mathrm{c}}}] \tag{6.8}$$

and

$$\frac{\sigma_q(t)}{\langle \sigma_q \rangle} = \exp[-(t/\tau_{\mathrm{d}})^{\beta_{\mathrm{d}}}], \tag{6.9}$$

where τ_{c}, τ_{d}, β_{c} and β_{d} are fitting parameters, and $\langle \sigma_q \rangle$ is retrieved from Fig. 6.8a. These functions have been used successfully to analyze the relaxation of dynamically heterogeneous systems that have charging and discharging dynamics unable to be described by a single exponential relaxation process [20].
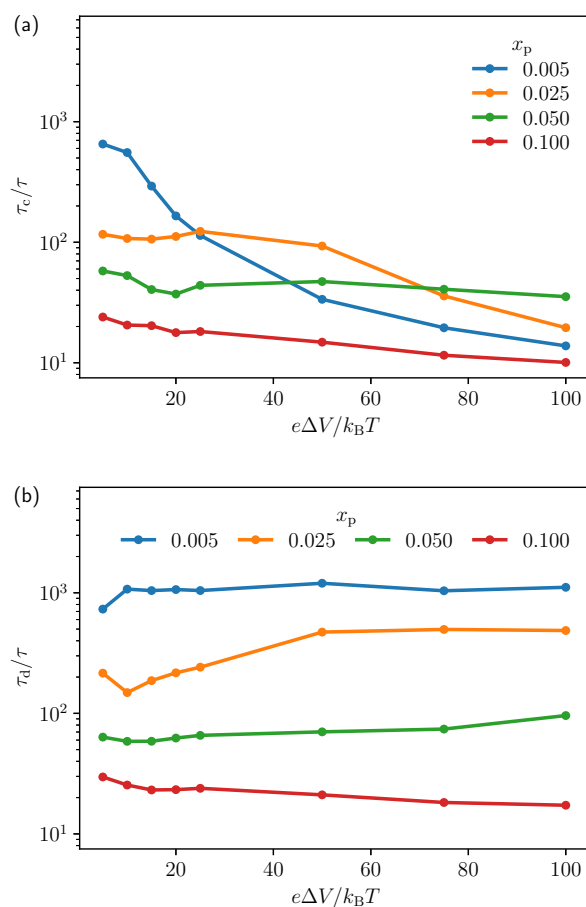
Figure 6.10: (a) Charging times τ_{c} and (b) discharging times τ_{d} in polyelectrolyte electric double-layer capacitors as functions of the polyanion fraction x_{p} and the potential difference ΔV.

Fig. 6.10a displays the charging times obtained from the stretched exponential fits in Fig. 6.12 of the Appendix. At a low $x_{\mathrm{p}} = 0.005$, τ_{c} decreases monotonically as ΔV increases. At low ΔV, the slow charging dynamics are governed by the diffusion of the charged species to and from the surfaces. As ΔV increases, the charging time decreases due to the strengthened electric field, which more effectively separates the

polyanions from their counterions and directs the charged species to their respective surfaces.

For intermediate ion fractions such as $x_p = 0.025$ and $x_p = 0.050$, the τ_c–ΔV relationship generally trends downwards but becomes non-monotonic at moderate ΔV. Compared to systems with low ion fractions, the charging dynamics at low ΔV are faster due to a higher availability of charged species near the surfaces, making the EDL formation less dependent on the sluggish ion diffusion. At high ΔV, the charging process slows down because the increased ion concentration leads to a stronger screening effect, which diminishes the ability of the electric field to overcome the counterion condensation in the bulk (expected in our system since the dimensionless Coulomb coupling strength is $\Gamma = \lambda_B/b \approx 1.5$, which is greater than 1) and effectively draw the charged species to their respective surfaces.

At intermediate ΔV, there is a peak in the charging time caused by a combination of stepwise adsorption and crowding effects. When the potential difference is applied, polyanions adsorb one-by-one or in small groups, which successively screens the electric field and lessens the driving force for subsequent polyanions to adsorb. This behavior is seen in the $\Delta V = 25k_BT/e$ subplot in Fig. 6.12b, where the $1-\sigma_q(t)/\langle\sigma_q\rangle$ curves for individual simulations exhibit stepwise decays during $t < 7,500\tau$. As the adlayer fills with polyanions, the last few polyanions to diffuse to the surface struggle to fit into the remaining gaps, necessitating an in-plane reorientation of the other polyanions to create space. This local maximum in the charging time shifts to higher ΔV as x_p increases since a stronger electric field is necessary to overcome the counterion condensation and complete the adlayer with only polyanions due to stronger screening.

When the ion fraction gets sufficiently large (i.e., $x_p \geq 0.100$), both charged species are abundantly available near the surfaces. Consequently, the charging process is much faster since it is primarily dependent on the adlayer reorientation and less influenced by the ion diffusion or the initial breaking of polyanion–counterion pairs by the electric field.

We now turn our attention to the discharging times shown in Fig. 6.10b, which are obtained from the stretched exponential fits in Fig. 6.13 of the Appendix. Surprisingly, Fig. 6.13a reveals a hysteresis effect during the discharging process for the $x_p = 0.005$ systems, where σ_q does not return to zero due to the strong polyanion adsorption shown previously in Fig. 6.3a. To address this, the average value of $\sigma_q(t)$ past $t > 7,500\tau$ is subtracted from all data points to shift the entire curve down for

fitting Eq. 6.9.

From Fig. 6.10b, there are no immediately obvious τ_d–ΔV trends for any given x_p. However, we do observe that the discharging dynamics accelerate as the ion fraction increases. This occurs because the image charge interactions, which attract the charged species to the electrodes as shown previously in Figs. 6.3 and 6.5, are felt more strongly in the systems with low ion fractions due to weaker screening. As such, when the potential difference is removed, the polyanions tend to remain near the electrodes in their established layers. In fact, for $x_\mathrm{p} = 0.005$ and $x_\mathrm{p} = 0.025$, the discharging process first entails the counterions desorbing from their surface and diffusing across the simulation systems to condense on the polyanions still adsorbed on the opposing surface. Then, the polyanion–counterion pairs leave the surface together, allowing both charged species to return to the bulk. This lingering of polyanions slows down the discharging process, which normally involves the direct exchange of ions between the EDL and the bulk, or the expulsion of both charged species from the EDL into the bulk.

Finally, a comparison of the charging and discharging dynamics in Figs. 6.10a and b shows that the discharging times are consistently longer and can be over an order of magnitude slower than the charging times, which is a complete reversal of the behavior expected and previously reported in systems with nonmetal (dielectric) boundaries [20]. Therefore, the attractive image charge interactions from perfectly conducting boundaries can have a significant impact on the charging and discharging dynamics of polyelectrolyte EDLCs. They not only drastically slow down the discharging process of systems with low ion fractions by keeping polyanions adsorbed on their surface, but also causes the hysteresis effect observed in systems with low ion fractions, such as $x_\mathrm{p} = 0.005$. However, a more systematic study is required to fully characterize that phenomenon, which is beyond the scope of the current study.

6.4 Conclusion

In this chapter, we examined systems consisting of polyanions, their counterions, and solvent particles confined between planar parallel nonmetal or perfectly conducting metal surfaces, where the boundary polarizability was accounted for by the method of image charges. For systems with uncharged nonmetal boundaries, we were able to qualitatively reproduce the depletion of polyanions and counterions from the surfaces that PDFT [14] predicted. Notably, the GCMe simulations showed that there is a growing accumulation of both charged species on the surfaces as the

ion fraction x_p increases, a feature missing in PDFT due to the density smearing under its incompressibility condition. For systems with neutral perfectly conducting boundaries, which cannot be represented by a mean-field treatment, we found a complete reversal in the structure and charge of the effective EDLs. Peculiarly, there is a strong accumulation of both polyanions and counterions on the surfaces, suggesting that the attractive image charge interactions are favorable enough to overcome the conformational entropy penalty from the polyanion adsorption. As x_p increases and the nominal screening length decreases, the image charge interactions weaken and the EDL structure begin to resemble that from a high x_p system with nonmetal boundaries.

Despite the contrasting adsorption behavior, we observed similar energy storage in systems with perfectly conducting and nonmetal surfaces when potential differences were applied, except at low ΔV. At these lower potentials, systems with nonmetal surfaces stored slightly more energy due to a higher capacitance peak, which results from a more significant change in the EDL structure compared to systems with perfectly conducting boundaries, where the EDL is already partially formed due to the strong polyanion and counterion adsorption. However, the charging and discharging dynamics with different boundary materials differed drastically. While previous studies found faster discharging processes than charging processes in systems with nonmetal boundaries, we observed discharging times up to an order of magnitude slower than charging times in systems with perfectly conducting boundaries due to polyanions remaining adsorbed to the surfaces by the attractive image charge interactions even after the potential difference was removed. In systems with low ion fractions, this metastability even causes a hysteresis effect, where the polyelectrolyte EDLCs do not fully discharge and the surface charge density does not return to zero.

These findings underscore the importance of capturing the surface polarizability effects in simulations [21, 22] and how they can influence the energy storage and power delivery capabilities of EDLCs. By understanding these ion–surface interactions, we can better optimize and design electrochemical systems, paving the way for advancements in energy storage devices.

6.5 Appendix

Electrostatic potential profiles for systems with neutral surfaces

The electrostatic potential profile $\Psi(z)$ can determined by numerically evaluating the one-dimensional Poisson's equation in Eq. 6.7 using the charge density profile
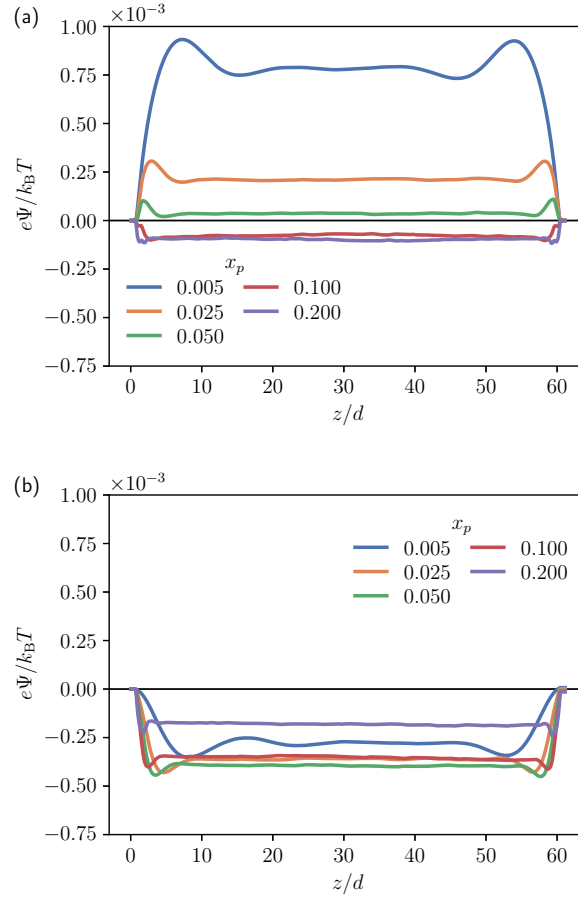
Figure 6.11: Electrostatic potential profiles $\Psi(z)$ for systems with (a) perfectly conducting and (b) nonmetal boundaries at different ion number fractions x_{p}.

$\rho_q(z)$ with boundary conditions $\Psi|_{z=0} = 0$ to use the left surface as the reference and $\partial\Psi/\partial z|_{z=0} = -\sigma_q/(\varepsilon_0\varepsilon_{\mathrm{r}})$ to enforce zero electric field in the bulk of the polyelectrolyte system [9, 23]. Without an applied potential difference ($\Delta V = 0$), the surface charge density σ_q is zero in systems with nonmetal boundaries and $\sigma_q = -L_z^{-1} \int_0^{L_z} z\rho_q(z)\,dz$ in systems with perfectly conducting boundaries due to the polarization effects from the image charges [17, 18].

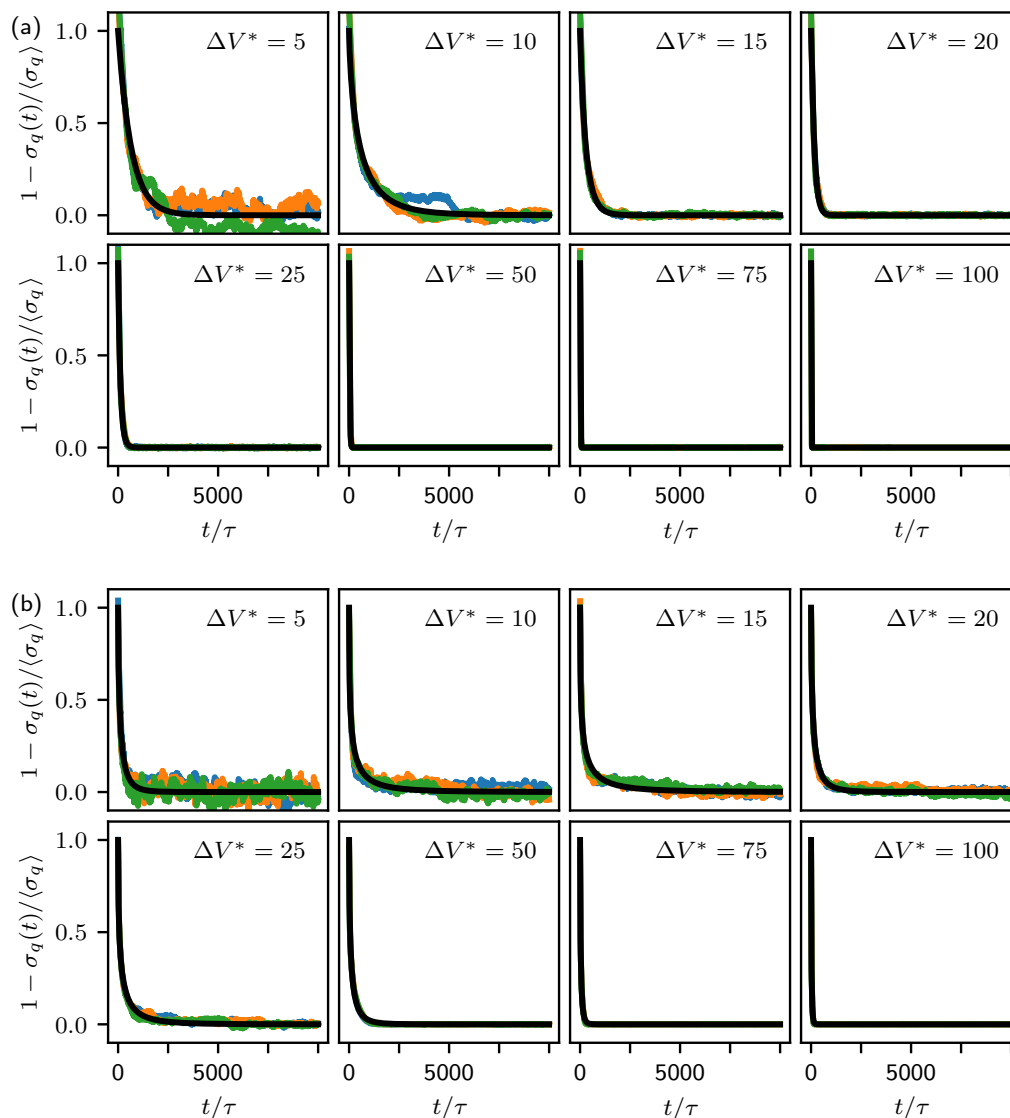**Stretched exponential fits of charging and discharging dynamics**

Figure 6.12: Stretched exponential fits to obtain the charging times τ_c at given reduced potential differences $\Delta V^* \equiv e\Delta V/(k_B T)$ in polyanion–counterion–solvent systems with perfectly conducting electrodes and polyanion fractions of (a) $x_p = 0.005$, (b) $x_p = 0.025$, (c) $x_p = 0.050$, and (d) $x_p = 0.100$. The colored curves show the normalized raw data from three separate simulations.

Figure 6.12: Stretched exponential fits to obtain the charging times τ_c at given reduced potential differences $\Delta V^* \equiv e\Delta V/(k_B T)$ in polyanion–counterion–solvent systems with perfectly conducting electrodes and polyanion fractions of (a) $x_p = 0.005$, (b) $x_p = 0.025$, (c) $x_p = 0.050$, and (d) $x_p = 0.100$. The colored curves show the normalized raw data from three separate simulations.
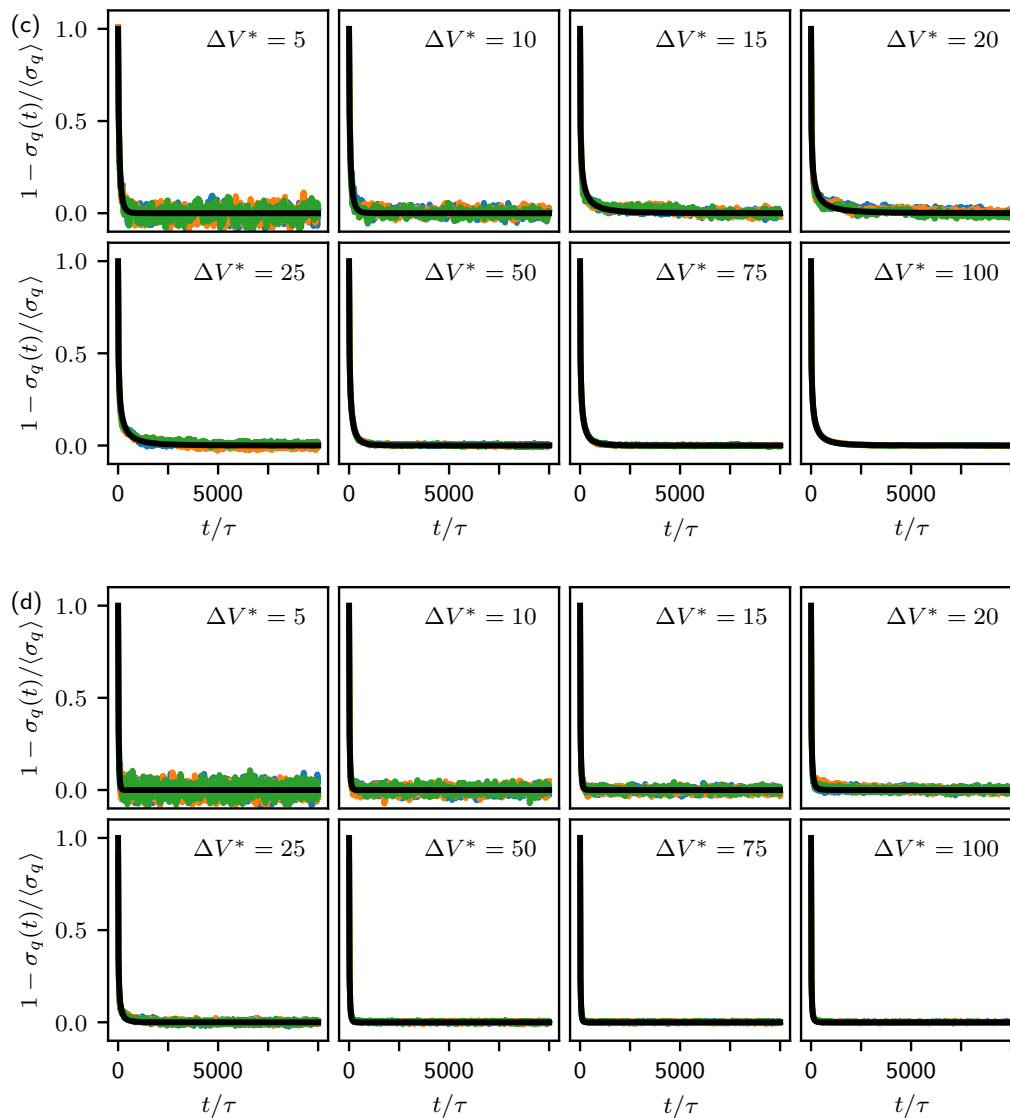
Figure 6.13: Stretched exponential fits to obtain the discharging times τ_d at given reduced potential differences $\Delta V^* \equiv e\Delta V/(k_B T)$ in polyanion–counterion–solvent systems with perfectly conducting electrodes and polyanion fractions of (a) $x_p = 0.005$, (b) $x_p = 0.025$, (c) $x_p = 0.050$, and (d) $x_p = 0.100$. The colored curves show the normalized raw data from three separate simulations.
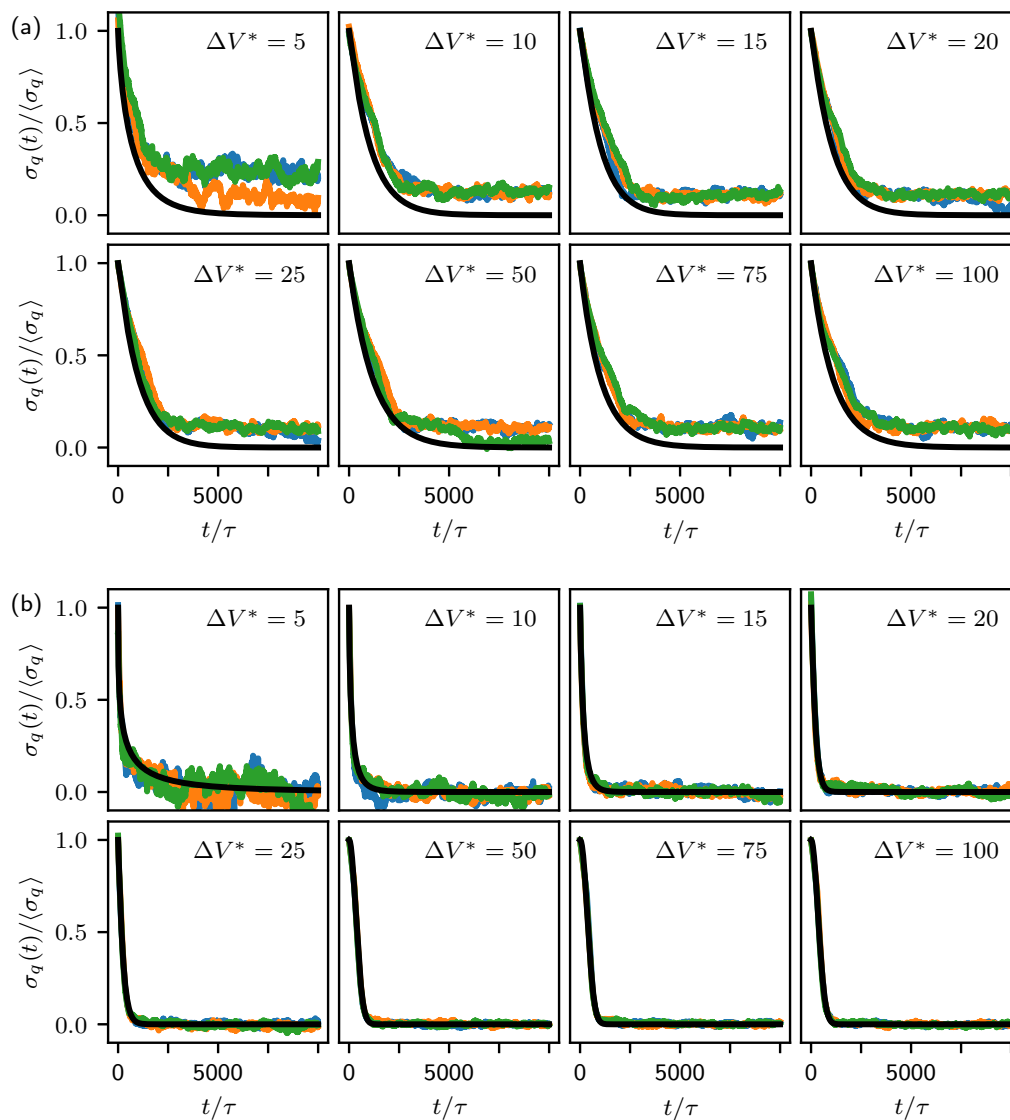
Figure 6.13: Stretched exponential fits to obtain the discharging times τ_d at given reduced potential differences $\Delta V^* \equiv e\Delta V/(k_B T)$ in polyanion–counterion–solvent systems with perfectly conducting electrodes and polyanion fractions of (a) $x_p = 0.005$, (b) $x_p = 0.025$, (c) $x_p = 0.050$, and (d) $x_p = 0.100$. The colored curves show the normalized raw data from three separate simulations.
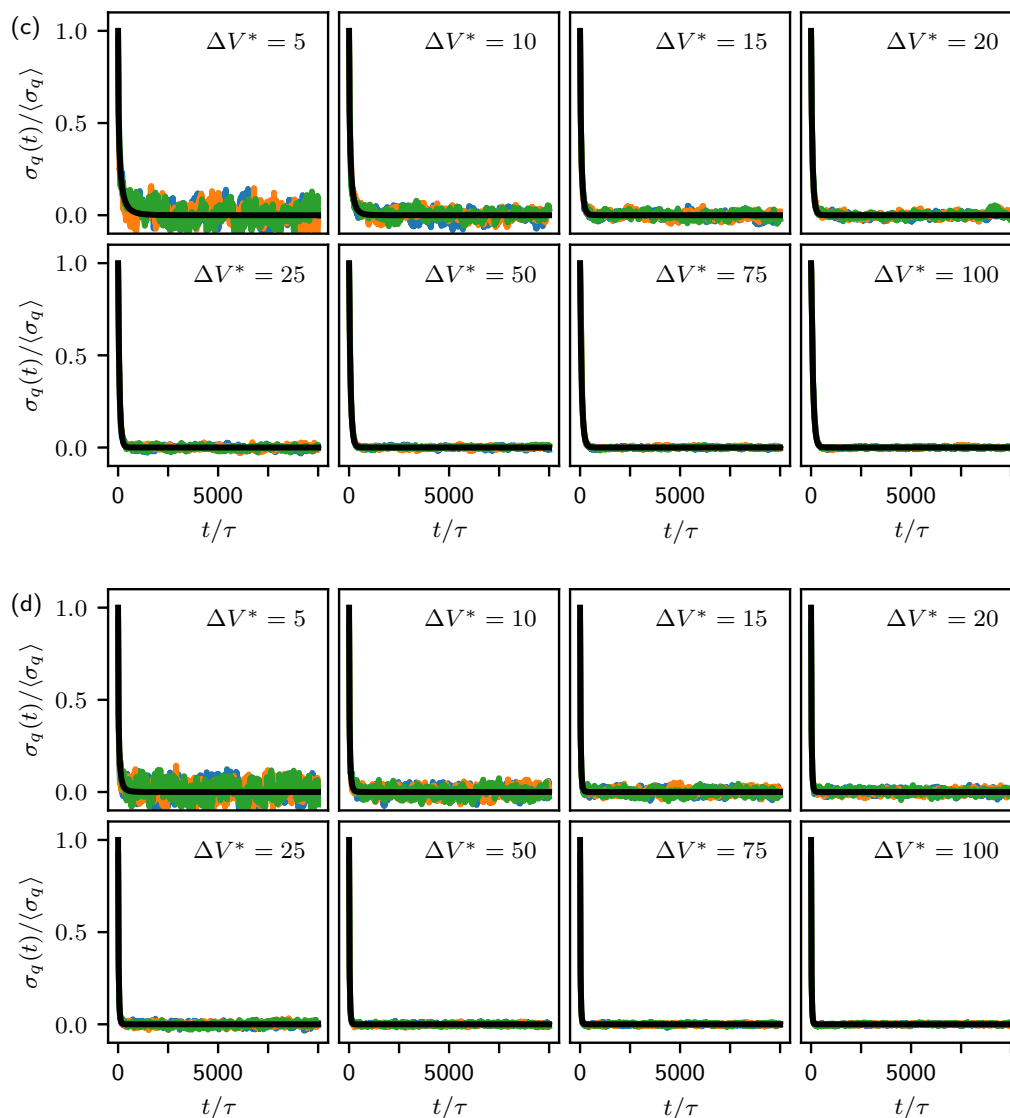
References

(1) Ye, B. B.; Chen, S.; Wang, Z.-G. *J. Chem. Theory Comput.* **2024**, acs.jctc.4c00603, DOI: `10.1021/acs.jctc.4c00603`.

(2) Wang, F.; Wu, X.; Yuan, X., et al. *Chem. Soc. Rev.* **2017**, *46*, 6816–6854, DOI: `10.1039/C7CS00205J`.

(3) Zhong, C.; Deng, Y.; Hu, W., et al. *Chem. Soc. Rev.* **2015**, *44*, 7484–7539, DOI: `10.1039/C5CS00303B`.

(4) Zhang, Z.; Krajniak, J.; Keith, J. R.; Ganesan, V. *ACS Macro Lett.* **2019**, *8*, 1096–1101, DOI: `10.1021/acsmacrolett.9b00478`.

(5) Matsumoto, M.; Shimizu, S.; Sotoike, R., et al. *J. Am. Chem. Soc.* **2017**, *139*, 16072–16075, DOI: `10.1021/jacs.7b09156`.

(6) Lian, C.; Su, H.; Liu, H.; Wu, J. *J. Phys. Chem. C* **2018**, *122*, 14402–14407, DOI: `10.1021/acs.jpcc.8b04464`.

(7) Eyvazi, N.; Biagooi, M.; Nedaaee Oskoee, S. *Sci. Rep.* **2022**, *12*, 1098, DOI: `10.1038/s41598-022-04837-4`.

(8) Wang, R.; Ginzburg, V. V.; Jiang, J.; Wang, Z.-G. *Macromolecules* **2023**, *56*, 7653–7662, DOI: `10.1021/acs.macromol.3c01096`.

(9) Bagchi, D.; Nguyen, T. D.; Olvera de la Cruz, M. *Proc. Natl. Acad. Sci. U.S.A.* **2020**, *117*, 19677–19684, DOI: `10.1073/pnas.2007545117`.

(10) Eastman, P.; Swails, J.; Chodera, J. D., et al. *PLoS Comput. Biol.* **2017**, *13*, ed. by Gentleman, R., e1005659, DOI: `10.1371/journal.pcbi.1005659`.

(11) Yeh, I.-C.; Berkowitz, M. L. *J. Chem. Phys.* **1999**, *111*, 3155–3162, DOI: `10.1063/1.479595`.

(12) Ballenegger, V.; Arnold, A.; Cerdà, J. J. *J. Chem. Phys.* **2009**, *131*, 094107, DOI: `10.1063/1.3216473`.

(13) Jiang, J.; Ginzburg, V. V.; Wang, Z.-G. *Soft Matter* **2018**, *14*, 5878–5887, DOI: `10.1039/C8SM00595H`.

(14) Jiang, J.; Ginzburg, V. V.; Wang, Z.-G. *J. Chem. Phys.* **2019**, *151*, 214901, DOI: `10.1063/1.5123172`.

(15) Son, C. Y.; Wang, Z.-G. *Proc. Natl. Acad. Sci. U.S.A.* **2021**, *118*, e2020615118, DOI: `10.1073/pnas.2020615118`.

(16) Ye, B. B.; Wang, Z.-G. *Phys. Chem. Chem. Phys.* **2022**, *24*, 11573–11584, DOI: `10.1039/D2CP00166G`.

(17) Hautman, J.; Halley, J. W.; Rhee, Y.-J. *J. Chem. Phys.* **1989**, *91*, 467–472, DOI: `10.1063/1.457481`.

(18) Qing, L.; Zhao, S.; Wang, Z.-G. *J. Phys. Chem. B* **2021**, *125*, 625–636, DOI: `10.1021/acs.jpcb.0c09332`.

(19)   Zeng, L.; Tan, X.; Ji, X., et al. *Journal of Energy Chemistry* **2024**, S2095495624001694, DOI: `10.1016/j.jechem.2024.02.043`.

(20)   Noh, C.; Jung, Y. *Phys. Chem. Chem. Phys.* **2019**, *21*, 6790–6800, DOI: `10.1039/C8CP07200K`.

(21)   Nguyen, T. D.; Li, H.; Bagchi, D.; Solis, F. J.; Olvera De La Cruz, M. *Comput. Phys. Commun.* **2019**, *241*, 80–91, DOI: `10.1016/j.cpc.2019.03.006`.

(22)   Dos Santos, A. P.; Jiménez-Ángeles, F.; Ehlen, A.; Olvera De La Cruz, M. *Phys. Rev. Res.* **2023**, *5*, 043174, DOI: `10.1103/PhysRevResearch.5.043174`.

(23)   Boda, D.; Gillespie, D. *Hung. J. Ind. Chem.* **2021**, *41*, DOI: `https://doi.org/10.1515/512`.

Chapter 7

MDCRAFT: A PYTHON ASSISTANT FOR PERFORMING AND ANALYZING MOLECULAR DYNAMICS SIMULATIONS

For new or inexperienced computational chemists and physicists, there are several major deterrents to conducting molecular dynamics (MD) simulations. These include the steep learning curve associated with the complex command-line and application programming interfaces of common MD simulation software, the challenges of initializing stable simulation systems and properly parameterizing intermolecular interactions in the force fields, and the need for a strong understanding of the principles underlying MD simulations and statistical mechanics to correctly process the simulation data and interpret the results. In particular, the data analysis can be an especially daunting task. Not only does data have to be parsed, extracted from large trajectory files, and sanitized before it can be used to compute desired physical quantities, but this procedure also has to be implemented efficiently so that it can be feasibly evaluated on the computer hardware available today. Motivated by the lack of an all-encompassing tool to reduce these hurdles, we developed a easy-to-use and well-documented open-source Python package called MDCraft to provide helper classes and functions that aid in every step of the simulation research workflow. MDCraft has been used extensively in the preceding sections for setting up and simulating intricate soft matter systems, analyzing terabytes of simulation data, and generating publication-ready figures.

This chapter includes content from our manuscript that we submitted for publication in the Journal of Open Source Software. The submission can be accessed at `https://joss.theoj.org/papers/fa65dcce626157b3f2b0b396c43adfed`.

7.1 Summary

MDCraft is a comprehensive Python package designed to enhance research workflows involving molecular dynamics (MD) simulations. It streamlines the entire process—from setting up and executing simulations to analyzing trajectories using sophisticated algorithms and visualizing results—making computational chemistry more accessible to a broader audience. At its core, MDCraft comprises three principal components.

First, the `lammps` and `openmm` modules provide user-friendly tools to initialize, optimize, and run simulations, enabling the exploration of various large soft matter systems across different timescales. These modules extend the functionality of the LAMMPS [1] and OpenMM [2] simulation packages by introducing custom force fields, such as the efficient and intuitive Gaussian core model with smeared electrostatics (GCMe) [3]; incorporating advanced techniques like the slab correction [4, 5] and the method of image charges [6] for charged systems with slab geometries; facilitating coarse-grained MD simulations by scaling physical values by the fundamental quantities (mass m, length d, energy ϵ, and Boltzmann constant $k_\mathrm{B}T$); and offering feature-rich readers and writers for topologies and trajectories stored in memory-efficient formats.

Second, the `algorithm` and `analysis` modules offer optimized serial and multi-threaded algorithms and analysis classes for evaluating structural, thermodynamic, and dynamic properties using thermodynamic state and trajectory data. These properties include, but are not limited to, static and dynamic structure factors, density and potential profiles, end-to-end vector autocorrelation functions for polymers, and Onsager transport coefficients [7].

Finally, the `fit` and `plot` modules simplify the post-processing and visualization of data, aiding in the creation of aesthetically pleasing figures for scientific publications. These modules consist of models for curve fitting and helper functions that interface seamlessly with the commonly used SciPy [8] and Matplotlib [9] libraries.

Together, these modules provide both novice and experienced MD simulation users with a comprehensive set of tools necessary to conduct computer experiments ranging from simple to complex, all within a single, succinct package.

7.2 Statement of need

Although established MD analysis packages such as MDAnalysis [10] and MD-Traj [11] have been around for a considerable time, they primarily focus on the post-simulation analysis. In contrast, MDCraft is designed to provide comprehensive support throughout the entire simulation process, from initialization to post-processing.

MDCraft is tightly integrated with OpenMM, a relatively new simulation toolkit that has seen a surge in popularity in recent years due to its class-leading performance and flexibility through support for custom intermolecular forces and integrators for equations of motion. Due to its age and design philosophy, OpenMM offers com-

paratively fewer choices of pair potentials and external forces, and no on-the-fly analysis support. MDCraft fills this gap in two ways. First, the `openmm` module leverages the modularity of OpenMM to provide a suite of custom force fields, problem-solving tools, trajectory readers and writers, and utility functions for unit reduction, topology transformations, and performance optimizations that are not typically available in other simulation packages. Then, the classes in the `analysis` module enable computing common structural, thermodynamic, and dynamic properties using the topology, trajectory, and state data generated by OpenMM (or other simulation packages).

The `analysis` module also stands out due to the remarkable flexibility it affords its end users. General users have unprecedented control over what aspects of the properties to calculate and which method to employ through a plethora of well-documented built-in options in each analysis class, without having to be concerned about the underlying implementations. More advanced users, on the other hand, have the option to work directly with the algorithms in the `algorithms` module for further customization. These analysis functions and classes have proven indispensable in several recent publications [12–14].

The application of MDCraft extends across various domains within computational chemistry and materials science. Researchers can utilize it to study the low-level mechanisms involved in supercapacitors, polymer gels, drug delivery systems, and nanomaterial synthesis, thus highlighting its versatility and broad applicability in cutting-edge scientific research.

References

(1) Thompson, A. P.; Aktulga, H. M.; Berger, R., et al. *Comput. Phys. Commun.* **2022**, *271*, 108171, DOI: `10.1016/j.cpc.2021.108171`.

(2) Eastman, P.; Swails, J.; Chodera, J. D., et al. *PLoS Comput. Biol.* **2017**, *13*, ed. by Gentleman, R., e1005659, DOI: `10.1371/journal.pcbi.1005659`.

(3) Ye, B. B.; Chen, S.; Wang, Z.-G. *J. Chem. Theory Comput.* **2024**, acs.jctc.4c00603, DOI: `10.1021/acs.jctc.4c00603`.

(4) Yeh, I.-C.; Berkowitz, M. L. *J. Chem. Phys.* **1999**, *111*, 3155–3162, DOI: `10.1063/1.479595`.

(5) Ballenegger, V.; Arnold, A.; Cerdà, J. J. *J. Chem. Phys.* **2009**, *131*, 094107, DOI: `10.1063/1.3216473`.

(6) Hautman, J.; Halley, J. W.; Rhee, Y.-J. *J. Chem. Phys.* **1989**, *91*, 467–472, DOI: `10.1063/1.457481`.

(7) Fong, K. D.; Self, J.; McCloskey, B. D.; Persson, K. A. *Macromolecules* **2020**, *53*, 9503–9512, DOI: `10.1021/acs.macromol.0c02001`.

(8) Virtanen, P.; Gommers, R.; Oliphant, T. E., et al. *Nat. Methods* **2020**, *17*, 261–272, DOI: `10.1038/s41592-019-0686-2`.

(9) Hunter, J. D. *Comput. Sci. Eng.* **2007**, *9*, 90–95, DOI: `10.1109/MCSE.2007.55`.

(10) Michaud-Agrawal, N.; Denning, E. J.; Woolf, T. B.; Beckstein, O. *J Comput Chem* **2011**, *32*, 2319–2327, DOI: `10.1002/jcc.21787`.

(11) McGibbon, R. T.; Beauchamp, K. A.; Harrigan, M. P., et al. *Biophysical Journal* **2015**, *109*, 1528–1532, DOI: `10.1016/j.bpj.2015.08.015`.

(12) Glisman, A.; Mantha, S.; Yu, D., et al. *Macromolecules* **2024**, *57*, 1941–1949, DOI: `10.1021/acs.macromol.3c02437`.

(13) Mantha, S.; Glisman, A.; Yu, D., et al. *Langmuir* **2024**, *40*, 6212–6219, DOI: `10.1021/acs.langmuir.3c03640`.

(14) Lee, S.; Walker, P.; Velling, S., et al. Molecular Control via Dynamic Bonding Enables Material Responsiveness in Additively Manufactured Metallo-Polyelectrolytes, 2024, DOI: `10.21203/rs.3.rs-3643582/v1`.